CHARACTERIZING CARBON-DIOXIDE FLUXES FROM OCEANS AND

TERRESTRIAL ECOSYSTEMS

Thesis by

Nir Y. Krakauer

In Partial Fulfillment of the Requirements

for the Degree of

Doctor of Philosophy

California Institute of Technology

Pasadena, California

2006

(Defended May 19, 2006)

ACKNOWLEDGEMENTS

Chapters 1 and 2 were published with slight textual changes as journal articles (citations given in the Overview below) for which copyright is held by the American Geophysical Union. They are included here with permission.

Contributions to specific chapters are as follows:

Chapter 1: James Randerson was my coauthor in the version of this chapter published as a journal article. I thank Jim Collatz for valuable discussions and Lianhong Gu for providing a preprint of his *Science* paper. Lianhong Gu and an anonymous

Finally, I thank my family and friends for believing in me.

ABSTRACT

Understanding the processes that change the amount of carbon stored in the ocean and in the land biota, with their implications for future climate and ecology, is a fundamental goal of earth-system science. I have developed, refined, and applied several approaches that combine data analysis and modeling to better understand processes affecting carbon fluxes.

(1) Using a database of tree-ring widths from some 40,000 trees, I looked at the impact of large volcanic eruptions in the past millennium on tree growth globally. I found a decline in growth north of 45° N lasting for several years after eruptions, presumably due to eruption-associated cooling, and no significant impact at lower latitudes. This argues against the hypothesis that the increased diffuse-light fraction due to volcanic aerosols greatly increased plant carbon uptake after the 1991 Pinatubo eruption, suggesting that other explanations are needed for the slow increase in atmospheric CO_2 levels in the early 1990s.

(2) I applied generalized cross-validation (GCV) to the problem of estimating a regional CO_2 source/sink pattern consistent with observed geographic variation in atmosphere CO_2 levels. I showed that GCV works for selecting data and regional-flux uncertainty levels to assume for this inverse problem; these have usually been estimated rather arbitrarily, though they can have a large impact on the solution.

(3) The air-sea gas transfer velocity determines how fast the surface ocean adjusts to a change in atmospheric composition, and hence is important for understanding ocean

CO_2 uptake. By modeling the ocean's adjustment to fluctuations in atmospheric carbon isotope composition and analyzing a variety of atmosphere and ocean bomb-^{14}C and ^{13}C measurements, I estimated regional and global mean gas transfer velocities, concluding that there may be less latitudinal variation in the gas transfer velocity than usually thought – implying, for example, relatively low CO_2 uptake in the Southern Ocean.

TABLE OF CONTENTS

---

[1] For technical reasons, this appendix (beginning after p. 47) has its own page and section numbering and bibliography.

LIST OF FIGURES

LIST OF TABLES

Overview

Carbon is the central element in the chemical structure of life on earth, and its movements in the biosphere are closely related to life processes. Broadly, carbon cycles between inorganic (oxidized) forms in the atmosphere, ocean and lithosphere and organic forms in living organisms, detritus in soil and in the ocean column and sediments, and sedimentary rocks, with residence times ranging from months to millions of years for different pools in each of these categories. The rates of the major processes and something about how they changed through geologic time were largely worked out in the 1950s-1990s, aided by the advent of precise measurements of the partial pressure of carbon dioxide; measurements of the isotopic composition of carbon; and long-term monitoring sites at forests and other ecosystems that aimed to construct detailed carbon budgets. Concurrently, human industry has been modifying carbon flows in increasingly drastic ways. Land where a large fraction of all carbon is fixed is now used for supplying food and various other biomass products [*Vitousek et al.*, 1986; *Rojstaczer et al.*, 2001]. Also, primarily due to fossil fuel burning, the atmospheric CO_2 partial pressure is increasing at a geologically rapid rate, with the CO_2 mixing ratio going from 280 ppm in the 19th century to 380 ppm today; the absorption of outgoing infrared radiation resulting from this increase is the leading contributor to an enhancement in greenhouse warming that, if trends continue, will raise mean temperatures by several degrees C in a century. Ongoing monitoring of carbon flows is therefore of considerable practical importance both to living within our natural resource base and to developing ways of limiting climate change.

Estimating year-to-year changes in the carbon content of the ocean and land biosphere requires an interdisciplinary approach and much ingenuity, since the relative change in the carbon content is small and the carbon fluxes are very heterogeneous. The work set out here develops several approaches to using a variety of data, together with appropriate statistical methods and previously developed models, to gain a better understanding of the processes that control carbon flows between the atmosphere and the ocean and land biosphere. In the following, I will briefly describe the motivation, methods, conclusions and impact of the research presented in each chapter.

In chapter 1, I quantify the effects of large volcanic eruptions on plant growth using a large database of tree-ring records. I was drawn to tree rings as recorders of plant response to large volcanic eruptions while seeking to assess the possibility that the cooling and darkening following a large volcanic eruption that resulted in a worldwide sulfur aerosol haze, as in the "year without a summer" following the Tambora eruption in 1815, would devastate agriculture. By looking at changes in tree-ring width after historically known eruptions in a database of thousands of chronologies, I could gauge the impact of large eruptions on plant growth in different places, and I found a small but significant reduction in growth in trees at middle and high northern latitudes. This also provided indirect evidence against the hypothesis that the observed lower growth rate of the atmospheric carbon dioxide concentration in 1991-1993, following the Pinatubo eruption, was because the eruption fostered *increased* plant growth, for example by increasing the diffuse light fraction so that light reached shaded leaves; alternative explanations, such as a reduction in respiration rates due to the cool temperatures,

become more likely. (*Indirect* evidence because the tree-ring database used had few records extending past the Pinatubo eruption, so that our results were primarily based on trends in tree-ring width after earlier eruptions of similar magnitude to that of Pinatubo.)

This work was published in *Global Biogeochemical Cycles* [*Krakauer and Randerson*, 2003]. In a 2003 AGU conference presentation, I used tree-ring and eddy-covariance measurements from Harvard Forest to show that, in fact, no enhancement in growth is seen there after the Pinatubo eruption. Subsequent research showed that the seasonality of the enhanced CO_2 uptake in 1991-1993 was, in fact, inconsistent with an increase in net primary production as the cause [*Angert et al.*, 2004]. The complex effects of aerosol pollution on plant growth, due to light scattering as well as other mechanisms, continue to be investigated using field data and modeling [*Niyogi et al.*, 2004; *Steiner and Chameides*, 2005]. The equally complex impacts of interannual temperature variability on CO_2 uptake and release, which differ by region and display intriguing time lags, have recently been discussed by *Adams and Piovesan* [2005].

In Chapter 2, I describe a method of choosing parameters in inversions for regional carbon fluxes based on information on atmospheric CO_2 concentrations and how they reflect transport from CO_2 source or sink regions. This sort of inversion has been an important recent approach to estimating regional ecosystem carbon uptake and its interannual variability, with the idea of deducing the net CO_2 flux from measurements of air CO_2 concentrations in stations around the region of interest. Inversion-based estimates have varied widely between studies, however, in part because of different assumptions made regarding the structure of the measurement errors and the smoothness of the

regional flux fields. Using as a starting point the well-documented inversion protocol of the TransCom project [*Gurney et al.*, 2002], which had as its goal to use a suite of atmospheric transport models to quantify the error induced in such inversions by assumptions about the transport of CO_2 from source regions to measurement stations, I applied a statistical method known as generalized cross validation (GCV) to select values of these parameters that fit available data and model predictions.

This work was published in *Geophysical Research Letters* [*Krakauer et al.*, 2004], with the Appendix included as a supplement to more fully explain how to implement GCV. With Christian Rödenbeck (Max-Planck-Institut für Biogeochemie, Jena) and others, I have since then begun exploring how to usefully employ GCV in complicated and high-dimensional inversion set-ups. The alternative statistical approach of choosing inversion parameters based on maximum likelihood, alluded to in the Appendix, has been taken up by *Michalak et al.* [2005].

In Chapter 3, I develop several approaches to learn about regional mean air-sea gas transfer velocities from knowledge of carbon isotope abundances in CO_2 in the atmosphere and ocean. Uptake by the ocean, which contains very large amounts of dissolved (and mostly ionized) CO_2 in approximate long-term equilibrium with the atmospheric concentration, is believed to be the main factor in slowing down the current buildup of CO_2 in the atmosphere. An important constraint on the air-sea gas transfer velocity has been ocean uptake of ^{14}C from nuclear-bomb explosions mostly in the late 1950s and early 1960s. The distribution of bomb ^{14}C in the ocean could be used to infer the regional distribution of the mean air-sea gas exchange rate, an inverse problem

analogous to the inversion of atmospheric CO_2 measurements discussed in Chapter 2; this time, an ocean transport model is required to relate the observed ocean bomb ^{14}C enhancement pattern to fluxes across the ocean surface. Using state-of-the-art transport fields derived by the Estimating the Circulation and Climate of the Ocean (ECCO) consortium through assimilating millions of hydrographic measurements, I modeled ocean bomb ^{14}C uptake for a variety of candidate fields of air-sea gas transfer velocity. With these results, I estimated the air-sea gas exchange rate for different ocean regions that best fit thousands of ocean ^{14}C measurements, and parameterized this rate as a function of satellite-measured mean windspeed fields. I also compared the resulting atmospheric ^{14}C distribution and ocean ^{13}C and total CO_2 uptake with observations of the rate of change and latitudinal gradients in atmospheric ^{13}C and ^{14}C isotopic ratios (relative to the predominant isotope, ^{12}C). These independent lines of evidence support a relatively weak increase of gas transfer velocity with regional-mean windspeed and an only moderately high gas transfer velocity in the windy Southern Ocean, suggesting less CO_2 uptake in the Southern Ocean than estimated from observations of sea surface pCO_2 assuming that the gas exchange rate increases rapidly with windspeed. These findings are in review for the *Tellus* International Carbon Dioxide Conference special issue. My modeling of the atmospheric ^{14}C distribution resulting from fossil fuel emissions, land respiration, and ocean uptake will hopefully help guide and interpret ongoing measurements at UC Irvine and elsewhere of the latitudinal distribution and the seasonal cycle in the atmospheric ^{14}C. The Appendix to this chapter details how to infer isotope fluxes from the observed rate of change in the abundance of an isotope such as ^{13}C in a reservoir such as the atmosphere.

Chapter 1: Tree-Ring Evidence for the Effect of Volcanic

Eruptions on Plant Growth

1.1 Abstract

Low growth rates of atmospheric CO_2 were observed following the 1991 Pinatubo (Luzon) volcanic eruption. One hypothesis for this CO_2 anomaly is that since diffuse light is more efficiently used by forests than direct light, the increase in the diffuse fraction of sunlight due to scattering by volcanic sulfur aerosol in the years following the eruption substantially increased forest net primary production (NPP). However, satellite observations suggest a decrease in NPP of northern forests because of the cooler conditions following the eruption. Here, we used a global database of dated tree ring widths (which correlate with forest NPP) to test this hypothesis. Ice core records of sulfur deposition allowed us to identify the timing and magnitude of 23 Pinatubo-scale eruptions since 1000 CE. We found a significant decrease in ring width for trees in mid- to high northern latitudes (north of 45° N) following eruption sulfur peaks. Decreases in tree ring widths were in the range of 2-8 % and persisted for ~8 years following sulfur peaks, with minima at around 4-6 years. Ring-width changes in the southern hemisphere (30° S to 56° S) and at lower latitudes in the northern hemisphere (30° N to 45° N) were not significant. In the tropics (30° N to 30° S) the paucity of tree ring records did not permit the evaluation of NPP changes. Given that elevated aerosol levels and summer cooling last only ~2-3 years after an eruption, the persistence of declines in northern tree growth for up to 8 years after eruptions implies some additional mechanism that links these shorter-lived global eruption effects to sustained changes in tree physiology, biogeochemistry, or microclimate. At least for this sample of trees, the beneficial effect of aerosol light scattering appears to be entirely offset by the deleterious effect of eruption-induced climate change.

1.2 Introduction

The June 1991 Pinatubo eruption was the century's largest in terms of stratospheric sulfur emissions and effects on global climate [*Hansen et al.*, 1996; *Jones and Cox*, 2001]. It was followed by ~3 years of reduced atmospheric CO_2 accumulation [*Prentice et al.*, 2001]. Concurrent measurements of atmospheric $\delta^{13}C$ provide evidence that the carbon sink was terrestrial [*Battle et al.*, 2000; *Francey et al.*, 2001] while inverse modeling based on remote CO_2 flask measurements implicates the northern mid- and high latitudes [*Fan et al.*, 1998; *Rayner et al.*, 1999; *Bousquet et al.*, 2000].

Following the Pinatubo eruption, scattering by sulfur aerosols globally increased the diffuse fraction of incident light with only modest reductions in total light levels [*Molineaux and Ineichen*, 1996]. An increase in diffuse light fraction at constant total light levels is thought to enhance photosynthesis, particularly in forests, by distributing light more evenly among leaves – decreasing the shade volume within the canopy – and thus increasing canopy light use efficiency. Modeling of light use by forest and crop leaves [*Sinclair et al.*, 1992; *Cohan et al.*, 2002] along with eddy-covariance based measurements of carbon uptake under cloudy as compared with clear conditions [*Gu et al.*, 1999; *Gu et al.*, 2002] clearly show that instantaneous, canopy-level light use efficiencies are higher for diffuse as compared to direct radiation.

Roderick et al. [2001] hypothesized that the carbon sink following the Pinatubo eruption resulted from a volcano-induced increase in the diffuse fraction of incident sunlight boosting terrestrial photosynthesis. Building on the canopy-level studies showing diffuse-light growth enhancement, *Roderick et al.* [2001] estimated a 7% increase in global plant net primary production (NPP), and wood production specifically, as a result

of the increase in diffuse light fraction in the year following the Pinatubo eruption; this would roughly match the observed carbon uptake. *Gu et al.* [2003] explicitly tested this hypothesis using tower eddy covariance measurements of CO_2 uptake in the Harvard Forest, finding ~15% increases in noontime photosynthesis rates under clear skies in 1992-1993.

In contrast, satellite measurements of Normalized Difference Vegetation Index (NDVI) suggest that leaf area and NPP in northern hemisphere extratropical forests actually decreased following the Pinatubo eruption as a result of cooler summer temperatures [*Zhou et al.*, 2001] and a reduction in the length of the growing season [*Lucht et al.*, 2002], although interference of volcanic aerosols with the satellite observations of vegetation reflectance complicates interpretation [*Myneni et al.*, 1998; *Shabanov et al.*, 2002]. Modeling studies suggest that an enhanced carbon sink in northern biomes after Pinatubo can be consistent with reduced NPP assuming that heterotrophic respiration decreased by an even greater extent than NPP in response to summer cooling [*Jones and Cox*, 2001; *Lucht et al.*, 2002].

Previous studies have used the correlation with climate of tree ring parameters such as width and maximum latewood density to reconstruct climate responses to past volcanic eruptions [*Lough and Fritts*, 1987; *Briffa et al.*, 1998; *D'Arrigo and Jacoby*, 1999]. The existing body of tree ring width chronologies can also be more directly used to test the hypothesis that the increase in diffuse light associated with volcanic events enhances NPP. Tree radial increment is proportional to annual NPP in a variety of forest types [*Grier and Logan*, 1977; *Graumlich et al.*, 1989; *Gower et al.*, 1992; *LeBlanc*, 1996; *Rathgeber et al.*, 2000]. This link with NPP makes the spatially extensive tree ring

chronologies from the last millennium a potentially useful means for evaluating the

response of NPP to a variety of environmental factors, including volcanic events, at both

regional and global scales. Since many tree-ring chronologies extend over a period of

several centuries, we can obtain additional confidence in any patterns found by assessing

their consistency across multiple volcanic eruptions.

1.3 Methods

We compiled all dated tree ring width data files from the International Tree Ring

Data Bank (ITRDB) that included site longitude and latitude. This yielded 1,498 sites,

with a median of 25 cores per site, and a total of 43,447 cores in our analysis (Figure

1.1a). (In the studies contributing to the ITRDB, typically 2 cores were sampled from

each tree [*Schweingruber*, 1988].) The ITRDB [*Contributors*, 2003] represents data

gathered by over 100 different research groups. The largest single block, 31% of the sites

we used, came from the northern hemisphere temperate and boreal tree ring network

developed by *Schweingruber et al.* [1991] for reconstructing regional summer

temperatures [*Briffa et al.*, 1998; *Briffa et al.*, 2001; *Briffa et al.*, 2002]; no other single

research group contributed more than 5% of the sites used. Conifers (gymnosperms)

accounted for 86% of the sites in our analysis, with *Pinus* (pine), *Picea* (spruce), and

Larix (larch) respectively representing 30%, 21%, and 7% of the total. Broadleaf trees

(angiosperms) accounted for the remaining 14% of the sites, with *Quercus* (oak) the most

prevalent genus (7% of total sites).

Width series were first divided by a 41 year moving average to remove tree-age as

well as low-frequency climatic effects. All cores from a given site were averaged to

produce a nondimensional width-index time series with a mean of 1 [*Fritts*, 1976]. Then all available site indices were averaged to produce ring-width indices for site subgroups of interest that extended back as far as 1000 CE, which were again normalized to a unit mean.

Even for the last few centuries, climatically important volcanic eruptions are incompletely known, and the different published compilations differ somewhat; a volcanic aerosol "dust veil" often cannot be assigned to a historically known eruption [*Bradley and Jones*, 1995]. However, sulfate levels in ice cores, which show pronounced peaks as aerosol from a large eruption is deposited, can provide the basis for consistent estimates of past volcanic aerosol levels [*Zielinski*, 2000]. Points within an ice core can be dated to the year by counting annual layers downward from the surface, either visually or using the annual cycle in such ice properties as $\delta^{18}O$. (For a comprehensive discussion of stratigraphic dating of ice cores, see *Alley et al.* [1997].)

We used the time series of annual mean northern hemisphere 550-nm optical depth since 1000 CE from *Crowley* [2000] (http://www.ngdc.noaa.gov/paleo/pubs/crowley.html) to identify eruption years. This time series was derived primarily from high-resolution ice core sulfate measurements calibrated against atmospheric observations after modern eruptions. Eruption years were defined as those that showed a peak in volcanic aerosol forcing; this was often the year after the actual eruption implicated, e.g., 1992 for Pinatubo (Table 1.1). Many of these eruption years, and all of the eruption years before 1500, do not correspond to known large eruptions (Table 1.1), presumably because of the incompleteness of the historical record of volcanism. Using an optical depth estimate of 0.1 as a threshold (Pinatubo peak

depth in this series was 0.123) we obtained 23 eruption years during the period 1000-1970, or 2.4 per century (Table 1.1). Note that width changes after Pinatubo itself (and the 1982 El Chichón eruption) were not included in our averaging of ring width index departures across eruption years because ring widths were not available for a long enough period after these eruptions to allow the same filtering scheme to be used.

The possibility of missing or double-counting annual layers introduces the potential for error in ice core chronologies, so that the uncertainty in dating increases going back in time from the known surface date. The *Crowley* [2000] time series of northern hemisphere sulfate aerosol levels since 1000 is based primarily on measurements from two extensively studied Greenland ice cores, Crête and GISP2 [*Hammer et al.*, 1980; *Zielinski*, 1995]. An idea of the accuracy of the dating of these cores over this period can be obtained from considering the very large mid-13th century sulfur peak from an unidentified tropical eruption, which is accompanied by distinctive volcanic tephra in ice cores from both hemispheres [*Palais et al.*, 1992]. The highest sulfate concentrations from this event are in the 1259 layer for both cores, as well as for at least two other arctic cores independently dated by counting layers [*Langway et al.*, 1988; *Zielinski*, 1995]. This suggests that drift between the two cores and between each core and calendar years is ≤1 year at least as far back as the 13th century.

For southern hemisphere sites, we used southern hemisphere volcanic-aerosol optical depths from the time series of *Robertson et al.* [2001] (http://www.ngdc.noaa.gov/paleo/pubs/robertson2001/robertson2001.html). This time series extends back to 1500 and was also derived primarily from ice core records. For this time series, we used a threshold optical depth of 0.085 because this time series' value for

northern hemisphere post-Krakatau forcing is 15% lower than that from *Crowley* [2000]. This threshold yielded 12 southern hemisphere eruption years (Table 1.1).

Standard errors for width departures following eruptions were calculated from the distribution of width departures across eruption years. Since the distribution of ring widths tends to be skew rather than normal [*Schweingruber*, 1988], departures were tested for significance using a Monte Carlo approach. For the same group of sites, ring width departures were separately calculated (using the same filtering and averaging approach described above) for 1000 different scenarios in which random groups of years were substituted for the actual eruption years. This approach provides an estimate of the probability that a given width anomaly following eruptions would arise by chance. We used $p = 0.05$ (two-tailed) as the significance level.

We combined all sites within 15° wide latitude zones to produce zonal ring width time series before and after eruption events. Since sites were concentrated in the northern extratropics (Figure 1.1a), we excluded the tropics (30°N-30°S). Ring width departures in percent are reported in Table 1.2 for two combinations of years: years 0 to 1 relative to the eruption year, when atmospheric aerosol levels and thus enhancement of diffuse radiation should have been greatest [*Roderick et al.*, 2001], and years 0 to 8, to examine longer-term effects on tree growth.

1.4 Results

For years 0-1, trees north of 60° N showed a trend toward narrower widths that was significant when sites were weighted according to regional levels of NPP but not when all sites within the latitude zone were weighted equally (Table 1.2; Figure 1.3a). No

other zone examined showed significant year 0-1 width departures (Table 1.2; Figure 1.1b).

Significantly narrowed tree rings (implying decreased levels of NPP) were found in regions north of 45° N for the period 0-8 years after eruption years (Figure 1.2; Table 1.2). Trees north of 60° N showed a multiyear decline in mean ring width following eruptions, with the maximum reduction in ring width (8.1±2.7%) occurring in year 4 and an average decrease in years 0-8 of 5.0±1.4% (Figure 1.3a). Sites 45°-60° N showed a similar pattern but with smaller amplitude: the maximum reduction in ring width (4.3±1.2%) occurred in year 6 and the average decrease in years 0-8 was 1.9±0.8% (Figure 1.3b). In the two remaining zones – 30°-45° N and south of 30° S – the ring width departures for years 0-8 were not significant (Table 1.2), nor do the individual years show any clear anomalies (Figure 1.3c,d).

Among trees north of 45° N, we found significant multiyear width reductions for a number of individual conifer genera (Figure 1.4a-c, Table 1.2). However, *Quercus*, the primary broadleaf genus in this zone in our data set, did not show any significant ring width departures (Figure 1.4d). Width reductions were widely distributed longitudinally, though they appear to be greater over Eurasia than over North America (Figure 1.1b,c).

We found negative ring width departures for trees north of 45° N after most of our individual northern hemisphere eruption years (20 out of 23; Figure 1.5a). Over a range of peak optical depths (from *Crowley* [2000]), there was a positive correlation between the degree of width reduction north of 45° N and the peak optical depth (Figure 1.5b). Although we did not include the recent Chichón and Pinatubo eruptions in our analysis of response patterns across eruption years, ring widths around these eruptions appear to be

broadly consistent with the response patterns observed after earlier eruptions (Figure 1.5a).

In the earlier part of our study period there are fewer site chronologies available (75% of sites in our data set have widths for 1800, 17% for 1500, 5% for 1200, 3% for 1000) and eruption magnitudes and timings are less well known; however, restricting our analysis to only the eruption years since 1500 that correspond to historically known large eruptions in Table 1.1 (10 northern hemisphere, 11 southern hemisphere eruption years) results in the same general pattern of width reductions at mid- to high-northern latitudes (Figures 1.7 and 1.8; cf. Figure 1.5a).

1.5 Discussion

1.5.1 Does diffuse light enhance forest NPP?

We found no increase in NPP in our data set immediately following eruptions over the past millennium. Our findings suggest that for extratropical trees, any diffuse light growth enhancement is offset by other, deleterious consequences of eruptions, such as summer cooling and a decrease in the length of the growing season.

Tree rings provide a method of assessing NPP changes after eruptions that complements field-level eddy covariance measurements of net carbon uptake such as those which provided evidence for an increase in photosynthesis rates following Pinatubo [*Gu et al.*, 2003]. While eddy covariance measurements provide near-instantaneous rates of net ecosystem carbon exchange, a tree ring provides a measure of plant growth integrated over weeks to months. There are a number of possible reasons that tree ring analysis and eddy covariance might lead to different conclusions about the effect of

eruptions on forest carbon uptake. Modeling of forest diffuse-light response suggests that increased aerosol scattering may enhance photosynthesis under clear conditions but impede photosynthesis on cloudy days [*Cohan et al.*, 2002]. Even assuming substantial overall diffuse light enhancement of photosynthesis, aerosol-induced climate change such as nocturnal warming [*Roderick and Farquhar*, 2002] raising nighttime plant respiration and overall cooling resulting in delayed onset and early end of the growing season may lead to a smaller increase, or a decrease, in annual NPP. As proxies for NPP, tree rings have the additional advantages of straightforward replication and extension, permitting assessment of NPP changes over large spatial and temporal distances, and of providing a means to evaluate the effect of eruptions on individual tree species and habits within a canopy.

Using tree rings as a proxy for NPP following eruptions also has limitations. Diffuse light growth enhancement would be expected to be most pronounced for closed-canopy forests with high leaf area indices [*Roderick et al.*, 2001], and presumably especially significant for understory plants with more leaves shaded from direct light. The format of the ITRDB did not allow us to group trees by canopy leaf density, and tree ring chronologies measured for climate reconstructions generally use dominant rather than understory trees [*Fritts*, 1976]. Analyses of ring-width series carefully chosen to represent different canopy leaf area indices and tree positions within the canopy may be able to build on our findings and more sensitively assess the magnitude of diffuse-light growth enhancement on a forest-wide basis. Also, few ring chronologies are available for tropical forests. The development of more tropical ring chronologies [*Worbes*, 1999] may soon allow an assessment of the effect of volcanic eruptions on tropical tree growth.

Finally, the magnitude of growth enhancement that an analysis like ours can detect is limited by interannual variability in ring width due to other factors. While our uncertainties are small enough that we would likely have detected the 7% increase in global wood production lasting 1-2 years after Pinatubo-scale eruptions that *Roderick et al.* [2001] hypothesized, our analysis lacked the power to detect a smaller growth enhancement or a merely regional one.

An additional source of uncertainty in our analysis comes from the volcanic aerosol time series used to construct our list of eruption years. Even assuming no error in the ice core datings, sulfate levels from any one core reflect imperfectly eruption sulfur emissions. Sulfur deposition over the Antarctic after Pinatubo varied ~20% even over a few km [*Jihong and Mosley-Thompson*, 1999] and sulfate loading for well-documented eruptions such as Novarupta 1912 is undetectable in some Greenland cores while substantial in others [*Zielinski*, 1995; *Zielinski et al.*, 1997]. An index of past aerosol optical depth that includes information from more ice cores measured at high resolution along with atmospheric observations (e.g., of eclipses [*Stothers*, 2002]) is desirable and would likely improve our precision in determining volcanic aerosol effects on tree growth.

Eddy covariance and tree rings each have advantages and drawbacks in measuring forest parameters relevant to uptake of atmospheric carbon. Ultimately, combining techniques such as eddy covariance that measure instantaneous carbon fluxes with techniques such as tree-ring analysis that retrospectively measure biomass accumulation offers the best prospects for understanding the full impacts of volcanic eruptions and changes in diffuse light fraction on photosynthesis rates, NPP, and carbon uptake.

1.5.2 Why is there a decade-length decrease in tree growth following eruptions?

Ring narrowing for ≥10 years following eruptions has been reported at individual high-latitude and alpine sites [*Scuderi*, 1990; *Gervais and MacDonald*, 2001]. This study shows that narrower rings occur after eruptions across a broad array of middle- and high-latitude northern trees with the period of decreased growth lasting considerably longer than would be expected from the initial aerosol radiative forcing.

Trees that grow in cool-summer climates are often temperature-limited, so that their ring widths correlate well with annual mean and particularly summer temperatures. Invoking the cooling observed in the summers following eruptions [*Groisman*, 1992; *Robock and Mao*, 1995; *Hansen et al.*, 1996] as the major cause for ring width departures following eruptions explains the latitudinal distribution of ring narrowing well. A reduction in temperature would not reduce growth in more temperate sites that are not temperature-limited, such as most of those in the 30°-45° N band. In fact, for trees in this band that grow in more xeric climates, cooling might result in growth *enhancement* due to a reduction in water stress, although we did not find significant growth enhancement for the band as a whole after eruptions.

Unlike trees in the 45°-60°N band, trees at the equivalent latitudes in the southern hemisphere did not show a significant growth reduction (Table 1.2). The greater marine influence on land climate might produce less severe post-eruption cooling in the southern as compared to the northern midlatitudes. However, since the departures for the two

bands are the same within error, interhemispheric differences in tree response remain conjectural.

Volcano-derived stratospheric aerosols have an initial e-folding time of ~1 year (Figure 1.6a) [*Robock*, 2000], and large eruptions result in reductions in measured global temperatures lasting 2-3 years (Figure 1.6b) [*Sear et al.*, 1987] and changes in $\delta^{18}O$ of Greenland snow indicating cooling for ~2 years following the deposition of volcanic sulfur [*Stuiver et al.*, 1995]. The effect found here on ring width lasts longer, peaking at ~4-6 years and lasting on average for 8 years (Figure 1.6c). This raises the question of whether post-eruption cooling can explain this effect. To do so would require either cooling lingering more than ~3 years after eruptions or a lag of several years between cooling and tree growth reduction.

The climate impact of eruptions is not uniform but has distinctive seasonal and regional patterns [*Lough and Fritts*, 1987; *Groisman*, 1992; *Robock and Mao*, 1995; *D'Arrigo and Jacoby*, 1999] and it is possible that some mid- and high-latitude cooling can last considerably longer than 2-3 years. Thus, an examination of glacier movements has suggested that eruptions trigger decade-long episodes of glacial advance [*Porter*, 1986]. A spectral analysis of global temperature fields since 1950 raises the possibility that eruptions cause long-term climate perturbations through persistent El Niño -like ocean temperature patterns [*Lee and Fang*, 2000], and a long-lasting ocean effect is consistent with models of the land-ocean response to radiative forcing [*Lindzen and Giannitsis*, 1998]. Up to decadal-scale ocean cooling tentatively linked to volcanic eruptions has also been found in a study of south Pacific coral [*Crowley et al.*, 1997].

Nevertheless, it appears puzzling that the maximum growth reduction seen in this study lags by several years the period of maximum eruption cooling.

Tree wood increment is often largely based on previous-year productivity, so that a period of distinctive climate conditions will affect ring width for several years afterwards [*Fritts*, 1976]. For evergreen needleleaf trees, the multiyear needle lifetime means that the effect of previous-year climate is particularly pronounced [*Jacoby et al.*, 1996]. However, the large width reduction found for larch (Figure 1.4c), which are deciduous (cf. *Colenutt and Luckman* [1996]), suggests that needle retention cannot be the primary explanation for the response lag.

For trees growing on permafrost, permafrost encroachment on tree roots following even one or two abnormally cool summers [*Romanovsky and Osterkamp*, 1997] may persist in subsequent years due to the long response time of soil temperature to surface temperature changes. Shallower thaws may cause water and nutrient stress because more of the trees' roots remain frozen during the growing season. This is an attractive explanation for the particularly large width reduction observed in larch in our data set, many of which grew within the Siberian permafrost zone (cf. *Kobak et al.* [1996]). In very moist environments cool summers may similarly lead to nutrient limitation following root damage from waterlogging, as has been suggested for Irish oaks [*Baillie and Munro*, 1988].

Carbon in wood deposited from trees under drought stress due to permafrost encroachment following eruptions would be predicted to show reduced discrimination against ^{13}C (e.g. *Hubick and Farquhar* [1989]) in rings following eruption years. Similarly, nutrient stress due to permafrost encroachment or flooding might be expected

to result in reduced discrimination against ^{15}N (e.g. *McKee et al.* [2002]). Variations in tree ring carbon and nitrogen isotope ratios have been used to deduce changes in tree water and nutrient status in response to such factors as arctic warming, increased ambient CO_2, and acid rain [*Leavitt and Long*, 1991; *Bert et al.*, 1997; *Penuelas and Estiarte*, 1997; *Tang et al.*, 1999; *Barber et al.*, 2000]. Measurements of the composition of rings formed around volcanic events can thus potentially test whether drought stress, nutrient stress or other factors are significantly affecting tree physiology following eruptions.

The work of *Braswell et al.* [1997], which shows a 2-year lag between changes in mean surface temperature and NDVI-derived vegetation extent in a number of biomes, and a similar lag between changes in mean surface temperature and the reduction of CO_2 growth rates at Mauna Loa and the South Pole, suggests a positive correlation between temperature and lagged NPP. A 2-year or perhaps somewhat longer lag between temperature and NPP changes for northern forests is consistent with our findings as well. *Braswell et al.* [1997] suggest temperature-sensitive heterotrophic nutrient cycling as a mechanism by which a temperature change leads to a delayed change in NPP. Analyses of tree ring isotopic composition may be able to test whether cooling indeed affects tree nutrient status.

1.6 Conclusions

In our analysis of tree ring widths, including over 40,000 cores from more than 1000 sites, we find evidence for a decrease in northern forest NPP following eruptions. This decrease appears at least initially to be a consequence of the surface cooling effects of volcanic aerosols. Some additional feedback mechanism is required to explain the observed persistence of this reduced growth for several years beyond the cooling peak.

Our finding of no significant increase in wood accumulation around eruption years favors lower soil respiration rather than increased plant growth as the main factor in northern forest post-Pinatubo carbon uptake. Diffuse light enhancement of growth of temperate understory trees and herbaceous plants, or of tropical vegetation, is still possible; the importance to plants of light relative to temperature would be expected to increase moving into deep shade and towards the tropics, and may have been greater after Pinatubo than after earlier eruptions because of warming in recent decades. Eruption-induced ocean fertilization [*Watson*, 1997] and tropical fire suppression (cf. *Langenfelds et al.* [2002]) provide additional possible avenues for carbon uptake.

Table 1.1. Eruption years used in this study (defined as years with high atmospheric levels of volcanic aerosol) and the possible responsible historical eruptions

	optical depth[b]		eruption description[c]					
eruption year[a]	NH	SH	volcano	locality	beginning month/year	latitude	longitude	VEI[d]
1026	0.11		Sheveluch	Kamchatka	1000±50	56.7N	161.4E	5
			Billy Mitchell	Bougainville	1030±25	6.1S	155.2E	5
1058	0.15		Baitoushan	China	1050±10	42.0N	128.1E	7
1175	0.23		Okataina	New Zealand	1180±20	38.1S	176.5S	5
1229	0.17							
1259	0.39							
1285	0.13							
1295	0.12							
1329	0.10							
1453	0.15		Kuwae	Vanuatu	1452±10	16.8S	168.5E	6
1460	0.15							
1586		0.19	Kelut	Java	1586	7.9S	112.3E	5
1587	0.15							
1594		0.09	Raung	Java	1593	8.1S	114.0E	5
1600		0.16	Huaynaputina	Perú	2/1600	16.6S	70.9W	6
1601	0.18							
1622	0.10							
1641	0.18		Komaga-take	Japan	7/1640	42.1N	140.7E	5
			Parker	Phillipines	12/1640	6.1N	124.9E	5
1674	0.11		Gamnokara	Halmahera	5/1673	1.4N	127.5E	5
1693		0.10	Hekla	Iceland	2/1693	64.0N	19.7W	4
			Serua	Indonesia	6/1693	6.3S	130.0E	4
1695	0.12	0.14						
1729	0.11							
1783	0.11	0.09	Grímsvötn	Iceland	5/1783	64.4N	17.3W	4
			Asama	Japan	5/1783	36.4N	138.5E	4
1809	0.18							
1810		0.28						
1815	0.20	0.67	Tambora	Sundas	4/1815	8.3S	118.0E	7
1831	0.16		Babuyan Claro	Phillipines	1831	19.5N	121.9E	4
1836		0.19	Cosiguina	Nicaragua	1/1835	13.0N	87.6W	5
1883	0.12		Krakatau	Indonesia	8/1883	6.1S	105.4E	6
1884		0.09						
1902	0.12		Santa Maria	Guatemala	10/1902	14.8N	91.6W	6
1951		0.09	Ambrym	Vanuatu	12/1950	16.2S	168.1E	4
			Lamington	New Guinea	1/1951	9.0S	148.2E	4
1963		0.10	Agung	Bali	3/1963	8.3S	115.5E	4
1983	0.10		El Chichón	México	3/1982	17.4N	93.2W	5
1992	0.12	0.12	Pinatubo	Phillipines	6/1991	15.1N	120.4E	6

a.   *italics*: northern hemisphere volcanic aerosol peak, **bold**: southern hemisphere.
b.   NH: northern hemisphere, SH: southern hemisphere. Optical depths from *Crowley* [2000] and *Robertson et al.* [2001] respectively, except for the 1992 southern hemisphere value which is from *Sato et al.* [1993], and were used to define the eruption years in Column 1.

c.   Likely contributing eruptions compiled from *Simkin and Siebert* [1994] as updated at
http://www.volcano.si.edu/gvp/world/ . Note that in many cases the most important contributing eruption is uncertain or
unknown; the location and date of a contributing eruption were not directly used in compiling the list of eruption years in
Column 1, which is based on ice core rather than historical eruption records.

d.   VEI = Volcanic Explosivity Index [*Simkin and Siebert*, 1994]; 4 is "large", 5 and up "very large".

Table 1.2: Ring width departures following eruption years

| site grouping | number of sites | number of cores | ring widths, % difference from average (±SE)[a] | | | |
| | | | equal weighting[b] | | weighting by NPP[c] | |
			years 0-1	years 0-8	years 0-1	years 0-8
all N of 60°N	259	7948	-3.4 ±2.6	-5.0** ±1.4	-4.0* ±2.7	-5.5** ±1.5
all 45°-60°N	465	12182	0.0 ±0.9	-1.9* ±0.8	0.0 ±0.9	-2.1* ±1.0
all 30°-45°N	527	15893	0.5 ±1.2	0.4 ±0.9	1.1 ±0.9	0.4 ±0.8
all 30°-45°S	144	4242	2.1 ±1.5	-0.9 ±1.3	3.0 ±1.4	-0.6 ±1.5
all 45°-56°S	31	890	-0.4 ±3.1	-3.5 ±1.3	0.6 ±3.1	-3.3 ±1.8
N of 45°N:						
spruce	267	7226	-1.3 ±2.5	-2.9** ±1.7	-1.5 ±2.0	-2.7** ±1.4
pine	148	4612	-1.5 ±1.5	-3.1** ±0.7	-0.7 ±1.5	-3.1** ±0.9
larch	104	3090	-6.3* ±2.8	-7.2** ±1.8	-7.0** ±2.7	-7.2** ±1.8
oak	72	1826	2.6 ±2.2	-0.7 ±2.1	2.0 ±1.9	-0.4 ±2.2
all trees	723	20101	-1.6 ±1.3	-3.2** ±0.8	-1.3 ±1.3	-3.1** ±0.9

a. *: p ≤ .05, **: p ≤ .01 (probabilities derived from Monte Carlo resampling).
b. Average of sites within a grouping, weighted equally.
c. Sites averaged by 1° x 1° cell and weighted by contemporary NPP per unit area [*Randerson et al.*, 1997] for that cell.
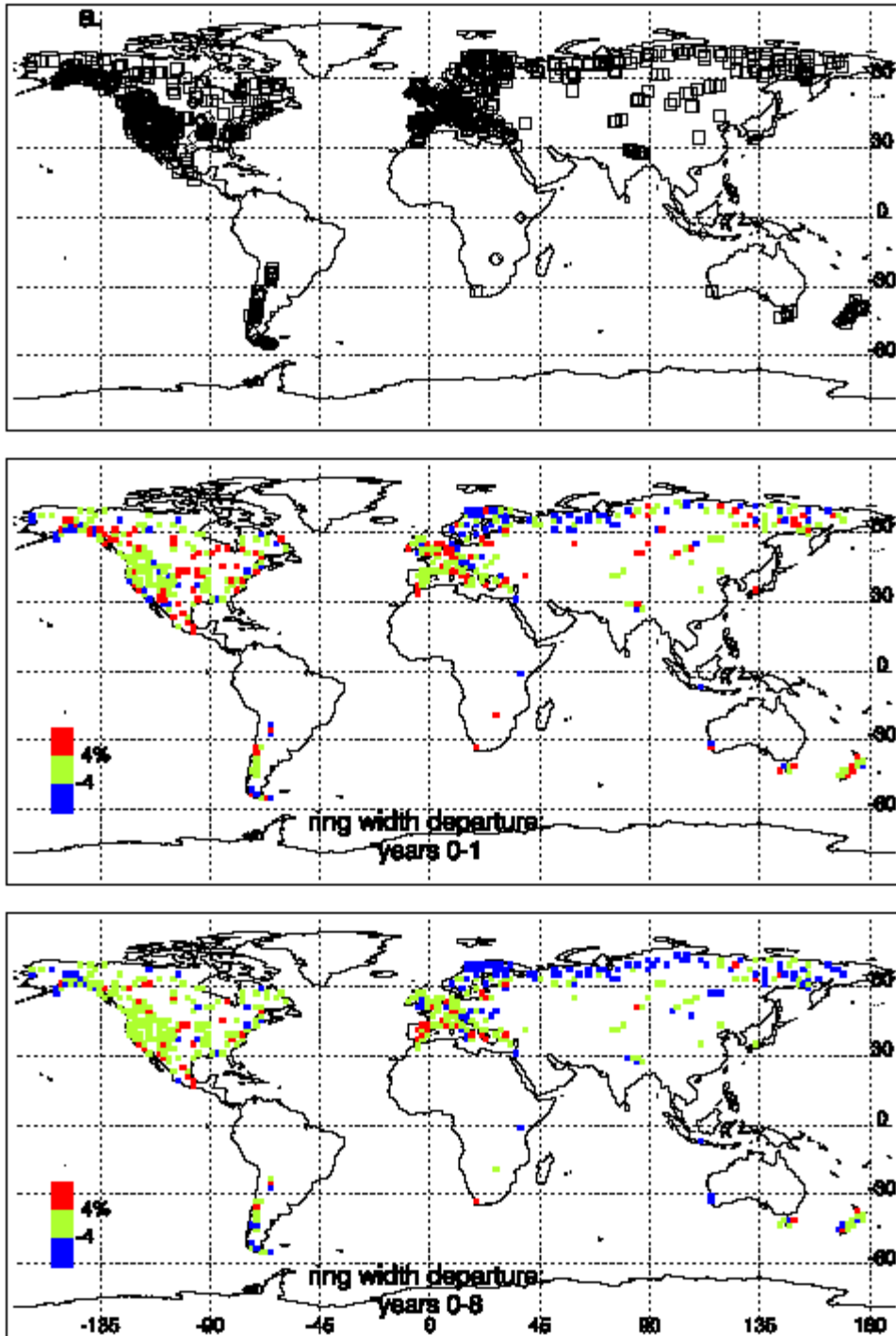
Figure 1.1. (a) Location of sites used for this analysis (n = 1498). Symbols indicate tree type: needleleaf (squares) or broadleaf (diamonds). (b) Ring widths for years 0 through 1 following eruption years compared with the long-term average. Site responses were averaged over 2° x 2° cells. (c) Ring widths for years 0 through 8 following eruption years compared with the long-term average. Note the preponderance of negative width departures at mid- and high northern latitudes.
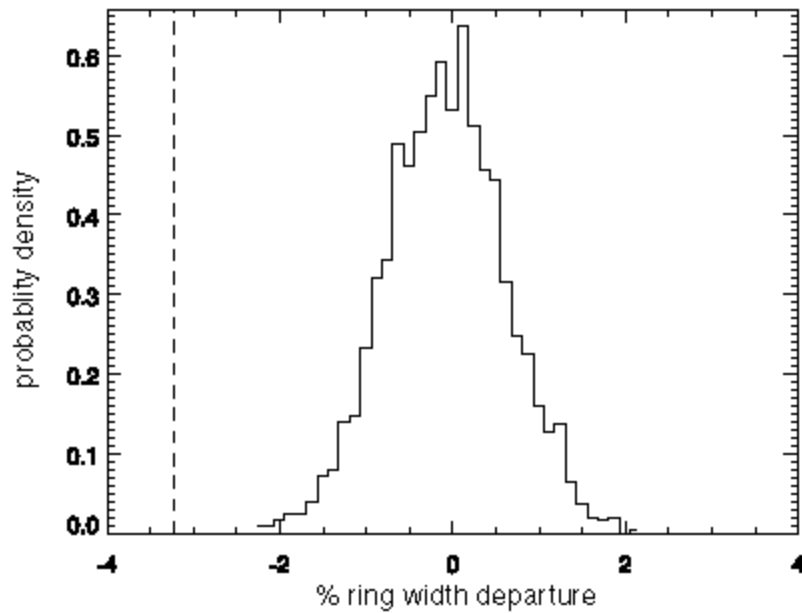
Figure 1.2. An example of the Monte Carlo method used to test regional width departures for significance: the width departure for sites north of 45° N for years 0-8 following eruption years (dashed line) is compared to the distribution of width departures from the same sites following 1000 sets of random "eruption years" (histogram). Here the negative departure is significant, $p < 0.001$.
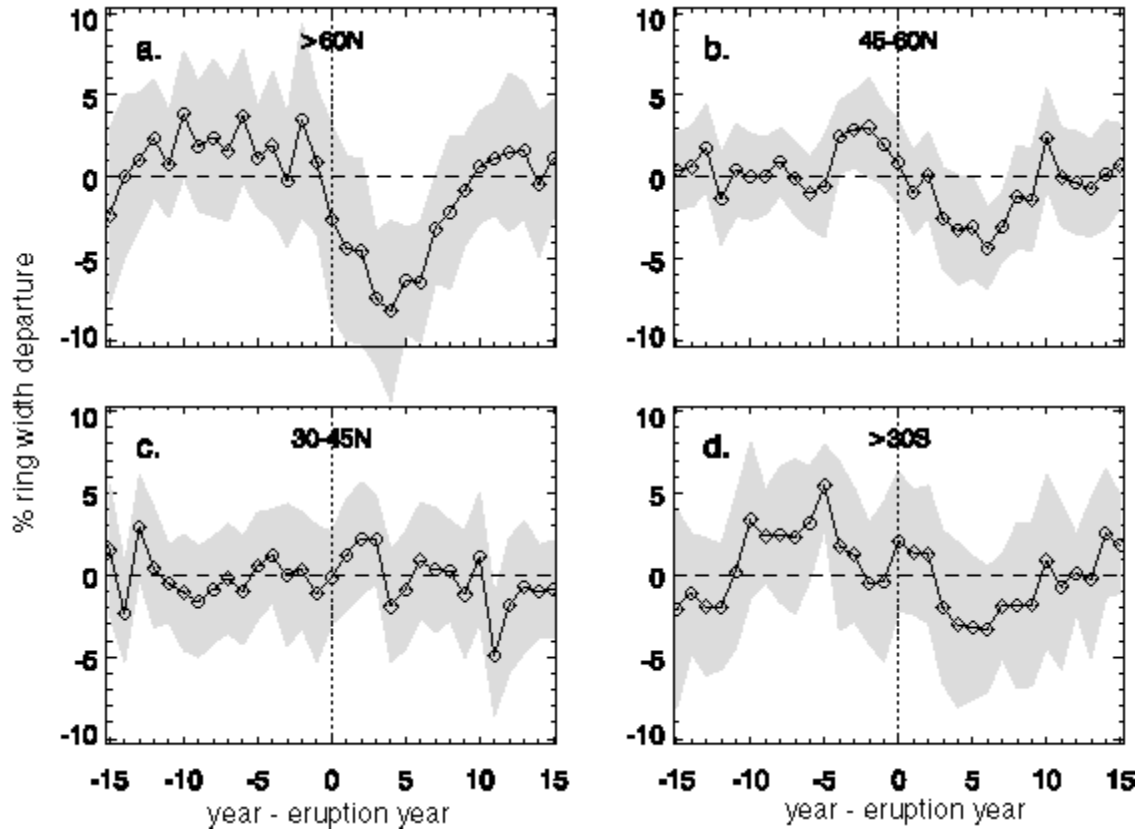
Figure 1.3. (a-d) Mean ring width departures around eruption years, by latitude zone (with the 30°-45° S and 45°-56° S zones combined). Shading shows 2-standard-error confidence limits based on the variation across eruption years. Because width departures are expressed relative to a centered moving average, zones that have substantial negative departures following eruption years tend to show positive departures preceding eruption years. See Table 1.2 for number of sites and significance levels of departures for each zone. Table 1.1 lists the eruption years used.
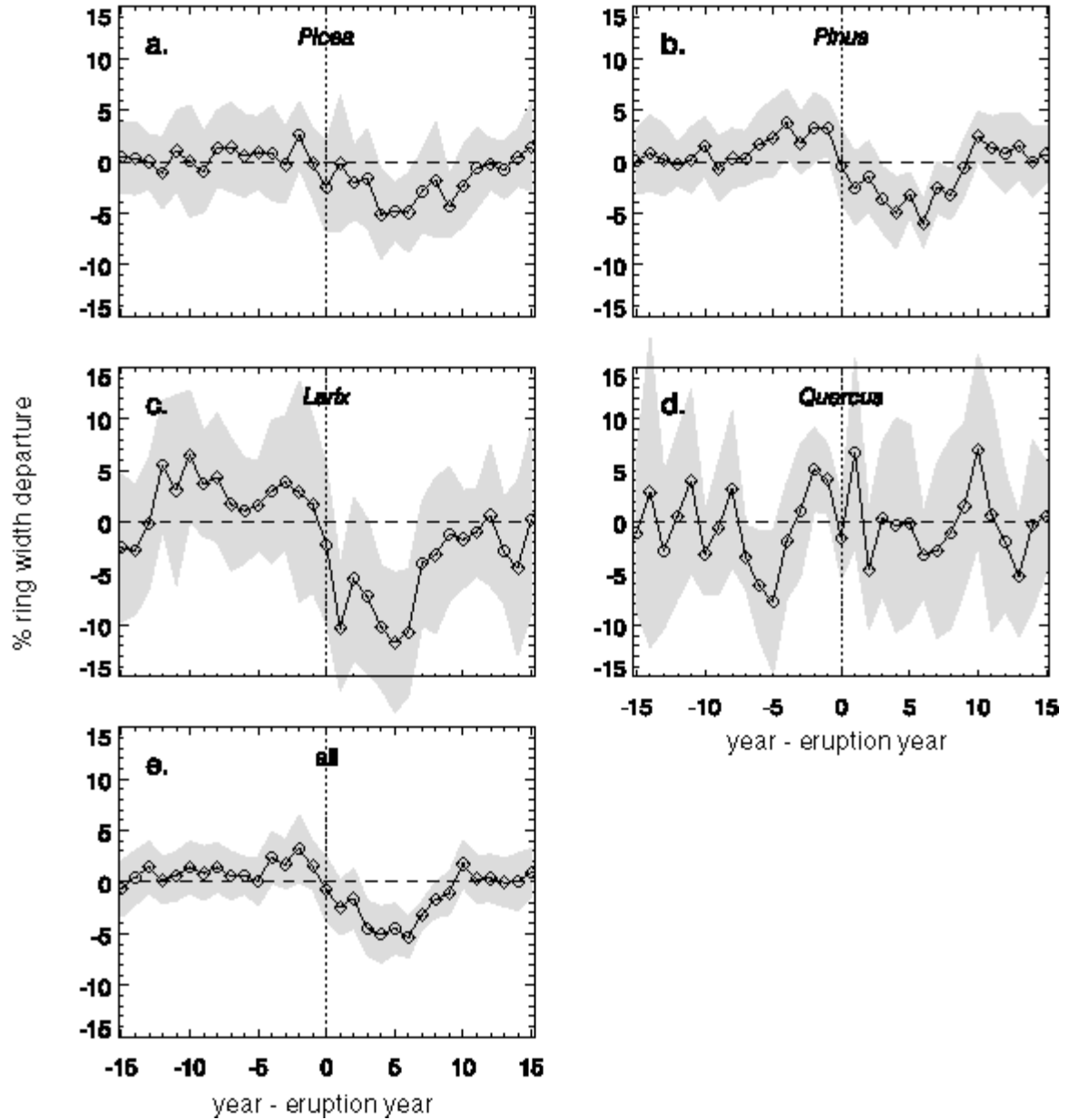
Figure 1.4. (a)-(e) Mean ring width departures around eruption years among sites north of 45° N, for the most common tree genera in the database (a)-(d), and mean of all sites north of 45° N (e). Shading shows 2-standard-error confidence limits based on the variation across eruption years. See Table 1.2 for number of sites and significance levels of departures for each group. Table 1.1 lists the eruption years used.
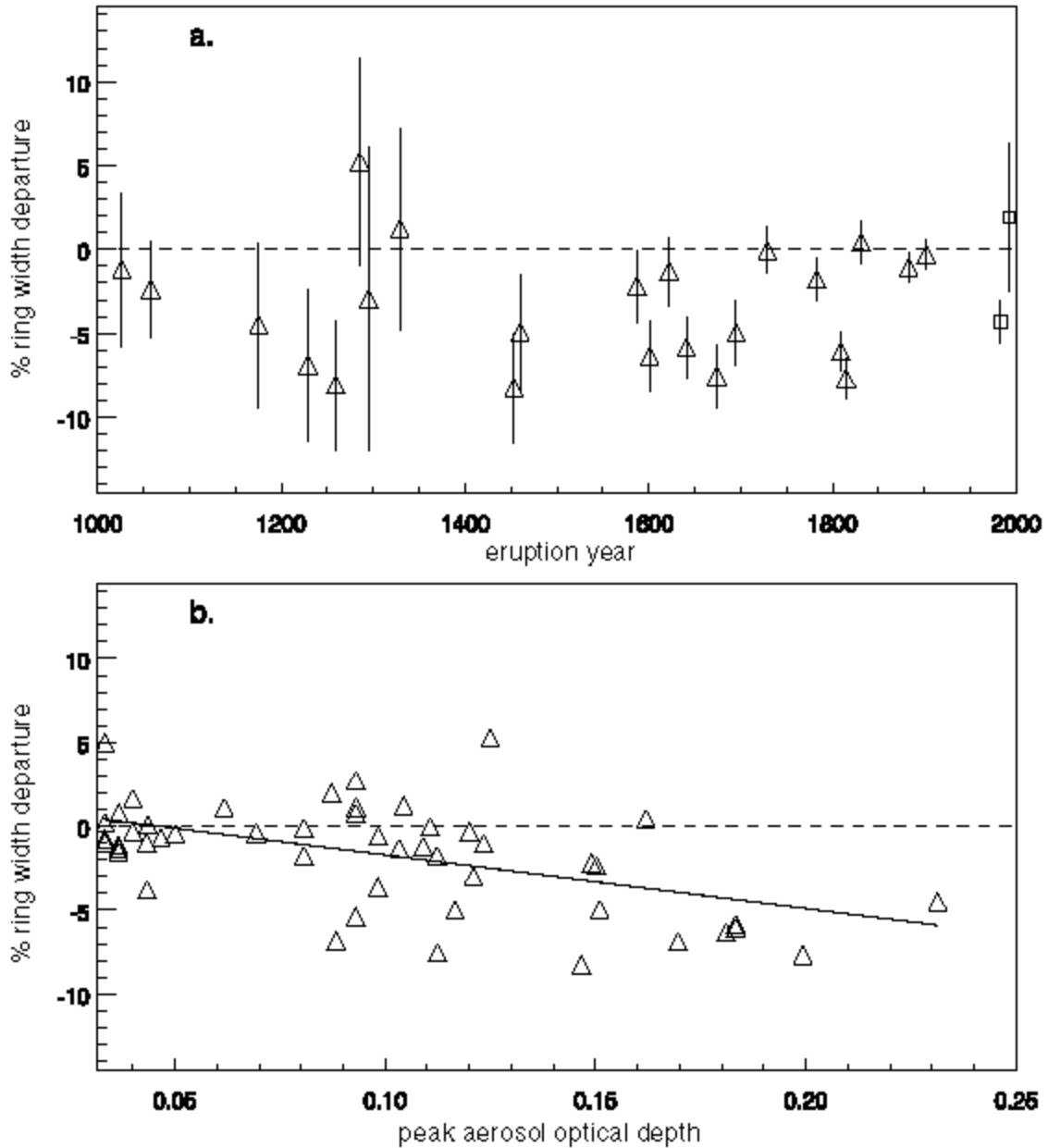
Figure 1.5. Year 0-8 ring width departure, mean of sites north of 45° N, by individual northern hemisphere eruption year. (a) Triangles: years considered in our averaging of width departures across eruptions (optical depth > 0.1; n = 23) plotted by date. Error bars show standard error across sites. These are larger for the earliest eruptions considered because fewer site chronologies exist for the early part of the period. Squares: the Chichón and Pinatubo eruptions, with ring widths normalized against the last 41 years of data for each tree rather than the centered 41-year moving average used for earlier eruptions. Note that the pattern of a width decrease after eruptions is consistent across centuries. (b) For all aerosol optical depth peaks with magnitude 0.033-0.250 (n = 51) as a function of the optical depth. High peak optical depth correlates with negative width departures. A linear fit of the relationship is drawn: y = 1.5 – 31.9x, weighted R^2 = 0.36 (p < 0.01 [Student's t test]).
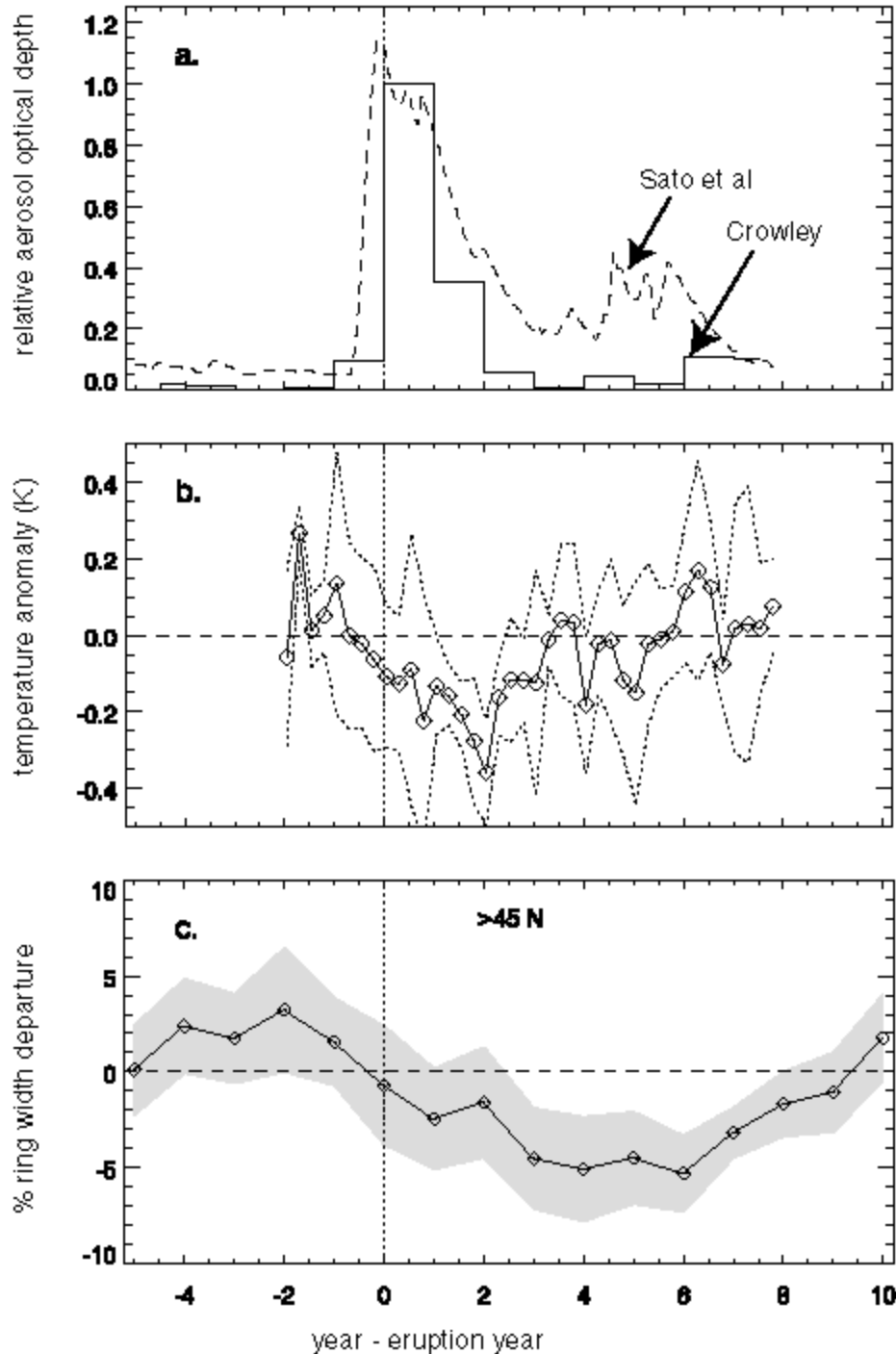
Figure 1.6. Timescale of responses after large eruptions: a) Aerosol optical depth as a fraction of that for the eruption year – mean of 25 eruptions since 1000 from *Crowley* [2000] (northern hemisphere) and globally by month median of 5 large eruptions since 1880 from *Sato et al.* [1993] (http://www.giss.nasa.gov/data/strataer/). The peak shows an initial approximately 1 y decay time, although a fraction of the aerosols appears to last several years. b) Solid line: mean seasonal northern hemisphere surface temperature anomalies around the 5 eruptions since 1880, calculated from the temperature

compilation of *Hansen et al.* [1999] (http://www.giss.nasa.gov/data/update/gistemp/).
Dotted lines: mean ± 1 standard deviation. c) Ring widths among trees north of 45° N for
eruptions since 1000 (this study) – same data as Figure 1.4e. Comparing panels b and c,
the lag between the peak post-volcanic temperature and ring width departures can be
seen.
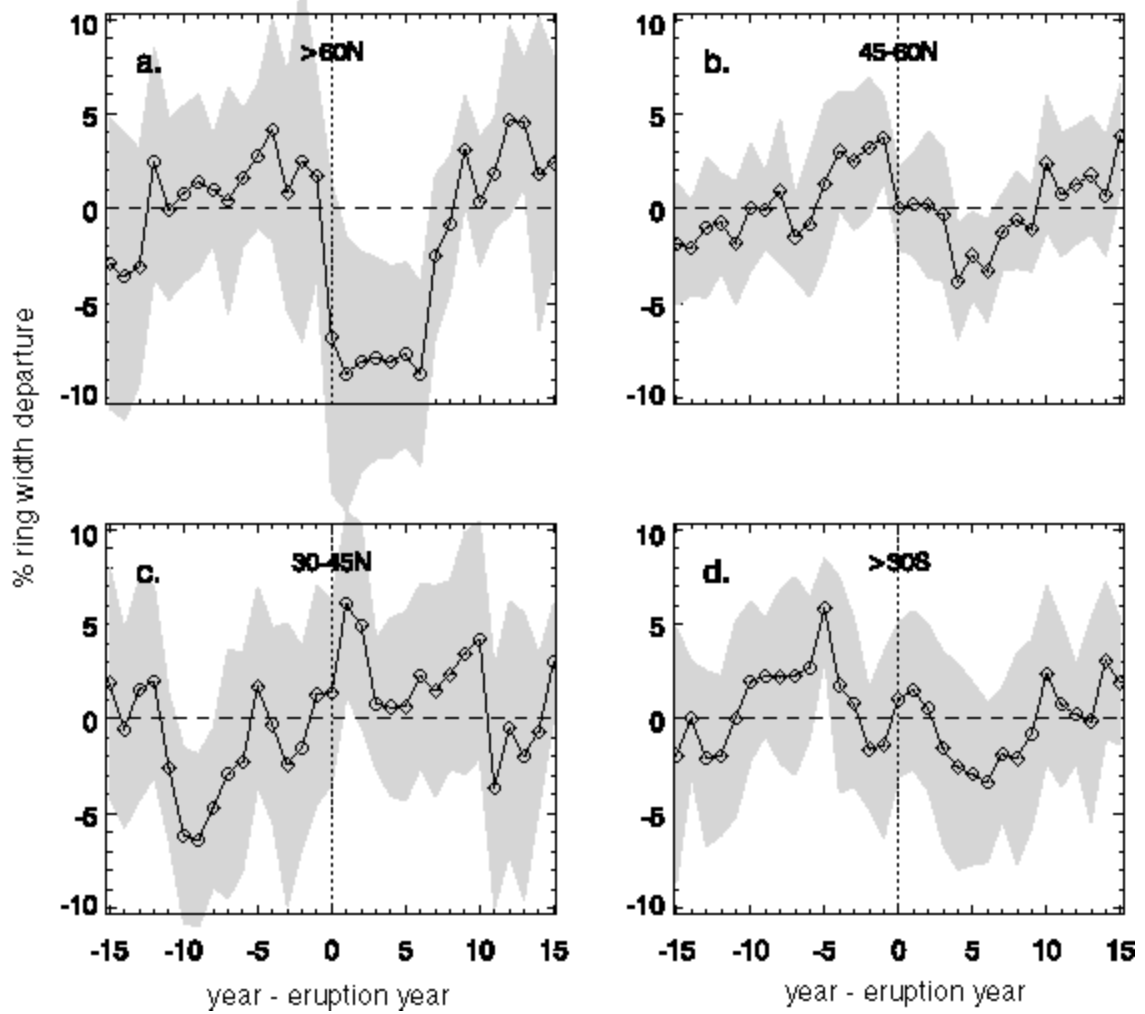
Figure 1.7. Same as Figure 1.3 but using only eruption years since 1500 that follow within 2 years of a known large eruption (Table 1.1). The eruption years used are as follows: northern hemisphere, 1587, 1601, 1622, 1641, 1695, 1783, 1815, 1831, 1883, 1902; southern hemisphere, 1586, 1594, 1600, 1693, 1695, 1783, 1815, 1836, 1884, 1951, 1963. Note that the shape of width reduction north of 45° N is quite similar to that in Figure 1.3.
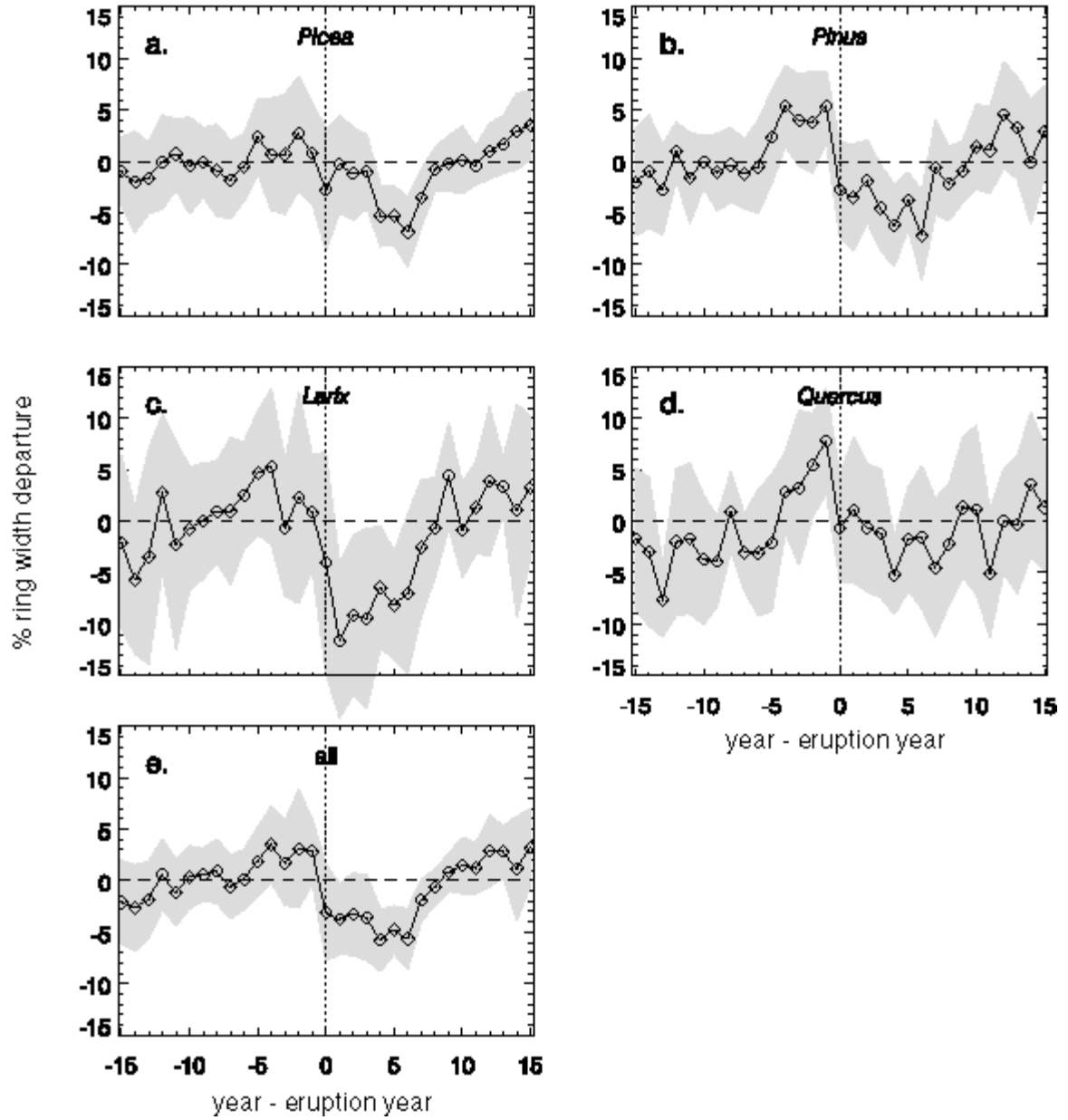
Figure 1.8. Same as Figure 1.4 but using only eruption years since 1500 that follow within 2 years of a known large eruption (Table 1.1). The years used are the northern hemisphere list in the caption to Figure 1.7.

Chapter 2: Selecting Parameters in Inversions for Regional Carbon

Fluxes by Generalized Cross-Validation

2.1 Abstract

Estimating CO_2 fluxes from the pattern of atmospheric CO_2 concentrations with atmospheric transport models is an ill-posed inverse problem, whose solution is stabilized using prior information. Weights assigned to prior information and to CO_2 concentrations at different locations are quantified by parameters that are not well known, and differences in the choice of these parameters contribute to differences among published estimates of the regional partitioning of CO_2 fluxes. Following the TransCom 3 protocol to estimate CO_2 fluxes for 1992-1996, we find that the partitioning of the CO_2 sink between land and oceans and between North America and Eurasia depends on parameters that quantify the relative weight given to prior flux estimates and the extent to which CO_2 concentrations at different stations are differentially weighted. Parameter values that minimize an estimated prediction error can be chosen by generalized cross-validation (GCV). The GCV parameter values yield fluxes in northern regions similar to those obtained with the TransCom parameter values, but the GCV fluxes are smaller in the poorly constrained equatorial and southern regions.

2.2 Introduction

To complement direct measurements of, for example, land or ocean carbon uptake, inverse modeling is widely used to estimate CO_2 fluxes from the observed spatial and temporal variations of atmospheric CO_2 concentrations. Different inverse modeling studies, however, have reached apparently contradictory conclusions on the longitudinal and land/ocean partitioning of CO_2 fluxes. For example, studies using similar data sets have variously placed a sink of order 1 Pg C yr^{-1} in temperate North America [*Fan et al.*,

1998], in north Asia [*Bousquet et al.*, 1999a], or in the north Atlantic and Pacific [*Rayner et al.*, 1999].

Estimating CO_2 fluxes involves the solution of a linear system

$$\mathbf{Ax} = \mathbf{b} + \boldsymbol{\varepsilon}, \tag{1}$$

where $\mathbf{b}$ is a vector of observed variations in CO_2 concentrations, $\boldsymbol{\varepsilon}$ is a vector of random errors with zero mean and with covariance matrix $\mathrm{cov}(\boldsymbol{\varepsilon}) = \mathbf{C}_b$, $\mathbf{x}$ is an unknown vector of CO_2 fluxes, and $\mathbf{A}$ is a transport operator that relates CO_2 fluxes to CO_2 concentrations.

The solution of this inverse problem is generally not well constrained by the CO_2 concentrations (i.e., the problem is ill-posed) and must be stabilized through the use of prior information or regularity constraints [e.g., *Hansen*, 1998]. Estimates of CO_2 fluxes are usually constrained to be close to CO_2 fluxes specified *a priori* [e.g., *Enting*, 2002] by minimizing an object function of the form

$$J = (\mathbf{Ax} - \mathbf{b})^T \mathbf{C}_b^{-1}(\mathbf{Ax} - \mathbf{b}) + \lambda^2(\mathbf{x} - \mathbf{x}_0)^T \mathbf{C}_x^{-1}(\mathbf{x} - \mathbf{x}_0), \tag{2}$$

consisting of the sum of the least squares object function (first term) and a penalty term (second term) that penalizes deviations of the solution $\mathbf{x}$ from a given prior estimate $\mathbf{x}_0$. The covariance matrix $\mathbf{C}_x$ represents uncertainty about the prior estimate $\mathbf{x}_0$, and the regularization parameter λ sets the weight of the term involving the prior information relative to the least squares term. (See also the Appendix.)

In CO_2 inversions, the covariance matrices $\mathbf{C}_b$ and $\mathbf{C}_x$ are usually taken to be diagonal, with diagonal entries $\mathbf{c}_b$ and $\mathbf{c}_x$ equal to assumed variances of the local CO_2 concentration errors and of the regional prior flux distributions. The prior fluxes $\mathbf{x}_0$ and their assumed variances $\mathbf{c}_x$ are typically chosen *ad hoc* from a range of reasonable values, as are the error variances $\mathbf{c}_b$ of the CO_2 concentrations. It is known that inversion results

can sensitively depend on the choice of such inversion parameters [*Bousquet et al.*, 1999b; *Rayner et al.*, 1999; *Law et al.*, 2003], but a unified approach to quantifying this source of uncertainty and to choosing inversion parameters systematically has not been pursued.

Several methods are available to choose inversion parameters systematically [e.g., *Hansen*, 1998, chapter 7]. One method applied in inverse problems in such fields as meteorological data assimilation [*Wahba et al.*, 1995] and geodesy [*Ditmar et al.*, 2003] is generalized cross-validation (GCV) [*Golub et al.*, 1979]. A form of leave-one-out cross-validation, GCV chooses parameters by minimizing an estimated mean-squared error of predictions with the model specified by the parameters. For the CO_2 problem, this means that GCV chooses inversion parameters by minimizing an estimated mean-squared error of predictions of CO_2 concentrations given estimated CO_2 fluxes and the model of atmospheric transport. Although such predictions are generally not the objective of inverse modeling of CO_2 fluxes, GCV provides a useful heuristic for choosing inversion parameters.

We applied GCV to estimate two parameters in the TransCom 3 framework for inverse modeling of CO_2 fluxes [*Gurney et al.*, 2002]. The two inversion parameters considered control the weighting of the prior flux estimates and the relative magnitudes of error variances of CO_2 concentrations at different locations. We examine how the CO_2 flux estimates depend on the values assigned to these parameters, choose parameter values by GCV, and discuss how the flux estimates thus obtained differ from those obtained with the original TransCom parameter values.

2.3 Methods

    2.3.1 Inverse modeling framework

The TransCom 3 annual-mean inversion [*Gurney et al.*, 2002] uses measured CO_2

concentrations to estimate CO_2 fluxes from 11 land and 11 ocean regions after

subtracting the estimated effects of fossil fuel emissions, of ocean carbon uptake, and of

covariances between the seasonality of the biosphere and that of atmospheric transport

(the seasonal "rectifier effect"). The data used are the mean 1992-1996 CO_2

concentrations at 76 stations and the mean growth rate of atmospheric CO_2

concentrations during that period, the latter constraining the sum of the regional fluxes.

We followed the TransCom 3 protocol except for excluding one station, Darwin, whose

mean concentration is anomalously high and apparently reflects local sources [*Law et al.*,

2003], leaving 75 stations. (The TransCom 3 data and flux patterns are available at

http://transcom.colostate.edu/TransCom_3/T3_Input_Data/. The prior fluxes and

variances used in the TransCom 3 inversion are given in the online supplement to *Gurney*

et al. [2002].)

      The transport operator **A** for this inverse problem specifies the modeled impact

of the magnitude of each of the TransCom 3 regional flux patterns on each data point. We

modeled atmospheric CO_2 transport with the Model of Atmospheric Transport and

Chemistry (MATCH) [*Rasch et al.*, 1994; *Mahowald et al.*, 1997], run at T21 resolution

(about 5.5° * 5.5°) with 26 vertical levels. The model was driven with one year of winds

from a simulation with the National Center for Atmospheric Research's Community

Climate Model version 3 [*Kiehl et al.*, 1998]. In this configuration, MATCH has been

used to study column CO_2 variability [*Olsen and Randerson*, 2004]. Other configurations of MATCH participated in the TransCom model intercomparisons [*Gurney et al.*, 2003].

2.3.2 Parameters varied

Like other recent inverse modeling studies, TransCom 3 uses prior estimates of regional CO_2 fluxes to stabilize the flux estimates. The weighting assigned to the prior estimates of regional CO_2 fluxes determines the relative influence of the data and of the prior estimates on the flux estimates. Assigning a very large weight to the prior estimates leads to a solution that is close to the prior estimates and fits the data poorly; a very small weight leads to an unstable solution that typically exhibits spurious large-amplitude fluxes.

Here we scale the weighting given to the prior estimates by a parameter λ that we vary from 0.5 to 3 (Equation 2). The parameter λ can be interpreted as the regularization parameter in what is known as Tikhonov regularization or ridge regression [e.g., *Hansen*, 1998, chapter 5]. Alternatively, in a Bayesian inversion framework, the parameter λ can be thought of as a scaling factor of the prior standard deviations, so that instead of the error variances $\mathbf{c}_{x,0}$ assigned by TransCom to the prior estimates, the error variances are of the form $\mathbf{c}_x = \lambda^{-2}\mathbf{c}_{x,0}$. (See also the Appendix.)

The relative magnitudes of the error variances $\mathbf{c}_b$ assigned to the CO_2 concentration data control the relative weights of CO_2 concentrations at different locations in the inverse model. The data error variances should reflect uncertainty due to error in the transport model and error in the regional source patterns assumed in the inversion as well as measurement and calibration error [*Kaminski et al.*, 2001]. (Estimated errors in the forward model can be taken into account explicitly in the solution

of inverse problems [*Van Huffel and Vandewalle*, 1989; *Golub et al.*, 1999]. Using such methods to estimate CO_2 fluxes appears to be worth pursuing, but we will not do so here.)

Investigators have typically either assumed the same error variance for all stations [*Fan et al.*, 1998; *Rayner et al.*, 1999] or have, as in TransCom, taken the error variance at each station to be proportional to the high-frequency variance of CO_2 concentrations at the station. In fact, the error variance may well be the sum of components that scale in each of the two ways [cf. *Rödenbeck et al.*, 2003]. Therefore, we allow a gradation from uniform station error variances $c_{b, e}$ to the TransCom error variances $c_{b, 0}$ by varying a parameter τ between 0 (uniform error variances) and 1 (TransCom error variances). The i-th station variance is given by $c_b^i = (c_{b, 0}^i)^\tau (c_{b, e}^i)^{1-\tau}$, and the magnitude of the uniform error variance chosen such that the diagonal covariance matrices $\mathbf{C}_{b, e}$ and $\mathbf{C}_{b, 0}$ have the same determinant.

2.4 Results

2.4.1 Effects of parameter choices on flux estimates

The large northern land sink inferred in the TransCom 3 inversions is stable with respect to changing the parameter values, decreasing by ~25% (0.7 Pg C yr^{-1}) with increasing λ (Figure 2.1a). The longitudinal distribution of the sink changes as τ is varied (an effect noted by *Gurney et al.* [2002] as explaining part of the difference between the TransCom flux distribution and that inferred by *Fan et al.* [1998]). Most of this shift is due to two stations at the ITN tower in North Carolina [*Bakwin et al.*, 1995], whose low CO_2 concentrations imply a large North American sink but which are assigned large errors, hence little weight, in TransCom. At low τ, the North American sink is inferred to

be higher by 0.3 Pg C yr^{-1} (Figure 2.1b) and the estimated sinks in Europe (Figure 2.1c)
and Asia correspondingly decrease.

By contrast, the estimated flux distribution in equatorial and southern regions
depends strongly on the parameter values chosen. Changing λ can shift fluxes of 2 Pg C
yr^{-1} between equatorial and southern land regions (Figure 2.1d, e), with particularly large
flux magnitudes at low λ, where the prior constraints are weaker.

The sensitivity of the equatorial and southern regions' flux estimates to parameter
choices affects the global partitioning of fluxes between land and ocean. The total ocean
flux estimate varies by up to 0.8 Pg C yr^{-1} as τ is changed (Figure 2.1f), with
compensating changes in the land flux estimate. (Because of the global growth rate
constraint, the sum of land and ocean fluxes stays approximately constant at -2.8 Pg C
yr^{-1} as inversion parameters are varied.)

2.4.2 Choosing parameters by GCV

The GCV function is minimized when $\tau = 0.7$ and $\lambda = 2.1$ (Figure 2.2).
TransCom's error model ($\tau = 1$) or an intermediate error model ($0 < \tau < 1$) thus seems
more appropriate than an error model with equal error variances for all stations ($\tau = 0$).
The GCV choice of λ implies that the TransCom standard deviations of the prior fluxes
may be too large by about a factor of 2, intimating that TransCom's estimated CO_2 fluxes
overfit the data.

For northern regions, using the GCV parameter choices in place of the TransCom
parameter values changes the estimated fluxes by less than 20% (Figure 2.1a-c). For
many equatorial and southern regions (Figure 2.1d,e), however, the GCV flux estimates

are much closer to the prior values than the TransCom estimates, suggesting that the

station network provides little information about CO_2 fluxes in these regions.

2.5 Implications for future inverse-modeling studies

Parameter-choice methods such as GCV offer some scope for reducing

uncertainty in and variations between inverse modeling studies. Although selecting what

parameters to estimate will remain arbitrary, the fact that even our restricted variation of

parameters resulted in differences in estimated fluxes that are comparable to the

TransCom inter-model variation and to the *a posteriori* uncertainties estimated from the

data and prior flux uncertainties [*Gurney et al.*, 2002] suggests that choosing parameters

systematically is necessary.

GCV could be particularly useful for choosing relative weights for blocks of data

from different sources [*Gao*, 1994]. As inversions for carbon fluxes add additional types

of data, such as CO_2 isotopic composition [*Ciais et al.*, 1995; *Rayner et al.*, 1999],

spectroscopically determined column CO_2 [*Yang et al.*, 2002], and measurements of other

gases such as CO and O_2, GCV can be used to select a weighting for each type that

reflects not only measurement accuracies but also model capability to simulate each type

of data.

2.6 Conclusion

The choice of parameters can significantly contribute to variations in CO_2 flux

estimates obtained in inverse modeling studies. Methods such as GCV that choose

parameters systematically by optimizing a given objective function can improve

inversion results. We recommend that uncertainty in inversion parameters be considered in future inverse modeling protocols and that formal parameter choice methods be used where appropriate.
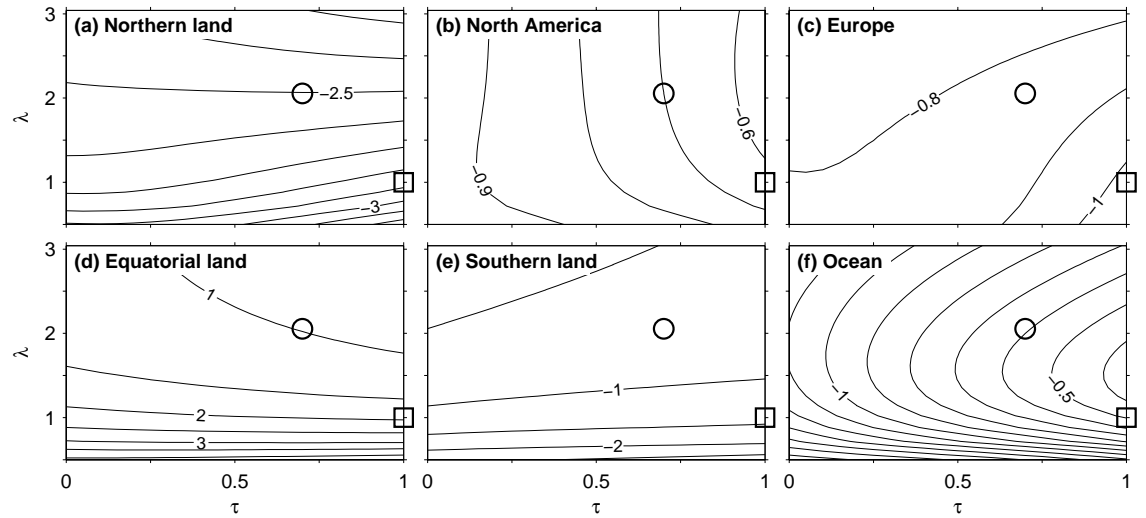
Figure 2.1. CO_2 fluxes (Pg C yr^{-1}) as a function of the inversion parameters. The contour interval is 0.1 Pg C yr^{-1} in panels (a)-(c) and (f) and 0.5 Pg C yr^{-1} in panels (d)-(e). Positive values represent flux into the atmosphere. The circle marks the parameter values chosen by generalized cross-validation. The square marks the original TransCom parameter values. (a) Sum of the TransCom northern land regions; (b) North America (sum of the TransCom temperate North America and boreal North America regions); (c) the Europe TransCom region; (d) sum of the TransCom equatorial land regions (northern South America, northern Africa, and southeast Asia); (e) sum of the TransCom southern land regions (southern South America, southern Africa, and Australia); (f) sum of ocean regions (including the *Takahashi et al.* [2002] fluxes that were presubtracted for the inversion).
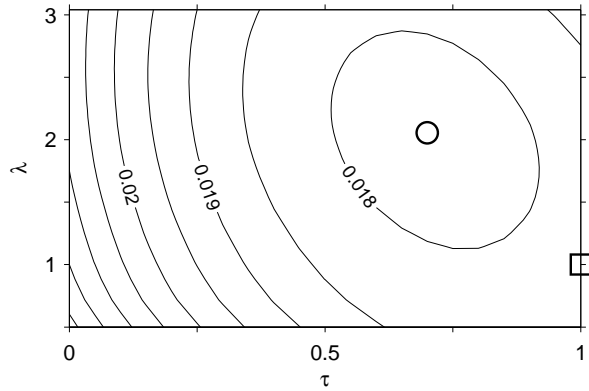
Figure 2.2. Generalized cross-validation (GCV) function for the TransCom inversion. The circle marks the function minimum. The square marks the original TransCom parameter values.

Appendix: Linear Inversion Methods and Generalized Cross-Validation

Here we briefly review regularization methods for the solution of linear ill-posed problems, point out relationships among different regularization methods that are used in inversions for regional carbon fluxes, and show how generalized cross-validation can be used with different regularization methods. The mathematical developments largely follow *Hansen* [1998].

1. The inverse problem for regional carbon fluxes

To estimate CO_2 fluxes, one has to estimate a vector $\mathbf{x}$ in the linear model

$$\mathbf{Ax} = \mathbf{b} + \boldsymbol{\varepsilon}, \tag{1}$$

where $\mathbf{b}$ is a given $n \times 1$ vector of CO_2 concentrations at n locations; $\boldsymbol{\varepsilon}$ is a random error with zero mean and with covariance matrix $\mathrm{cov}(\boldsymbol{\varepsilon}) = \mathbf{C}_b$; $\mathbf{x}$ is an unknown $p \times 1$ vector of CO_2 fluxes into and out of p regions; and $\mathbf{A}$ is a given $n \times p$ matrix representing a transport operator that relates CO_2 fluxes to CO_2 concentrations [e.g., *Enting*, 2002].

If the transport operator $\mathbf{A}$ is ill-conditioned, as is generally the case when the transport is turbulent so that the effect of regional sources and sinks on CO_2 concentrations downstream is smoothed out, the least squares estimate of the CO_2 fluxes is poorly constrained by the CO_2 concentrations. In inversions for regional CO_2 fluxes, more stable flux estimates are usually obtained by minimizing, in place of the least squares object function, a regularized object function

$$J = (\mathbf{Ax} - \mathbf{b})^T \mathbf{C}_b^{-1}(\mathbf{Ax} - \mathbf{b}) + \lambda^2(\mathbf{x} - \mathbf{x}_0)^T \mathbf{C}_x^{-1}(\mathbf{x} - \mathbf{x}_0), \tag{2}$$

consisting of the sum of the least squares object function (first term) and a penalty term (second term) that penalizes deviations of the solution $\mathbf{x}$ from a given prior estimate $\mathbf{x}_0$. The covariance matrix $\mathbf{C}_x$ represents uncertainty about the prior estimate $\mathbf{x}_0$. The regularization parameter λ indicates the relative weight of the penalty term compared with the least squares term.

In CO_2 inversions, the covariance matrices $\mathbf{C}_b$ and $\mathbf{C}_x$ are usually taken to be diagonal, with diagonal

entries $\mathbf{c}_b$ and $\mathbf{c}_x$ equal to assumed variances of the local CO_2 concentration errors and of the regional prior flux distributions. (However, the methods presented here may be used regardless of whether the covariance matrices are diagonal.) The regularization parameter λ is usually taken to be equal to one. In the TransCom protocol, which we followed, the prior standard deviations $\mathbf{c}_x^{1/2}$ for land regions are taken to be proportional to the growing season net CO_2 fluxes estimated with a model of the biosphere; the prior standard deviations $\mathbf{c}_x^{1/2}$ for ocean regions are taken to be proportional to the area of each region and to the number of CO_2 measurements in each region [*Gurney et al.*, 2003].

The minimizer $\mathbf{x}^*$ of the object function (2) for $\lambda = 1$ can be interpreted as a Bayesian maximum a posteriori estimate of CO_2 fluxes, assuming a Gaussian distribution of prior fluxes with mean $\mathbf{x}_0$ and covariance matrix $\mathbf{C}_x$ [*Tarantola*, 1987; *Enting*, 2002]. Alternatively, the minimizer $\mathbf{x}^*$ of the object function (2) for any λ can be interpreted as a Tikhonov-regularized estimate of CO_2 fluxes [*Tikhonov*, 1963; *Hansen*, 1998, chapter 5]. (Tikhonov regularization is also known as ridge regression [*Hoerl and Kennard*, 1970].) In the Bayesian interpretation, the weighting matrix, or inverse of the prior covariance matrix, $\mathbf{C}_x^{-1}$ is taken to be known a priori. In the regularization interpretation, the weighting matrix $\mathbf{C}_x^{-1}$ is taken to be known up to the scaling factor λ, a regularization parameter that must be estimated.

2. Transformation to standard form

The object function (2) can be transformed to a standard form by mapping the prior estimate $\mathbf{x}_0$ to zero and by rescaling variables so that the covariance matrices $\mathbf{C}_b$ and $\mathbf{C}_x$, assumed to be nonsingular, are identity matrices [*Hansen*, 1998, chapter 2.3]. The transformation takes the form

$$\bar{\mathbf{A}} = \mathbf{C}_b^{-1/2} \mathbf{A} \mathbf{C}_x^{1/2}, \tag{3a}$$

$$\bar{\mathbf{x}} = \mathbf{C}_x^{-1/2}(\mathbf{x} - \mathbf{x}_0), \tag{3b}$$

$$\bar{\mathbf{b}} = \mathbf{C}_b^{-1/2}(\mathbf{b} - \mathbf{A}\mathbf{x}_0), \tag{3c}$$

where $\mathbf{C}_b^{1/2}$ and $\mathbf{C}_x^{1/2}$ are the Cholesky factors of the covariance matrices $\mathbf{C}_b$ and $\mathbf{C}_x$. The linear model (1) in the original variables is equivalent to the linear model

$$\bar{\mathbf{A}}\bar{\mathbf{x}} = \bar{\mathbf{b}} + \bar{\varepsilon} \tag{4}$$

in the transformed variables, with an error covariance matrix $\mathrm{cov}(\bar{\varepsilon})$ equal to the identity matrix. In the transformed variables (3), the object function (2) assumes the standard form

$$J = \|\bar{\mathbf{A}}\bar{\mathbf{x}} - \bar{\mathbf{b}}\|_2^2 + \lambda^2\|\bar{\mathbf{x}}\|_2^2, \tag{5}$$

where $\| \cdot \|_2$ denotes the Euclidean norm. For $\lambda = 0$, minimizing the object function (5) yields the least squares estimates. For $\lambda = 1$, minimizing the object function (5) yields the Bayesian estimates used in the TransCom CO_2 inversions [*Gurney et al.*, 2003] as well as in most other CO_2 inversions starting with *Enting* [1993]. For arbitrary $\lambda > 0$, minimizing the object function (5) yields the Tikhonov-regularized estimate with regularization parameter λ.

3. Singular value decomposition, filter factors, and regularization methods

The least squares estimate and several regularized estimates for the linear model (4) can be expressed compactly in terms of the singular value decomposition of the transformed transport operator $\bar{\mathbf{A}}$,

$$\bar{\mathbf{A}} = \mathbf{U}\boldsymbol{\Sigma}\mathbf{V}^T, \tag{6}$$

where $\mathbf{U}$ and $\mathbf{V}$ have orthonormal columns $\mathbf{u}_i$ (left singular vectors) and $\mathbf{v}_i$ (right singular vectors), and $\boldsymbol{\Sigma}$ is a diagonal matrix with diagonal entries $\sigma_i \geq 0$, which are assumed to be arranged in descending order. A large family of estimates $\bar{\mathbf{x}}^*$ for the linear model (4) can be expressed as a linear combination of right singular vectors $\mathbf{v}_i$,

$$\bar{\mathbf{x}}^* = \sum_{i=1}^{\mathrm{rank}(\bar{\mathbf{A}})} f_i \frac{\mathbf{u}_i^T\bar{\mathbf{b}}}{\sigma_i}\mathbf{v}_i, \tag{7}$$

where the filter factors f_i characterize the estimation method [cf. *Hansen*, 1998, chapter 4]. The coefficients $\mathbf{u}_i^T\bar{\mathbf{b}}$ are often referred to as Fourier coefficients, in analogy to inverse problems in which the counterpart of the matrix $\bar{\mathbf{A}}$ is a convolution operator whose singular value decomposition is equivalent to a Fourier expansion [cf. *Wahba*, 1977; *Anderssen and Prenter*, 1981].

a. Least squares estimation

For the least squares estimate ($\lambda = 0$), the filter factors are identically equal to one (that is, no filtering),

$$f_i = 1 \quad \text{for all} \quad i. \tag{8}$$

Expressing the least squares estimate in terms of the singular value decomposition (7) makes manifest that errors of order ε in the transformed data $\bar{\mathbf{b}}$ typically result in errors of order $\varepsilon/\sigma_{\min}$ in the estimate $\bar{\mathbf{x}}^*$, where $\sigma_{\min}$ is the smallest nonzero singular value. If typical data errors exceed the smallest singular value, the least squares estimate is poorly constrained by the data. If the transformed transport operator $\bar{\mathbf{A}}$ is rank-deficient (i.e., $\mathrm{rank}(\bar{\mathbf{A}}) < p$), the least squares estimate is not unique. In this case, the estimate (7) with filter factors (8) is the least squares estimate with minimum norm $\|\bar{\mathbf{x}}^*\|_2$.

If the transformed transport operator $\bar{\mathbf{A}}$ has small singular values, regularization methods stabilize the least squares estimates by filtering out the contributions of right singular vectors $\mathbf{v}_i$ that are associated with the small singular values σ_i. These contributions to the estimate (7) typically represent high-frequency noise that is not estimable given the uncertainty of the data.

b. Bayesian estimation

For the Bayesian maximum a posteriori estimate ($\lambda = 1$), for which a prior normal distribution with mean zero and identity covariance matrix is assumed for the transformed fluxes $\bar{\mathbf{x}}$, the filter factors are

$$f_i = \frac{\sigma_i^2}{\sigma_i^2 + 1}. \tag{9}$$

This filter function decays smoothly from $f_i \approx 1$ for $\sigma_i \gg 1$ to $f_i \approx 0$ for $\sigma_i \ll 1$; that is, right singular vectors with singular values smaller than 1 are effectively filtered out. This filtering is what is commonly used in inversions for CO_2 fluxes.

c. Tikhonov regularization/ridge regression

For the Tikhonov-regularized estimate (λ adjustable), the filter factors are [*Hansen*, 1998, chapter 4.2]

$$f_i = \frac{\sigma_i^2}{\sigma_i^2 + \lambda^2}. \tag{10}$$

This filter function decays smoothly from $f_i \approx 1$ for $\sigma_i \gg \lambda$ to $f_i \approx 0$ for $\sigma_i \ll \lambda$; that is, right singular vectors with singular values smaller than λ are effectively filtered out.

The Tikhonov filter function is structurally identical to the Wiener filter, which is the optimal filter to separate noise of spectral density λ^2 from a signal of spectral density σ_i^2 [*Papoulis*, 1991; *Anderssen and Prenter*, 1981].

d.   Least squares estimation with inequality constraints

The estimate (7) with Tikhonov filter factors (10) is also the solution of a least squares problem with inequality constraint,

$$\min_{\bar{\mathbf{x}}} \|\bar{\mathbf{A}}\bar{\mathbf{x}} - \bar{\mathbf{b}}\|_2^2 \quad \text{subject to} \quad \|\bar{\mathbf{x}}\|_2^2 \leq \alpha, \tag{11}$$

where α is a parameter constraining the norm of the solution. If the norm $\|\bar{\mathbf{x}}^*\|_2$ of the least squares estimate is less than α, the least squares estimate solves the constrained least squares problem (11). If the norm of the least squares estimate is greater than α, the Tikhonov estimate solves the constrained least squares problem (11), with a regularization parameter λ (a Lagrange multiplier) that is a function of α [*Golub and Van Loan*, 1989, chapter 12.1.2].

Regularization with an inequality constraint (11), then, is equivalent to Tikhonov regularization if the inequality constraint is not redundant. Bayesian estimation and regularization with an inequality constraint, contrasted by *Fan et al.* [1999] as different methods, are therefore very similar. The methods merely correspond to choosing different values of the regularization parameter λ (and potentially different scalings of the variables).

e.   Regularization by truncated singular value decomposition

Another common way to filter out right singular vectors that are associated with small singular values is to keep only the first k right singular vectors, corresponding to filtering with a step function filter

$$f_i = \begin{cases} 1 & i \leq k \\ 0 & i > k \end{cases} \tag{12}$$

for some effective rank $k \leq \text{rank}(\bar{\mathbf{A}})$ [e.g., *Hansen*, 1998, chapter 3.2; *Fan et al.*, 1999]. This usually yields estimates similar to Tikhonov regularization with regularization parameter $\lambda \approx \sigma_k$.

4.   Generalized cross-validation

Generalized cross-validation offers a way to estimate appropriate values of parameters such as the regularization parameters k in truncated singular value decomposition, λ in Tikhonov regularization, or α in least squares estimation with inequality constraint. In the Bayesian formulation used in TransCom, components of the covariance matrices $\mathbf{C}_b$ and $\mathbf{C}_x$, which are generally poorly known, can likewise be estimated by generalized cross-validation.

For the family of estimates (7), the generalized cross-validation function, to be minimized as a function of the parameters, is given by

$$\text{GCV} = \frac{\|\bar{\mathbf{A}}\bar{\mathbf{x}}^* - \bar{\mathbf{b}}\|_2^2}{\mathcal{T}^2}, \tag{13}$$

where the numerator is the squared residual norm and the denominator is a squared effective number of degrees of freedom [*Hansen*, 1998, chapter 7.4]. For all estimation methods discussed above, the effective number of degrees of freedom (which is not necessarily an integer) can be written in terms of the filter factors as

$$\mathcal{T} = n - \sum_{i=1}^{\text{rank}(\bar{\mathbf{A}})} f_i. \tag{14}$$

The residual norm in the numerator of the GCV function can be computed efficiently from a singular value decomposition of the transformed transport operator $\bar{\mathbf{A}}$, making the evaluation of the GCV function for several regularization parameters straightforward.

The minimizer of the GCV function approximately minimizes the expected mean squared error of predictions of the transformed data $\bar{\mathbf{b}}$ with an estimated linear model (4) [*Golub et al.*, 1979]. With small but nonzero probability, the GCV function has a minimum near zero regularization (i.e., at $\lambda = 0$ or for $\alpha \to \infty$), so that generalized cross-validation occasionally leads to undersmoothed estimates when, in fact, more strongly regularized and smoother estimates would be more appropriate [*Wahba and Wang*, 1995]. Undersmoothed estimates in such cases can be avoided by constructing bounds for the regularization parameters, for example, from a priori guesses of the magnitude of the residuals [*Hansen*, 1998, chapters 7.7 and 7.2].

In our analyses, we evaluated the GCV function (13) as a function of the regularization parameter λ and of the weighting parameter τ on a mesh with spacing of 0.05 in τ and of 0.27 in λ^2.

Where inversion results are sensitively dependent on inversion parameters, it may be useful not only to choose "optimal" values of the parameters but also to estimate confidence regions for the parameters. Methods that treat inversion parameters as random variables and estimate their probability distributions given the data and a probability model for the parameters [*Wang and Wahba*, 1995; *Koch*, 1999; *Koch and Kusche*, 2002] could be applied for this purpose. Heuristic estimates of confidence regions may also be obtained from the curvature of the GCV function or other object functions at the optimum, by analogy with ordinary least squares regression [*Press et al.*, 1992, chapter 15.6]. Given confidence regions, the impact the uncertainty about inversion parameters has on flux estimates could then be quantified using either linear error propagation or Monte-Carlo methods.

References

Anderssen, R. S., and P. M. Prenter (1981), A formal comparison of methods proposed for the numerical solution of first kind integral equations, *J. Austral. Math. Soc. B*, *22*, 488–500.

Enting, I. G. (2002), *Inverse Problems in Atmospheric Constituent Transport*, 392 pp., Cambridge University Press, Cambridge and New York.

Enting, I. G. (1993), Inverse problems in atmospheric constituent studies. 3. Estimating errors in surface sources, *Inverse Problems*, *9*, 649–665.

Fan, S. M., J. L. Sarmiento, M. Gloor, and S. W. Pacala (1999), On the use of regularization techniques in the inverse modeling of atmospheric carbon dioxide, *J. Geophys. Res.*, *104*(D17), 21503–21512.

Golub, G. H., and C. F. Van Loan (1989), *Matrix Computations*, 2nd ed., 642 pp., Johns Hopkins University Press, Baltimore and London.

Golub, G. H., M. Heath, and G. Wahba (1979), Generalized cross-validation as a method for choosing a good ridge parameter, *Technometrics*, *21*, 215–223.

Gurney, K. R., R. M. Law, A. S. Denning, P. J. Rayner, D. Baker, P. Bousquet, L. Bruhwiler, Y. H. Chen, P. Ciais, S. M. Fan, I. Y. Fung, M. Gloor, M. Heimann, K. Higuchi, J. John, E. Kowalczyk, T. Maki, S. Maksyutov, P. Peylin, M. Prather, B. C. Pak, J. Sarmiento, S. Taguchi, T. Takahashi, and C. W. Yuen (2003), TransCom 3 CO_2 inversion intercomparison: 1. Annual mean control results and sensitivity to transport and prior flux information, *Tellus*, *55*(B2), 555–579.

Hansen, P. C. (1998), *Rank-Deficient and Discrete Ill-Posed Problems: Numerical Aspects of Linear Inversion*, 247 pp., Society for Industrial and Applied Mathematics, Philadelphia.

Hoerl, A. E., and R. W. Kennard (1970), Ridge regression: Biased estimation for non-orthogonal problems, *Technometrics*, *12*, 55–67.

Koch, K.-R. (1999), *Parameter Estimation and Hypothesis Testing in Linear Models*, Springer, Berlin, New York.

Koch, K.-R. and J. Kusche (2002), Regularization of geopotential determination from satellite data by variance components, *J. Geodesy*, 76(5), 259-268.

Papoulis, A. (1991), *Probability, Random Variables, and Stochastic Processes*, 3rd ed., 666 pp., McGraw Hill, New York.

Press, W. H., S. A. Teukolsky, W. T. Vetterling and B. P. Flannery (1992), *Numerical Recipes in C: The Art of Scientific Computing*, 994 pp., Cambridge University Press, Cambridge, New York.

Tarantola, A. (1987), *Inverse Problem Theory: Methods for Data Fitting and Model Parameter Estimation*, 613 pp., Elsevier, New York.

Tikhonov, A. N. (1963), Solution of incorrectly formulated problems and the regularization method, *Soviet Math. Dokl.*, *4*, 1035–1038. English transl. of *Doklady Akademii Nauk SSSR*, *151*, 501–504.

Wahba, G. (1977), Practical approximate solutions to linear operator equations when the data are noisy, *SIAM J. Numer. Anal.*, *14*, 651–667.

Wahba, G., and Y. Wang (1995), Behavior near zero of the distribution of GCV smoothing parameter estimates, *Stat. Probabil. Lett.*, *25*, 105–111.

Wang, Y. D., and G. Wahba (1995), Bootstrap confidence-intervals for smoothing splines and their comparison to Bayesian confidence-intervals, *J. Stat. Comput. Simul.*, 51(2-4), 263–279.

Chapter 3: Mean Regional Air-Sea Gas Transfer Velocities

Estimated from Ocean and Atmosphere Carbon Isotope

Measurements

3.1 Abstract

The air-sea gas transfer velocity is an important determinant of the exchange of gases, including CO_2, between the atmosphere and ocean, but the magnitude of the transfer velocity and what factors control it remains poorly known. Here, we use oceanic and atmospheric observations of ^{14}C and ^{13}C to constrain the global mean gas transfer velocity as well as the exponent of its wind-speed dependence, utilizing the distinct signatures left by the air-sea exchange of $^{14}CO_2$ and $^{13}CO_2$. While the atmosphere and ocean inventories of $^{14}CO_2$ and $^{13}CO_2$ constrain the mean gas transfer velocity, the latitudinal pattern in the atmospheric and oceanic ^{14}C and ^{13}C distributions contains information about the wind speed dependence. We computed the uptake of bomb ^{14}C by the ocean for different transfer velocity patterns using pulse response functions from an ocean general circulation model, and evaluated the match between the predicted bomb ^{14}C concentrations and observationally based estimates for the 1970s-1990s. Using a windspeed climatology based on satellite measurements, we solved either for the mean gas transfer velocity over each of 11 ocean regions or for the best-fit global relationship between gas exchange and mean windspeed. We also compared the predicted consequences of different gas exchange relationships on the rate of change and interhemisphere gradient of ^{14}C in atmospheric CO_2 with tree-ring and atmospheric measurements. Our results suggest that globally, the dependence of the air-sea gas transfer velocity on windspeed is close to linear, with an exponent of 0.9 ± 0.4, and that the global mean gas transfer velocity at a Schmidt number of 660 is 21 ± 2 cm / hour, similar to the results of previous analyses. We find that the air-sea flux of ^{13}C estimated

from atmosphere and ocean observations also suggests a lower than quadratic global

dependence of gas exchange on windspeed.

3.2 Introduction

In recent decades, the ocean has absorbed roughly one third of the CO_2 released

into the atmosphere by fossil fuel burning [*Prentice et al.*, 2001; *Sabine et al.*, 2004].

Ocean CO_2 uptake thus significantly influences the course of greenhouse climate forcing.

Further, the added CO_2 makes the ocean more acidic, with potentially serious

consequences for ocean ecology [*Caldeira and Wickett*, 2003; *Feely et al.*, 2004a; *Orr et

al.*, 2005]. As a result, quantitative description of the air-sea CO_2 flux and of changes in

ocean carbon chemistry has become a leading goal of oceanographic research [e.g.

Fasham, 2003].

The air-sea flux of CO_2 and other gases is generally estimated using a bulk

parameterization approach, i.e., assumed to be proportional to the difference in the

concentration of a gas between the bulk ocean and the bulk atmosphere [e.g. *Liss and

Merlivat*, 1986; *Frost and Upstill-Goddard*, 1999; *Orr et al.*, 2001]. This implies a

relationship of the form

$$F = k_w \cdot (C_s - C_a), \tag{1}$$

where F is the gas flux out of the ocean (with units such as mol m^{-2} s^{-1}); C_s is the gas

concentration in surface water (mol m^{-3}); C_a is the surface ocean concentration of the gas

in equilibrium with the partial pressure p (atm) of the gas in the air over the ocean surface

computed from Henry's law, i.e. $C_a = \alpha \cdot p$, with α (mol m^{-3} atm^{-1}) being the gas solubility; and k_w is an air-sea gas transfer velocity (m s^{-1}) that is independent of the gas concentration but might depend on, for example, the gas diffusivity and sea surface state. In this bulk parameterization, a negative concentration gradient $C_s - C_a$ across the air-sea interface is the driving force for gas uptake by the ocean, but the instantaneous uptake rate then depends on the gas transfer velocity k_w.

Knowledge of the gas transfer velocity is vital to approaches that estimate contemporary ocean CO_2 uptake from observations of the air-sea pCO_2 disequilibrium [*Takahashi et al.*, 2002] as any bias or uncertainty in the gas transfer velocity leads to a corresponding bias or uncertainty in the flux estimate. The gas transfer velocity is also a very important input parameter for the estimation of the oceanic uptake of anthropogenic CO_2 using an isotopic budget of ^{13}C in the atmosphere and ocean [*Tans et al.*, 1993; *Gruber and Keeling*, 2001; *Quay et al.*, 2003]. Knowledge of the gas transfer velocity is of secondary importance for modeling the air-sea exchange of CO_2, except at regions where vertical mixing is rapid, such as the equator and at high latitudes, where surface water turns over too quickly to reach equilibrium with atmospheric gas pressures [*England et al.*, 1994; *Murnane et al.*, 1999; *Ito et al.*, 2004]. Accurate determination of the gas transfer velocity would also help in inferring the air-sea fluxes of a variety of other gases of biogeochemical interest, such as oxygen, nitrous oxide, and dimethyl sulfide, from measurements of the concentration gradient across the air-sea interface [e.g. *Liss et al.*, 2004].

Gas transfer velocities over periods of up to a few days have been measured in laboratory wind tunnels as well as in small lakes and in the ocean [overviews in *Jähne*

and Haussecker, 1998; *Frost and Upstill-Goddard*, 1999]. Methods used include eddy correlation for fluxes of gases such as CO_2 [*McGillis et al.*, 2001], and observing the evasion of purposefully released tracer gases such as SF_6 and helium-3 [*Nightingale et al.*, 2000]. Gas transfer velocities are found to depend on boundary layer turbulence and to be enhanced by the formation of bubbles from breaking waves [see *Asher et al.*, 1998], and in many cases can be related to prevailing windspeed.

Drawing on such findings, *Wanninkhof* [1992] proposed a formulation for the air-sea gas transfer velocity that depends quadratically on windspeed,

$$k_w = k_0 \cdot u^2 \cdot (Sc/660)^{-0.5}, \qquad (2)$$

where k_0 is a constant, u is the windspeed measured at 10-meter height (m s^{-1}), and Sc is the Schmidt number (water kinematic viscosity divided by the gas diffusivity). 660 is a scaling factor included for convenience because it is a typical value for the Schmidt number of CO_2 in the ocean. The exponent -0.5 is representative of the diffusivity dependence found in various laboratory dual-tracer experiments, and more recently also in the open ocean [*Nightingale et al.*, 2000]. *Wanninkhof* [1992] calibrated the constant k_0 such that the global mean gas transfer velocity is consistent with the mean gas transfer velocity estimated from natural [*Broecker and Peng*, 1982] and bomb ^{14}C [*Broecker et al.*, 1986] (see more below).

The *Wanninkhof* [1992] formulation has been widely adopted for estimating ocean uptake of CO_2 and other gases from an observed or modeled air-sea concentration difference [e.g. *England et al.*, 1994; *Orr et al.*, 2001; *Dutay et al.*, 2002; *Takahashi et*

al., 2002]. Earlier, a linear, or piecewise linear, dependence on windspeed was more commonly assumed [*Broecker et al.*, 1985; *Liss and Merlivat*, 1986; *Toggweiler et al.*, 1989; *Tans et al.*, 1990]. *Wanninkhof and McGillis* [1999] more recently suggested that gas exchange may scale with the cube, rather than the square, of windspeed.

Comparing the commonly used relationships between air-sea gas exchange and windspeed proposed by *Wanninkhof* [1992], *Wanninkhof and McGillis* [1999] and others such as *Liss and Merlivat* [1986] and *Nightingale et al.* [2000] reveals a range of at least a factor of 2 at any given windspeed. This leads directly to a factor of 2 difference in the air-sea flux when estimated from air-sea partial pressure difference. The different relationships also lead to rather different diagnosed latitudinal pattern of air-sea fluxes in contemporary CO_2 because of the large mean differences in windspeed (Figure 1.1). If the gas transfer velocity increases as a quadratic or cubic power of windspeed even under high winds, much of the total ocean CO_2 uptake may be occurring during sporadic intense storms, such as hurricanes, and interannual variability in storm frequencies could explain much of the observed interannual variability in the rate of increase of atmospheric CO_2 [*Bates*, 2002], although inferences from atmospheric O_2 and $\delta^{13}CO_2$ do not support assigning such great interannual variability to the ocean CO_2 sink [*Bousquet et al.*, 2000]. Formulations of the air-sea gas transfer velocity thus need further evaluation.

In this study, we explore how observations of ^{14}C and ^{13}C in the atmosphere and ocean can help to constrain the mean gas exchange velocity as well as the exponent n of the windspeed dependency. Some of the ^{14}C constraints are well known and have been used previously, but we also introduce a set of new constraints, such as the

interhemisphere gradient in the atmospheric ^{14}C content and the rate of decrease in atmospheric ^{14}C. We further consider how the measurements of ^{13}C and its air-sea isotope flux can be used to address this question, supplementing the ^{14}C constraints. The next section introduces these constraints and how they have been used in the past.

3.3 Carbon isotope constraints on the gas transfer velocity

Observations of carbon-14 (radiocarbon) concentrations in the atmosphere and ocean have played a very important role in constraining the gas transfer velocity. ^{14}C is an unstable isotope with a half-life of 5730 years which comprises about one part in 10^{12} of the carbon in earth's atmosphere. ^{14}C is produced in the upper atmosphere at a roughly steady rate in reactions with cosmic rays and solar protons [e.g. *Lingenfelter*, 1963]. From there, it is transported as $^{14}CO_2$ into the lower atmosphere and then taken up by the ocean and terrestrial biosphere. Because water from the deep ocean takes on the order of 1000 years to circulate to the surface, dissolved inorganic carbon (DIC) in the deep ocean typically has a $^{14}C/^{12}C$ ratio about 200‰ lower than the atmospheric concentration [e.g. *Nydal*, 2000]. Surface ocean DIC reflects exchange both with the deep ocean and with the atmosphere, and so has an intermediate ratio.

The uptake of $^{14}CO_2$ by the ocean is relatively slow. A mixed layer of 50 m depth takes roughly 10 years for its DIC ^{14}C content to reach equilibrium with a perturbation in the $^{14}CO_2$ content of the overlying air [*Broecker and Peng*, 1982]. This equilibration time-scale is longer than the typical residence time of water in the surface mixed layer, leading to the observation that the surface ocean ^{14}C content of DIC can be far from equilibrium with the atmosphere (large concentration gradients across the air-sea

interface). This contrasts strongly with the exchange of other gases, including oxygen and chlorofluorocarbons, whose exchange time-scale is of the order of a week, resulting in surface ocean concentrations usually being very close to their equilibrium concentration.

^{14}C isotopic abundance is expressed in delta notation, where $\Delta^{14}C$ is the ratio of the measured $^{14}C/^{12}C$ ratio (normalized for mass-dependent isotopic fractionation to a reference $^{13}C/^{12}C$ level) to that of atmospheric CO_2 in the 19th century (determined from tree ring cellulose carbon), minus one [*Stuiver and Polach*, 1977]. Tree ring records show that $\Delta^{14}C$ of atmospheric CO_2 (or "atmospheric $\Delta^{14}C$") remained close to 0‰ in the centuries prior to the 20th century, suggesting that the global carbon cycle remained in an approximate steady-state [*Stuiver and Becker*, 1993], while measurements of coral carbonate show that surface water DIC averaged around −50‰ [*Druffel and Suess*, 1983]. In the first half of the 20th century, atmospheric $\Delta^{14}C$ dropped by around 20‰ because of dilution of ^{14}C by CO_2 derived from fossil fuels, which contain no ^{14}C [*Suess*, 1955; *Tans et al.*, 1979; *Stuiver and Quay*, 1981].

Nuclear bomb tests in the 1950s and early 1960s produced large amount of ^{14}C ("bomb radiocarbon") in the upper atmosphere, so that $\Delta^{14}C$ of CO_2 in the lower troposphere rose to +800‰ by 1964, only to decline in the following decades (to around +65‰ in 2004) as a result of exchange of atmospheric carbon with biosphere and ocean reservoirs that had lower $\Delta^{14}C$ (Figure 3.2a). The bomb radiocarbon influx from the atmosphere into the surface ocean increased the $\Delta^{14}C$ of surface water DIC as much as 300‰ by 1970 [*Linick*, 1980] (Figure 3.2b), at a rate set by air-sea gas exchange, and this bomb radiocarbon is now spreading into deeper water [e.g. *Broecker et al.*, 1985; *Masiello et al.*, 1998]. Due to the long equilibration time-scale of $^{14}CO_2$ across the air-sea

interface, ocean bomb $^{14}CO_2$ uptake is strongly limited by air-sea exchange, making the

bomb $^{14}CO_2$ inventory a powerful constraint for the gas transfer velocity.

The first extensive set of measurements of $\Delta^{14}C$ of ocean DIC (or "ocean $\Delta^{14}C$")

was made as part of the Geochemical Ocean Sections (GEOSECS) program. In a series

of oceanographic cruises in 1972-1978, $\Delta^{14}C$ profiles were measured at about 100

locations, clearly showing the enhancement of $\Delta^{14}C$ in surface water due to bomb

radiocarbon as well as elucidating deep water circulation pathways [*Ostlund and Stuiver*,

1980; *Stuiver and Ostlund*, 1980; 1983].

Broecker et al. [1985; 1986; 1995] used the GEOSECS data to estimate the ocean

bomb radiocarbon inventory by latitude band, arriving at $305\pm30 \times 10^{26}$ atoms in the

whole ocean as of the beginning of 1975 ("mid-GEOSECS"). Based on this inventory,

Broecker et al. estimated the global mean CO_2 invasion rate (equivalent to the product

k_wC_a in our notation [Equation 1]) at 20 ± 3 mol m^{-2} year^{-1}, a rate also consistent with pre-

bomb ocean $\Delta^{14}C$ profiles [*Broecker and Peng*, 1982]. *Broecker and Peng* [1982] used

GEOSECS and other ^{14}C data to also look at the natural ^{14}C constraint on the gas transfer

velocity. This constraint arises from the requirement that at steady state, the net invasion

of $^{14}CO_2$ into the ocean must be balanced by the decay of ^{14}C in the ocean. By subtracting

the estimated bomb ^{14}C from the observed ^{14}C, *Broecker and Peng* [1982] obtained an

estimate of the total ^{14}C that existed in the ocean in preindustrial times and an estimate of

the preindustrial air-sea difference in $\Delta^{14}CO_2$, from which they derived an estimate of the

gas transfer velocity. The estimate *Broecker and Peng* [1982] obtained following this

approach was remarkably close to that obtained from the bomb ^{14}C constraint. These ^{14}C-

based mean values have since then been widely used [e.g., *Tans et al.*, 1990;

Wanninkhof, 1992; *Wanninkhof and McGillis*, 1999] to set the scaling factor k_0 in expressions for k_w as a function of windspeed (such as Equation 2).

Hesshaimer et al. [1994] attempted to deduce from stratospheric $\Delta^{14}C$ measurements the total amount of bomb radiocarbon produced and to derive a consistent budget for its spread. They found that atmospheric $\Delta^{14}C$ had been declining more slowly than would be expected given the GEOSECS-derived rate of ocean uptake and assumptions about biosphere carbon uptake. They therefore proposed that mid-1970s ocean bomb radiocarbon uptake had to be ~25% lower, or around 230×10^{26} atoms, and suggested that this implies a lower mean gas transfer velocity.

Peacock [2004] showed that simple extrapolation of the GEOSECS station inventories to the whole ocean likely results in an overestimate of the GEOSECS inventory. She obtained an inventory of $258\pm50 \times 10^{26}$ atoms using multiple linear regression of GEOSECS radiocarbon measurements against well-measured ocean quantities, and some $270\pm25 \times 10^{26}$ atoms for the beginning of 1975 using modeled ocean CFC and anthropogenic CO_2 concentration fields to adjust the *Broecker et al.* [1995] extrapolation from GEOSECS measurements. This adjustment can be expected to affect the implied mean gas transfer velocity.

In the 1980s and especially the 1990s, the World Ocean Circulation Experiment (WOCE) and affiliated oceanographic survey programs measured ocean $\Delta^{14}C$ at many more locations, increasing the number of available data by an order of magnitude [*Key et al.*, 2002]. In this paper, we use both GEOSECS results and these new data together with an ocean circulation model to evaluate the mean air-sea transfer velocity and the form of its dependence on windspeed implied by ocean bomb ^{14}C uptake. We also revisit the

natural ^{14}C constraint developed by *Broecker and Peng* [1982]. In addition, we explore three other ^{14}C constraints, all arising from observations of atmospheric ^{14}C.

The first constraint pertains to the preindustrial interhemispheric gradient of ^{14}C. As a result of the upwelling of very old waters with low Δ^{14}C in the Southern Ocean, the ^{14}C content in the surface waters of the Southern Ocean is the lowest anywhere, leading to the largest air-sea gradient in ^{14}C. Taken together with the high windspeeds prevailing in this region, this means that the Southern Ocean takes up a disproportionately large amount of ^{14}C from the atmosphere. This is believed to be the major reason that atmospheric Δ^{14}C was a few permil lower in the southern than in the northern hemisphere in preindustrial times, as inferred from measurements of tree rings [*Braziunas et al.*, 1995]. This atmospheric gradient is sensitive to latitudinal variation in the air-sea transfer velocity, while the overall rate of preindustrial ocean ^{14}C uptake is sensitive primarily to the global mean transfer velocity [*Broecker and Peng*, 1982].

The second and third additional ^{14}C constraints pertain to the post-bomb period. Since the 1980s, the low-latitude oceans have grown close to isotopic equilibrium with the declining atmospheric Δ^{14}C level [e.g. *Caldeira et al.*, 1998], leaving the Southern Ocean, which still has low surface Δ^{14}C due to extensive mixing with deeper waters, as the major site of the uptake of bomb ^{14}C by the ocean [*Levin et al.*, 1987; *Randerson et al.*, 2002]. Thus, recent measurements of both the rate of decline in atmospheric Δ^{14}C and the atmospheric Δ^{14}C gradient between the tropics and high southern latitudes should be particularly sensitive to the air-sea transfer velocity over the Southern Ocean, providing constraints on the parameters $\bar{k}$ and n.

We also consider whether what is known about the total global air-sea fluxes of carbon-13 can help in inferring the form of the gas transfer velocity, as suggested by *Heimann and Monfray* [1989]. ^{13}C has the same slow exchange time-scale that characterizes ^{14}C. This has resulted in the surface ocean ^{13}C/^{12}C ratio lagging substantially behind the recent decrease in the atmospheric ^{13}C/^{12}C ratio arising from the burning of fossil fuels with a low ^{13}C/^{12}C ratio [e.g., *Bacastow et al.*, 1996]. As a consequence, there is now a large net ^{13}C isotope flux out of the ocean. However, isotopic fractionation associated with photosynthesis leads to a distinct latitudinal pattern in ^{13}C/^{12}C of ocean DIC, so that there is an isotope flux out of the ocean at low latitudes but into the ocean at high latitudes [*Gruber et al.*, 1999]. Thus, given the observed surface ocean ^{13}C/^{12}C ratio of DIC, a stronger increase of the gas transfer velocity with windspeed implies a smaller exchange-weighted ^{13}C isotope flux out of the ocean. This can be compared with the ^{13}C isotope flux required to match observations of the rate of change in the ^{13}C/^{12}C ratio of atmospheric CO_2 and of ocean DIC [*Heimann and Maier-Reimer*, 1996; *Gruber and Keeling*, 2001; *Quay et al.*, 2003]. A second ^{13}C constraint exists in the preindustrial ^{13}C flux, which arises from the input of isotopically light organic carbon by rivers, which is then mostly remineralized in the ocean. This flux has been estimated to be of the order of 0.4 Pg C / year [*Heimann and Maier-Reimer*, 1996; *Aumont et al.*, 2001]. We compare this steady-state preindustrial ^{13}C isotope flux with that calculated from the estimated preindustrial ^{13}C/^{12}C ratio of the atmosphere and of sea-surface DIC; given the strong latitudinal dependence of the air-sea gradient in the ^{13}C/^{12}C ratio, this calculated flux would depend sensitively on the assumed windspeed dependence of the gas transfer velocity.

In combining these multiple carbon-14 and carbon-13 constraints, we first present results for simulations of ocean uptake of bomb ^{14}C using an ocean transport model, which we compare with compiled measurements of bomb ^{14}C in the ocean, and with published estimates, based on these measurements, of the total amount and distribution of bomb ^{14}C in the ocean at the 1970s and 1990s (the time of GEOSECS and WOCE respectively). Using this evidence, we find the range of global mean transfer velocities and power law dependences of the transfer velocity on windspeed that best explain the measured distribution. We then check this proposed relationship of the gas transfer velocity with windspeed against other observations of ^{14}C in the atmosphere and of ^{13}C in the ocean and atmosphere. The comparisons with the observed latitudinal distribution of atmospheric Δ^{14}C require the use of an atmospheric transport model to estimate the atmospheric latitudinal gradients that would result from different possible air-sea flux patterns. Our overall goal is to learn from ocean and atmosphere ^{14}C and ^{13}C observations about the mean gas transfer velocity over timescales of months to decades and its regional variability. This would complement smaller-scale laboratory and field work in suggesting and testing parameterizations for air-sea gas exchange.

3.4 Methods

3.4.1 Ocean circulation models

To efficiently simulate the uptake of bomb ^{14}C for many different scenarios, we employed a substitute model derived from surface pulse response functions (see *Joos* [1996] and *Gloor et al.* [2001] for the concept). We used regional pulse functions derived from the MIT general circulation model (MITgcm) [*Marshall et al.*, 1997] integrated in a

quasi-global (80°S to 80°N) ocean configuration with 1° horizontal grid spacing and with

23 vertical levels. This model was driven by air-sea fluxes of heat, freshwater, and

momentum derived by the consortium for Estimating the Circulation and Climate of the

Ocean (ECCO) for the 1992-2002 period using the "adjoint" method to fit the model to a

wide variety of satellite and *in situ* observations [*Stammer et al.*, 2004]. This ocean model

was used to compute tracer Green's functions for estimating anthropogenic CO_2 uptake,

as described by *Mikaloff Fletcher et al.* [in press]. All configuration details were as in

Stammer et al. [2004], except that (i) the 1992-2002 surface boundary conditions were

repeated in order to cover the 1765-2005 simulation period, (ii) sea surface salinity was

relaxed to a monthly mean climatology from the National Oceanographic Data Center

(NODC) World Ocean Atlas 1998 (WOA98) with a time constant of 30 days, and (iii) sea

surface temperature was relaxed to daily mean 1992-2002 estimates from the National

Centers for Environmental Prediction and the National Center for Atmospheric Research

(NCEP/NCAR) atmospheric reanalysis, also with a time constant of 30 days. This model

configuration has been found to reproduce the CFC distribution measured during the

1990s WOCE cruises better than any of the other ocean models compared in the Ocean

Carbon-Cycle Model Intercomparison Project (OCMIP) Phase 2 study [*Dutay et al.*,

2002; *Mikaloff Fletcher et al.*, in press]. We deconvolved regional pulse response

functions for the MITgcm from the tracer Green's functions computed for the *Mikaloff*

Fletcher et al. [in press] study. Given the known flux boundary conditions, we

transformed these Green's functions to obtain pulse-response functions describing yearly

mean concentration patterns resulting from an instantaneous unit pulse of a tracer into

each of 30 surface basis regions (shown in Figure 3.3a). We then used the pulse response

substitute model to simulate the time-varying bomb radiocarbon distributions resulting from a given gas transfer velocity pattern.

To check for errors in model transport, and to assess the degradation in accuracy caused by using the substitute model instead of the full ocean circulation model, we simulated ocean uptake of the chlorofluorocarbons CFC-11 and CFC-12 with the same substitute model and compared the modeled fields with WOCE ocean observations and with a simulation using the full MITgcm. Our boundary conditions followed the OCMIP protocol for chlorofluorocarbons [*Dutay et al.*, 2002], and we used the standard OCMIP air-sea gas exchange formulation. Our substitute model simulated 1994 CFC-11 inventory was 11% lower than that of the gridded field based on WOCE measurements [*Key et al.*, 2004] – 4.61×10^8 versus 5.16×10^8 mol for the volume covered by the gridded field – and the modeled latitudinal distribution tracked the observed one very well, with the exception of underestimating uptake in the northern subtropics (Figure 3.4). (The estimated uncertainty in the WOCE gridded inventory is 15%, or 0.8×10^8 mol [*Key et al.*, 2004].) The latitudinal distribution was also close to that simulated using the full MITgcm (Figure 3.4), suggesting that simulations using the substitute model preserve the large-scale features simulated using the full transport model. Using the substitute model, the correlation coefficient between individual ocean CFC measurements in the GLODAP database [*Key et al.*, 2004] and the modeled CFC concentration at the same grid box and month was +0.84. (The full model corresponded better with observations, with a correlation coefficient of +0.92; its simulated 1994 CFC-11 inventory was 4.82×10^8 mol.) Results for CFC-12 were similar, with the ocean inventory underestimated by 8% and a measured-modeled correlation coefficient of +0.85 using the pulse functions.

Calculation of the perturbation in sea-surface $\Delta^{14}C$ caused by the pre-bomb decrease in $\Delta^{14}C$ of atmospheric CO_2 attributable to fossil fuel burning, and the perturbation in the sea-surface $^{13}C/^{12}C$ ratio caused by the ongoing decrease in the $^{13}C/^{12}C$ of atmospheric CO_2, also attributable to fossil fuel burning, required longer integration times than those available in our pulse response substitute model. For these calculations, we used an offline version of an ocean general circulation model, with monthly-mean transport fields obtained from a version of the Modular Ocean Model (MOM) [*Pacanowski et al.*, 1993] configured as described by *Primeau* [2005]. This model overpredicted rather than underpredicted the 1990s ocean CFC inventory, due to excessive uptake in the Southern Ocean (Figure 3.4): the modeled 1994 inventory was 5.97×10^8 mol, 16% above the inventory based on WOCE measurements. The modeled-measured correlation coefficient for individual CFC-11 measurements was +0.86. Because the MITgcm latitudinal CFC uptake pattern matched observations more closely overall, we used the MITgcm pulse functions to simulate of ocean bomb ^{14}C uptake.

3.4.2 Atmospheric transport model

To predict the gradients in atmospheric $\Delta^{14}C$ resulting from various air-sea gas exchange patterns combined with other carbon fluxes, we again used regional pulse functions for their computational speed and accuracy. These atmospheric pulse response functions, which compactly represent the effect of the release of a unit amount of inert tracer at the surface in a particular region on the atmospheric concentration pattern of that tracer [e.g. *Randerson et al.*, 2002], were generated using the Model of Atmospheric Transport and Chemistry (MATCH) [*Mahowald et al.*, 1997]. MATCH was run with

approximately 5.5° horizontal resolution and 26 vertical levels, and driven by meteorological fields from the NCAR Community Climate Model Version 3 [*Olsen and Randerson*, 2004]. Our pulse functions corresponded to tracer releases over the 22 TransCom regions [*Gurney et al.*, 2002] over each month of the year, allowing us to accurately represent seasonally varying fluxes. We also constructed pulse functions for northern, southern, and equatorial tracer release in the stratosphere (at the 90 millibar pressure level) and in the upper troposphere (at 200 millibar) to allow us to simulate the effect of cosmogenic ^{14}C production in the upper atmosphere on atmospheric Δ^{14}C gradients.

To estimate the error in modeling atmospheric transport with our pulse functions, we compared the latitudinal Δ^{14}C gradients modeled for several of our flux fields with those predicted by annual-mean regional pulse functions generated from an ensemble of 15 transport models for the TransCom Level 3 experiment [*Gurney et al.*, 2003]. Our model predictions were generally within one standard deviation of the intermodel mean. We used the intermodel standard deviation as an estimate of the error in the predicted gradients induced by our atmospheric transport model.

3.4.3 The assumed functional form of the air-sea gas transfer velocity

We took as our reference the parameterization suggested by *Wanninkhof* [1992], which involves a quadratic dependence on windspeed and was scaled to yield the ^{14}C-derived global mean gas transfer velocity (Equation 2). Following OCMIP Phase 2, we use monthly distributions of root-mean-square windspeed over the ocean derived from Special Sensor Microwave Image (SSM/I) satellite measurements over the period 1988-

1993 [*Boutin and Etcheto*, 1996] (shown in Figure 3.1) as the basis for estimating u^2.

Below, we will generally refer to this distribution of the gas transfer velocity simply as

the *Wanninkhof* [1992] distribution. The global mean gas transfer velocity implied by

this parameterization, averaged over ice-free water, is 20.6 cm / hour (at a Schmidt

number of 660).

To test whether the *Wanninkhof* [1992] formulation is consistent with data on air-

sea carbon isotope exchange, and to determine, if necessary, a more suitable formulation,

we sought to estimate the global mean transfer velocity $\bar{k}$ and the windspeed dependence

exponent n in the relationship

$$k_w = \bar{k} \left(\frac{u^n}{\overline{u^n}} \right) (Sc/660)^{-0.5} \qquad (3)$$

where we used the root-mean-square climatological windspeed used in OCMIP (varying

in space and monthly) as an estimate of u and where $\overline{u^n}$ is the area-weighted global mean

of a power of windspeed (spatially and seasonally constant for a given value of n).

(Dividing by $\overline{u^n}$ holds the area-weighted global mean transfer velocity at $\bar{k}$ regardless of

the value of n chosen.) To estimate the parameters $\bar{k}$ and n, we compared the modeled

isotope distributions calculated using different values of $\bar{k}$ and n in Equation 4 with

available observations and sought values of $\bar{k}$ and n that yielded ocean carbon-14 or

carbon-13 uptake patterns that agreed well with the observations. We considered values

of $\bar{k}$ ranging from 0.5 to 1.5 times the *Wanninkhof* [1992] value, or 10-31 cm / hour, and

values of n ranging from 0 to 3. As detailed in the next sections, we employed several

largely independent approaches, using different sets of observations and different applications of our atmosphere and ocean transport models.

3.4.4 Estimating the gas transfer velocity from ocean bomb ^{14}C

3.4.4.1 Simulating ocean uptake of bomb ^{14}C

Following the simplified formulation of *Toggweiler et al.* [1989], we carried bomb radiocarbon in Δ units, and it entered the surface layer following a version of Equation 1 appropriate for isotope fluxes, namely

$$F = k_w \cdot \alpha \cdot pCO_2 \cdot (\Delta_{sea}^{14}C - \Delta_{air}^{14}C) / DIC, \tag{4}$$

where F is now the air-sea flux in Δ units m s^{-1} (positive when out of the ocean), k_w is the gas transfer velocity for CO_2 in m s^{-1}, α is the solubility of CO_2 in seawater (mol m^{-3} atm^{-1}), pCO_2 is the partial pressure of CO_2 in the air (atm), $\Delta_{sea}^{14}C$ is the bomb carbon-14 content of sea surface DIC in Δ units, $\Delta_{air}^{14}C$ is the carbon-14 content of atmospheric CO_2 in Δ units above the preindustrial level of 0‰, and DIC is the sea surface DIC concentration (mol m^{-3}).

The uptake of bomb ^{14}C by the ocean was then computed by combining the flux boundary condition (Eq. 4) with the substitute model representing the transport of bomb ^{14}C into the ocean interior. Our bomb radiocarbon simulations began in 1956 with an ocean bomb radiocarbon concentration initialized at zero (following the operational definition of bomb radiocarbon used in *Rubin and Key* [2002]) and then stepped forward in time.

Of the terms on the right hand side of Equation 4, we varied k_w as specified below. $\Delta_{sea}^{14}C$ was the model prediction for the end of the previous time step. Values for the other terms were adapted from those used in various OCMIP tracer uptake studies, as follows. α was calculated based on the relationship of *Weiss and Price* [1980] and monthly climatological water surface temperature and salinity from the World Ocean Atlas 2001 [*Boyer et al.*, 2002; *Stephens et al.*, 2002]. pCO_2 was taken from a time series of annual-mean CO_2 mixing ratios based on measurements at Mauna Loa (http://quercus.igpp.ucla.edu/OceanInversion/inputs/atm_co2/splco2_mod.dat) [*Keeling et al.*, 1976] and a monthly climatology of sea-level atmospheric pressure from *Esbensen and Kushnir* [1981]. $\Delta_{air}^{14}C$ was from a compilation of annual mean values for northern, equatorial and southern latitudes (I. Levin, personal communication to J. Orr, http://www.ipsl.jussieu.fr/OCMIP/phase3/simulations/NOCES/boundcond/atmC14/Levin /Jim_data_2004.doc) based on long-term atmospheric measurement series at several sites [e.g. *Rozanski et al.*, 1995; *Levin and Kromer*, 2004]. DIC was based on climatologies produced by the Global Ocean Data Analysis Project (GLODAP) for the 1990s (from extensive oceanographic observations) and preindustrially (by subtracting an estimated anthropogenic component from the observations [*Gruber et al.*, 1996]) [*Key et al.*, 2004]. We interpolated between the preindustrial period and the 1990s by assuming that the amount of anthropogenic DIC in the ocean is everywhere proportional to the atmospheric CO_2 mixing ratio elevation above the preindustrial level at the current time step. The comparatively small share of anthropogenic DIC during the simulation period (generally less than 3% of total DIC, even at the surface) means that any errors induced by this interpolation scheme are small.

We applied Equation 4 to ice-free water. We assumed that no gas exchange occurs across sea ice, defined by a monthly sea ice climatology based on *Walsh* [1978] and *Zwally et al.* [1983].

3.4.4.2 Varying the air-sea gas transfer velocity

We took two different approaches for varying the *Wanninkhof* [1992] gas transfer velocity to fit ocean bomb radiocarbon observations. In the first approach, we solved for the best-fit mean transfer velocity in each of 11 large ocean regions, which were aggregations of the 30 ocean regions for which we had pulse functions and were very similar to the basis regions of the TransCom study [*Gurney et al.*, 2002]. We successively perturbed the transfer velocity for each region from the *Wanninkhof* [1992] global mean by a fractional amount (generally 0.1) to construct a linear operator that represented the effect of varying the mean gas transfer velocity in each region on the amounts of bomb radiocarbon simulated at the measurement locations and months. This linearization made it easier to estimate the regional transfer velocities that minimized the misfit between simulated and observed values (with misfit functions as described below). Since the nonlinearity of the dependence of simulated concentrations and inventories on the air-sea transfer velocity was weak, iterating this linearization about the regional transfer velocities estimated from the previous iteration led to rapid convergence. This approach is conceptually similar to that of *Gloor et al.* [2001; 2003] and *Gruber et al.* [2001], who solved for regional air-sea fluxes of heat, oxygen, or anthropogenic CO_2 that best fit ocean observations. As a final step, we fit a power law to the relationship of the derived

regional gas transfer velocities with regional mean windspeeds to estimate globally

optimal values for $\bar{k}$ and n.

Our second approach similarly fit air-sea exchange parameters to bomb

radiocarbon observations, but instead of deriving the best-fit transfer velocity by region,

we sought to directly estimate the global mean transfer velocity $\bar{k}$ and the windspeed

dependence exponent n that best fit ocean bomb radiocarbon observations. We simulated

ocean bomb radiocarbon uptake for different values of n and $\bar{k}$ on a mesh using a

spacing of 0.3 in n and 0.1 times the *Wanninkhof* [1992] value (or about 2 cm / hour) in

$\bar{k}$. We solved for the best-fit values by linearizing a misfit function, as in the first

approach, about the combination of $\bar{k}$ and n in our mesh that had the smallest misfit.

3.4.4.3 Ocean ^{14}C data

We compared our simulated bomb radiocarbon fields with a quality-controlled

compilation of 17,501 measurements of radiocarbon in ocean water samples prepared by

the Global Ocean Data Analysis Project (GLODAP) [*Key et al.*, 2004], which represent

1,070 depth profiles (Figure 3.3). The compilation includes measurements from

GEOSECS in the 1970s and from several cruises in the 1980s, with a predominance of

measurements from the WOCE program in the 1990s. As part of GLODAP, gridded

maps of ocean total and bomb radiocarbon were also developed based on interpolation

from WOCE-era measurements [*Key et al.*, 2004].

A measurement of an ocean sample taken in the 1970s-1990s reveals only its total

Δ^{14}C. To compare this measurement to a simulated value of bomb Δ^{14}C requires an

estimate of the water's 1950s (pre-bomb) Δ^{14}C, which can be then subtracted to yield the

bomb enhancement. For most of the ocean $\Delta^{14}C$ measurements, GLODAP provides estimates of this background level and of the bomb enhancement component. These are based primarily on the assumption that the water's pre-bomb $\Delta^{14}C$ is linearly related to its potential alkalinity. Water with higher potential alkalinity has generally been in the deep ocean longer, and thus had lost ^{14}C to decay. This relationship was calibrated using 1950s coral and surface water samples, as well as later deep water samples that contain little bomb radiocarbon [*Rubin and Key*, 2002]. The typical error in deducing $\Delta^{14}C$ from potential alkalinity is found to be around 12‰ [*Rubin and Key*, 2002]. This is much worse than the analytical precision of the $\Delta^{14}C$ measurements, typically around 5‰ [*Key et al.*, 2002].

An alternative approach to estimating the $\Delta^{14}C$ background, with roughly the same accuracy, is based on the water silica content: water high in silica tends to have low background $\Delta^{14}C$ [*Broecker et al.*, 1985; *Broecker et al.*, 1995; *Peacock*, 2004]. We calculated bomb radiocarbon values using this method as well, employing silica measurements for the same water samples (also from the GLODAP compilation) and the relationship between silica and background $\Delta^{14}C$ derived by *Peacock* [2004]. As a check on the sensitivity of our fit to the bomb radiocarbon component separation, we used both these silica-based determinations of bomb $\Delta^{14}C$ and the GLODAP ones, which are based primarily on potential alkalinity.

3.4.4.4 Comparing simulation with observations

As a first step to determining which air-sea gas transfer velocity distribution yields the best fit with observed bomb radiocarbon levels, we compared our simulated

global bomb radiocarbon ocean total and its latitudinal distribution for the mid-1970s and mid-1990s (at the middle of the GEOSECS and WOCE periods, respectively) with available observation-based inventories [*Broecker et al.*, 1995; *Key et al.*, 2004; *Peacock*, 2004]. To more rigorously determine the best-fit form of the air-sea gas transfer velocity, we compared bomb radiocarbon levels in individual measurements, or alternatively column inventories (the integrals of bomb radiocarbon depth profiles), with model-predicted levels for the same months and grid cells, using data from either the GEOSECS period (1970s) or the WOCE period (1980s-1990s). Many more measurements are available from the 1990s, but because much more time has passed since the period of fastest ocean bomb radiocarbon uptake (~30 years as opposed to ~10 years in the 1970s), the effect of transport errors on attributing source regions to the observed radiocarbon distribution is likely to be larger. For our first approach (solving for the best-fit mean gas transfer velocity by region), we will show only results obtained using GEOSECS data, since WOCE measurements turned out to be unable to consistently distinguish between uptake in some pairs of adjacent regions.

For a given set of observations, we determined which regional gas transfer velocities, or which global mean and windspeed dependence of the gas transfer velocity, minimized the overall misfit between the observations and model predictions. This problem is one of minimizing some norm of the weighted deviation between two vectors representing observations and predictions respectively, so that the minimum-misfit parameter values can be expressed in the form

$$\mathbf{x}^* = \min_{\mathbf{x}} \| \mathbf{C}^{-1/2}(\mathbf{b} - A(\mathbf{x})) \|^2, \tag{5}$$

where **x** is a vector of the unknown parameters, **b** is a vector of the observations, A(**x**) are the model predictions as a function of the unknown parameters, **C** is a covariance matrix representing error in **b**, and ‖·‖ denotes a norm, in this case of the weighted deviation between predictions and observations. Specifying **C** for a comparison between measurements and an ocean model is challenging [e.g. *Wunsch*, 1996]. Sources of uncertainty for the comparison between observations and simulation include measurement error, error in estimating the bomb enhancement from the measured total $\Delta^{14}C$, interannual and small-scale variability in ocean transport not included in the model [*Peacock et al.*, 2005], and any number of spatially variable shortcomings in model transport. Here, we assumed that the error covariance matrix **C** is diagonal, although in fact the transport and bomb component attribution errors appear to show spatial autocorrelation, with the errors associated with observations that are close in space and time tending to be similar [cf. *Michalak et al.*, 2004 in an atmospheric inversion context]. For comparing individual measurements or column inventories, we assumed the error of each measurement or column inventory to be the same, meaning that all observations or column inventories were weighted equally.

In standard least-squares minimization, the vector 2-norm of the misfit is minimized in Equation 5; this minimum is easy to compute and is theoretically the maximum-likelihood estimate if the errors have a Gaussian distribution with the assumed covariance matrix **C**. In our comparisons we found that there are often more extreme values in the modeled-measured residual than in a Gaussian distribution, as occasional unusually large modeled-measured misfits result from, for example, a bomb radiocarbon measurement made below the thermocline at a depth that in the model was above the

thermocline and hence had a much higher predicted bomb radiocarbon content. Minimizing a 2-norm would lead to these outlying measurements unduly influencing the best-fit parameter values, so we have preferred to calculate minimum misfits using the 1-norm (the sum of the residual's absolute values), which should be more reliable in the presence of outliers [e.g. *Aster et al.*, 2005, Section 2.4]. We estimated 1 standard deviation uncertainty ranges for the 1-norm minimum from the curvature of the misfit function near its minimum using the results of *Parker and McNutt* [1980] and approximating the misfit function as parabolic.

3.4.5 Atmospheric evidence for 1990s ocean ^{14}C uptake

For the WOCE period (centered around 1994), extensive ocean Δ^{14}C surface measurements were used by *Key et al.* [2004] to construct a sea-surface Δ^{14}C climatology. We used this climatology, along with Equation 4, to compute the expected latitudinal gradient in Δ^{14}C of atmospheric CO_2 for different windspeed dependences of air-sea gas exchange, without reference to an ocean circulation model. To do this, we had to account for other substantial contributors to the latitudinal gradient. We assumed that long-term cosmogenic production averages 6.2 kg ^{14}C / year, balancing decay in short-term carbon pools [*Goslar*, 2001] and consistent with observed ^{14}CO concentrations [*Quay et al.*, 2000], and that interannual variability in production is proportional to the sunspot number [*Lingenfelter*, 1963]. Carbon from fossil fuels contains no ^{14}C, and so the concentration of fossil fuel burning in the northern midlatitudes results in Δ^{14}CO$_2$ depletion in the northern hemisphere [*Levin et al.*, 2003]. We model this surface flux using distributions of fossil CO_2 emissions from *Andres et al.* [1996]. Also, most of the

respired biomass in the 1990s was fixed when the atmosphere contained more bomb ^{14}C, with the result that since the 1980s, land biosphere respiration has been a net source of ^{14}C. This ^{14}C-enriched flux is highest in the tropics and in the north temperate zone where net primary production is high [*Randerson et al.*, 2002]. We modeled this flux using spatially and seasonally resolved biomass respiration pulse functions derived from the CASA biosphere model [*Thompson and Randerson*, 1999] convolved with the atmospheric Δ^{14}C history.

There has been significant interannual variability in the rate of decline of the Δ^{14}C of atmospheric CO_2 [e.g. *Levin and Kromer*, 2004]. We estimate this rate of decline as 7.0±0.6‰ / year for a 5-year period centered around 1994 by taking the average of available long-term atmospheric Δ^{14}C measurement series (Table 3.1). We estimated the contributions of the major influences on the atmospheric $^{14}CO_2$ isotopic budget (Table 3.2) and calculated the dependence of the ocean uptake on the parameters $\bar{k}$ and n. Uncertainty in several other contributions to the rate of decline was also around 0.6‰ / year (Table 3.2), and adding their contributions to the error variance yielded a total uncertainty of ±1.4‰ / year for the model-data comparison.

Published data on the latitudinal distribution of atmospheric Δ^{14}C in the 1990s are scarce. ^{14}C uptake in the Southern Ocean is the major influence on the Δ^{14}C gradient between the tropics and high southern latitudes, while Δ^{14}C gradients in the northern hemisphere are dominated by the influence of fossil carbon emissions [e.g. *Levin et al.*, 2003]. We compared the mean difference of 5.6±2.8‰ observed for 1993-1994 between Llano de Hato, Venezuela (9°N) and Macquarie Island in the Southern Ocean southeast of Australia (54°S) [*Levin and Hesshaimer*, 2000] to that predicted by our atmospheric

transport model for different air-sea gas exchange parameter values after accounting for the effect of other exchange processes (Table 3.2). Uncertainty in the predicted gradient due to model transport is about the same size as the reported measurement error but varies depending on the absolute size of the predicted gradient; the total uncertainty for the model-data comparison was about 4.5‰ (Table 3.2).

3.4.6 Preindustrial ocean ^{14}C uptake

We modeled air-sea ^{14}C fluxes using Equation 3, an atmospheric Δ^{14}C level of 0‰, and the GLODAP climatology of estimated pre-bomb ocean surface Δ^{14}C [*Key et al.*, 2004], which we corrected by using the a simulation with MOM (run with the *Wanninkhof* [1992] air-sea gas transfer velocity) to estimate the small depletion attributable to pre-bomb fossil fuel dilution.

The total amount of ^{14}C in the preindustrial ocean can be determined to an accuracy of perhaps 2% by integrating the pre-bomb ^{14}C distribution estimated by GLODAP and making a small correction for the effect of fossil fuel CO_2 to 1956. To estimate the preindustrial air-sea ^{14}C flux, one could assume steady state and take the net flux into the ocean to match the decay of ^{14}C in ocean DIC; this amount is 5.4 kg ^{14}C (2.3 $\times 10^{26}$ ^{14}C atoms) per year. This assumption is open to question, however, since it fails to account for exchange of DIC with other carbon pools with low Δ^{14}C, such as carbonate and organic sediment and volcanic or hydrothermal CO_2; the magnitude of this exchange is poorly known [*Damon and Sternberg*, 1989; *Goslar*, 2001]. For example, a plausible total input of 0.5 Pg per year of carbon containing essentially no ^{14}C would increase the steady-state air-sea flux required by 0.6 kg ^{14}C / year, or ~11%. In addition, some

deviation from steady state flux, caused for example by long-term oscillations in the atmospheric ^{14}C production rate [*Lingenfelter*, 1963] or in ocean circulation, is to be expected. Also allowing for uncertainty in the preindustrial ocean-surface $\Delta^{14}C$, we estimated the preindustrial air-sea flux at 5.4±1 kg ^{14}C / year and compared it with that predicted for different values of $\bar{k}$ and n.

The preindustrial interhemispheric $\Delta^{14}C$ gradient has been carefully measured (with replicate northern and southern samples analyzed in two laboratories to eliminate intercalibration error) as the offset in cellulose $\Delta^{14}C$ between tree rings from Britain and New Zealand [*Hogg et al.*, 2002]. Some oscillation over decade to century periods was found, with a mean ± standard deviation of 4.8±1.6‰ over the period 950-1850. (From earlier tree ring measurements, *Braziunas et al.* [1995] estimated a similar preindustrial gradient of 4.4±0.5‰ between the northern and southern midlatitudes.) We compared this gradient with that predicted by our atmospheric transport model to result from air-sea gas exchange for different values of $\bar{k}$ and n. Based on the spread of TransCom models, we estimated the atmospheric transport uncertainty at ±1.0‰, for a total uncertainty of ±1.9‰ for the model-data comparison.

3.4.7 Air-sea ^{13}C exchange

We constructed an isotopic budget of ^{13}C in the atmosphere for around 1995 based on the observed rate of decline in $\delta^{13}C$ of atmospheric CO_2 together with estimates of fossil fuel emissions and biosphere and ocean exchanges and their isotopic composition (Table 3.3), using an estimate of the oceanic uptake of anthropogenic CO_2 based on ocean DIC measurements [*Mikaloff Fletcher et al.*, in press] to determine the

relative magnitudes of land and ocean carbon uptake. This budget implies a disequilibrium air-sea ^{13}C isotope flux of 77±16 Pg C ‰ / year out of the ocean for the mid-1990s (Table 3.3), which agrees well with the estimate of 62±32 Pg C ‰ / year for a period centered in the 1980s derived by *Quay et al.* [2003] from observations of the decline in ocean δ^{13}C between the 1970s and 1990s. (Our simulation of ocean ^{13}C uptake suggests that the air-sea ^{13}C flux increased by some 14 Pg C ‰ / year between the mid-1980s and mid-1990s, further improving the agreement between our estimate and that of *Quay et al.* [2003].) If we account for a steady-state 8±4 Pg C ‰ / year flux into the ocean that balances the influx of ~0.4 Pg C / year of organic material depleted ~19‰ relative to the atmosphere that enters as runoff [*Heimann and Maier-Reimer*, 1996; *Aumont et al.*, 2001] (Table 3.3), we arrive at a total air-sea ^{13}C flux of 70±17 Pg C ‰ / year. We compared this value with the flux predicted by estimates of the air-sea δ^{13}C disequilibrium based on surface ocean measurements, combined with different formulations for air-sea gas transfer.

Extensive, accurate measurements of the δ^{13}C of sea-surface DIC were made for the first time in the 1980s and 1990s as part of WOCE and related cruises [*Gruber et al.*, 1999; *Quay et al.*, 2003]. We interpolated the sea-surface δ^{13}C measurements in GLODAP (mostly taken 1991-1999; median year, 1995) and used latitudinally and seasonally varying values for the δ^{13}C of atmospheric CO_2 for the mid 1990s based on measurements from the Scripps [*Keeling et al.*, 1995] and NOAA/CMDL [*Trolier et al.*, 1996] networks together with isotopic fractionation factors for air-sea exchange from *Zhang et al.* [1995] to predict the ^{13}C isotope flux for different global mean air-sea gas transfer velocities $\bar{k}$ and exponential dependences on windspeed n.

In comparing this predicted isotope flux with that inferred from the atmospheric record, additional uncertainties are introduced by possible error in the fractionation factors, by the interpolation of sea-surface $\delta^{13}C$, and by any intercalibration offset between the atmospheric and sea-surface $\delta^{13}C$ measurements. As a sensitivity test, we tried using the sea-surface $\delta^{13}C$ field of *Gruber and Keeling* [2001], based on different measurements and interpolation procedures, and found that the predicted global air-sea isotope flux was within about 5 Pg C ‰ / year of that obtained by interpolating $\delta^{13}C$ measurements from GLODAP, suggesting that interpolation and calibration errors in the $\delta^{13}C$ fields are probably smaller than the uncertainty in inferring the air-sea ^{13}C flux from atmospheric and other observations, which is of order ±17 Pg C ‰ / year (Table 3.3).

The latitudinal contrast in the direction of the ^{13}C isotope flux would have also existed in preindustrial times, and we can assume that, since the $\delta^{13}C$ of atmospheric CO_2 changed much more slowly, the net air-sea isotope flux was small. At steady state, we would expect only the aforementioned flux of 8±4 Pg C ‰ / year into the ocean, which balanced incoming river carbon. The preindustrial sea-surface $\delta^{13}C$ can be estimated from the WOCE-era distribution by subtracting from it the impact of recent exchange with atmospheric CO_2, whose $\delta^{13}C$ has been declining due to fossil emissions. We used a simulation with the MOM ocean transport fields, with the *Wanninkhof* [1992] air-sea gas exchange parameterization and a history of the decline in the $\delta^{13}C$ of atmospheric CO_2 since 1800 reconstructed from gas trapped in ice [*Francey et al.*, 1999], to estimate this perturbation in sea surface $\delta^{13}C$. To allow for error in the estimated perturbation, we increased the assumed uncertainty of the preindustrial flux to ±10 Pg C ‰ / year for the

purpose of comparing it with the predicted flux under different air-sea gas exchange

scenarios.

3.5 Results: Ocean bomb ^{14}C

3.5.1 Total amount of ocean bomb ^{14}C

The total ocean bomb radiocarbon uptake simulated using our ocean model

depends primarily on the global mean transfer velocity $\bar{k}$ (Figure 3.5). Increasing $\bar{k}$ by

1% increases the simulated GEOSECS-era inventory by around 0.8% and the WOCE-era

inventory by around 0.5%. Especially for the later (WOCE) period, modeled uptake is

also slightly greater at high n, since this shifts uptake in high latitudes, where more deep

water reaches the surface over a given period than at low latitudes so that the exchange-

weighted air-sea disequilibrium term $(\Delta_{sea}^{14}C - \Delta_{air}^{14}C)$ in Equation 4 is more negative.

When $\bar{k}$ is equal to the *Wanninkhof* [1992] value of 20.6 cm / hour, our model

ocean total is 293-309 $\times$ 10^{26} atoms for the beginning of 1975 and 348-382 $\times$ 10^{26} atoms

for mid-1994, depending on n (Figure 3.5). This amount is broadly consistent with

previous data-based estimates [*Broecker et al.*, 1995; *Key et al.*, 2004; *Peacock*, 2004].

On the grid we used, the GLODAP mapping of WOCE observations (mostly using

potential alkalinity to separate the bomb component) sums to 322 $\times$ 10^{26} atoms of bomb

radiocarbon (3% higher than the 313 $\times$ 10^{26} atoms reported by *Key et al.* [2004]). This

mapping excludes the Arctic Ocean and some marginal seas. Using our model

concentration field for 1994 to extrapolate to the entire ocean adds an additional 13% for

a WOCE-era total ocean amount of 364 $\times$ 10^{26} atoms (shown in Figure 3.5b). *Key et al.*

[2004] estimate the uncertainty on the total amount at 15%, or $\pm$55 $\times$ 10^{26} atoms. With

this uncertainty, the WOCE inventory implies a value of $\bar{k}$ in the range of 15-31 cm / hour (Figure 3.5b). This broad range is compatible with either the *Broecker et al.* [1995] estimate of $305\pm30 \times 10^{26}$ atoms or the *Peacock* [2004] estimate of some $270\pm25 \times 10^{26}$ atoms for the global GEOSECS-era ocean total, which imply values of $\bar{k}$ in the range of 18-24 or 15-20 cm / hour, respectively (Figure 3.5a).

The correlation between the bomb radiocarbon levels inferred from GLODAP ocean measurements and the modeled levels at the same time and space when $\bar{k}$ and n were close to the *Wanninkhof* [1992] values was +0.93, using either the potential alkalinity or the silica method to estimate the bomb radiocarbon component of the GLODAP observations. (This is higher than the corresponding correlation with CFC measurements, possibly because the slow air-sea exchange of ^{14}C as compared with CFCs makes its distribution less sensitive to seasonality in ocean transport patterns, which is not represented by our pulse functions.) At the *Wanninkhof* [1992] reference global mean gas transfer velocity $\bar{k}$ (20.6 cm / hour), our model reproduced fairly well the latitudinal structure estimated from measurements both for the GEOSECS period [*Broecker et al.*, 1995; *Peacock*, 2004] and for the WOCE period [*Key et al.*, 2004]. The amount of bomb ^{14}C in the Southern Ocean was better simulated if we assumed a linear dependence or no dependence of the transfer velocity on windspeed (Figure 3.6).

While the global total is relatively insensitive to the windspeed dependence n of the gas transfer velocity, Figure 3.6 suggests that the simulated latitudinal distribution of bomb radiocarbon is sensitive to n. The following approaches exploit observations of the regional distribution of bomb radiocarbon to estimate concurrently both $\bar{k}$ and n.

3.5.2 Estimates of the mean gas transfer velocity by region

Figure 3.7 shows the regional mean gas transfer velocities estimated from GEOSECS ocean radiocarbon measurements, compared with the values implied by the *Wanninkhof* [1992] parameterization. Figure 3.8 compares these estimated regional rates with those predicted using commonly used published parameterizations of the gas transfer velocity as a function of windspeed, shown as solid curves. The range of gas transfer velocities we estimated is somewhat higher than that implied by the *Wanninkhof* [1992] parameterization in the north subtropical, equatorial, and south subtropical Atlantic and in the eastern Equatorial Pacific, and somewhat lower in the north Pacific. We estimated the transfer velocity in the Southern Ocean (south of 45° S) at 21-30 cm / hour, considerably lower than the prediction of 38 cm / hour given by the *Wanninkhof* [1992] parameterization. Overall, a weak relationship with regional windspeed is evident (Figure 3.8), consistent with a roughly linear dependence of the gas transfer velocity on windspeed. Specifically, the best-fit power law relationship between regional root mean square windspeed and the estimated regional transfer velocities – derived by minimizing the 1-norm misfit, with the uncertainty for each of the estimated transfer velocities taken to be the range shown in Figure 3.7 (the gray vertical bars in Figure 3.8) – has an exponent n of 1.11±0.37 and a global mean $\bar{k}$ of 20.6±0.6 cm / hour (black dashed curve in Figure 3.8). This relationship implies typically higher gas transfer velocities at low windspeeds and lower rates at high windspeeds than the *Wanninkhof* [1992] quadratic or *Wanninkhof and McGillis* [1999] cubic dependence, but essentially the same global mean transfer velocity, and higher transfer velocities at all windspeeds compared with the *Liss*

and Merlivat [1986] and *Nightingale et al.* [2000] relationships, which yield lower global

mean transfer velocities (Figure 3.8).

3.5.3 Global parameterization of gas exchange as a function of windspeed

Figure 3.9 shows the optimum values of the global mean gas transfer velocity $\overline{k}$

and the windspeed dependence exponent n (Equation 3) obtained by minimizing the

misfit of modeled with measured bomb ^{14}C. Figure 3.9a shows the optimum values for

$\overline{k}$ and n estimated by fitting individual ocean GEOSECS (1970s) bomb ^{14}C

measurements or their column integrals; Figure 3.9b show the corresponding results

when 1980s-1990s (mostly WOCE) data were used. In each panel, the letter A and the

contour lines show the minimum misfit obtained using the individual measurements and

the GLODAP bomb component estimate (based on potential alkalinity); B shows the

minimum misfit for individual measurements and a bomb component estimate based on

silica; and C and D show the minimum misfit obtained using column integrals and,

respectively, potential alkalinity or silica-based estimates of the bomb component. The

posterior uncertainties, assuming that the each measurement is independent, were small –

for example, about 0.25 cm / hour for $\overline{k}$ and 0.06 for n when using individual GEOSECS

measurements – compared with the variability in the misfit minimum location between

the cases. It is likely that much of the error is highly correlated between individual

measurements, so that our assumption of uncorrelated errors greatly underestimates the

actual error (overestimates the effective number of data degrees of freedom).

Across all cases, we found the best-fit windspeed dependence of the gas transfer

velocity to be consistently less than quadratic, with the exponent n ranging from below

zero (which would mean that regions with low mean windspeed tend to have high gas

transfer velocities) to about 1, while $\bar{k}$ ranged from 17 to 25 cm / hour. With no obvious

cause to believe that any of the cases we tried yields more reliable results than the others,

we took the mean and standard deviation of the minimum-misfit $\bar{k}$ and n values across

the cases shown in Figure 3.9 (first setting any negative values for the optimum n to 0) to

obtain n = 0.61±0.40 and $\bar{k}$ = 20.7±2.4 cm / hour. We then averaged these values of $\bar{k}$

and n with those obtained by first estimating the transfer velocity for each region (see

previous section), but retained the larger of the two approaches' standard deviations to

allow for systematic error in either of them. This gave $\bar{k}$ = 21±2 cm / hour and n =

0.9±0.4 as the parameters in a power-law relationship of gas transfer velocity with

windspeed (Equation 3) that best reproduce the observed ocean distribution of bomb

carbon-14. We turn to other carbon-14 and carbon-13 observations to determine whether

these results are robust – in particular, whether our finding that n < 2 holds up.

3.6 Results: Other ^{14}C and ^{13}C observations

3.6.1 1990s air-sea ^{14}C exchange

Our fit for the dependence of the gas transfer velocity on windspeed to ocean

bomb radiocarbon observations (taking $\bar{k}$ = 21 cm / hour and n = 0.9) yielded a predicted

atmospheric Δ^{14}C decline rate of 7.7‰ / year, while the predicted decline rate was 8.7‰ /

year assuming the *Wanninkhof* [1992] quadratic dependence on windspeed, and 9.7‰ /

year assuming the cubic dependence of *Wanninkhof and McGillis* [1999] (Figure 3.10a).

The observed decline rate together with our estimate of the combined measurement

uncertainty and uncertainties in the other influences (Table 3.1) of 7.0±1.4‰ / year

implies that if we assume that $\bar{k}$ is 21 cm / hour, then n is around 0.3. The 1-σ range given the estimated uncertainty of 1.4‰ is 0-1.6, meaning that a quadratic or cubic dependence on windspeed yields too fast an atmospheric $\Delta^{14}C$ decline rate. If we assume that n = 0.9, $\bar{k}$ is 19±4 cm / hour.

At the *Wanninkhof* [1992] value for $\bar{k}$, the predicted Venezuela-Southern Ocean gradient was 4.2‰ for our parameterization of the dependence of the gas transfer velocity on windspeed, 7.5‰ assuming a quadratic dependence, and 10.8‰ assuming a cubic dependence (Figure 3.10b). The measured gradient of 5.6±4.5‰, suggests that n is around 1.3 (range: 0-2.7) if we assume that $\bar{k}$ is 21 cm / hour. If we assume that n = 0.9, the latitudinal gradient suggest that $\bar{k}$ is 24±11 cm / hour.

In our simulations using an atmospheric model, the windspeed dependence of the gas exchange transfer velocity was predicted to have a dominant effect on the latitudinal variation in atmospheric $\Delta^{14}C$ in the southern hemisphere (Figure 3.11). Accurate measurements and models may be able to use this latitudinal variation to determine the mean transfer velocity in the Southern Ocean independently of ocean-interior ^{14}C.

3.6.2 Preindustrial air-sea ^{14}C exchange

The dependence of the ocean uptake estimated from the sea-surface $\Delta^{14}C$ distribution on n was weak: the predicted air-sea flux was 5.5 kg ^{14}C / year for our parameterization for the dependence of the gas transfer velocity on windspeed (n=0.9), 5.8 assuming a quadratic dependence (n=2, as in *Wanninkhof* [1992]), and 6.2 assuming a cubic dependence (n=3, as in *Wanninkhof and McGillis* [1999]). Pending more detailed knowledge of preindustrial ^{14}C flows in the oceans, these all seem plausible. Conversely,

as long recognized [*Craig*, 1957; *Broecker and Peng*, 1982, Chapter 3], the preindustrial ^{14}C steady state does fix the global mean transfer velocity $\overline{k}$ to within ~25%, supporting the range we and earlier workers derived from ocean bomb ^{14}C measurements. Specifically, if we assume that the windspeed dependence exponent n is 0.9, $\overline{k}$ must be 21±4 cm / hour for the air-sea flux to have been in the range of 5.4±1 kg / year.

We also compared the observed preindustrial Britain-New Zealand gradient in atmospheric $\Delta^{14}C$ of 4.8±1.6‰ with that predicted by our atmospheric transport model for different values of $\overline{k}$ and n (Figure 3.10d). The predicted gradient was 4.6‰ for our parameterization of the dependence of the gas transfer velocity on windspeed, 5.9‰ assuming the *Wanninkhof* [1992] quadratic dependence, and 7.2‰ assuming the *Wanninkhof and McGillis* [1999] cubic dependence. If we assume a global mean velocity $\overline{k}$ of 21 cm / hour, the observed gradient of 4.8‰ suggests that n is around 1.1 (range: 0-2.5); if we assume that the windspeed dependence exponent n is 0.9, the observed gradient suggests that $\overline{k}$ is 22±9 cm / hour.

3.6.3 The air-sea ^{13}C isotope flux

The air-sea ^{13}C isotope flux only weakly constraints the mean gas transfer velocity (Figure 3.12a). However, it provides strong support for a low windspeed exponent. The predicted 1990s fluxes were 58 Pg C ‰ / year for our gas exchange parameterization, 37 Pg C ‰ / year for the *Wanninkhof* [1992] quadratic dependence on windspeed, and 19 Pg C ‰ / year for the *Wanninkhof and McGillis* [1999] cubic dependence. Comparing the predicted isotope fluxes with that estimated from the atmospheric ^{13}C budget (Table 3.3) suggested that the windspeed dependence exponent n

is low (Figure 3.12a). If $\bar{k} = 21$ cm / hour, n must be around 0.1 (range: 0-1.2) for the

isotope flux to 70±17 Pg C ‰ / year as inferred from observations.

In the reconstructed preindustrial case, a steady state assumption also implied a

relatively low dependence on windspeed (Figure 3.12b). The predicted fluxes (with the

negative sign denoting an isotope flux of ^{13}C into the ocean) were −5 Pg C ‰ / year for

our gas exchange parameterization, −19 Pg C ‰ / year for the *Wanninkhof* [1992]

quadratic dependence on windspeed, and −34 Pg C ‰ / year for the *Wanninkhof and*

McGillis [1999] cubic dependence. Again, if $\bar{k} = 21$ cm / hour, n must be around 1.1

(range: 0.3-1.9) for the isotope flux to be within the range of −8±10 Pg C ‰ / year

implied under a steady-state assumption.

3.7 Discussion

3.7.1 The air-sea gas transfer velocity: Comparison with previous results

Our comparison of modeled with measured ocean bomb radiocarbon distributions,

whether we solve for mean transfer velocity by region or solve for a best-fit exponential

relationship with windspeed, suggests that globally, long-term mean gas exchange

increase roughly linearly with root-mean-square windspeed (n = 0.9±0.4), and that

latitudinal gradients in the gas transfer velocity are smaller than a quadratic or, especially,

a cubic dependence on windspeed would imply. The requirement of an approximate

preindustrial steady state constrains the global mean transfer velocity $\bar{k}$ (Figure 3.10c),

and yields values that cover the range we obtained from ocean bomb radiocarbon data.

The preindustrial latitudinal gradient, as well as 1990s ocean surface and atmospheric

measurements, are also sensitive to the windspeed dependence exponent n (Figure

3.10abd), although measurement and other uncertainties meant that some of the data we considered are consistent with a wide range in n. The observed decline rate of atmospheric $\Delta^{14}C$, as well as the requirement that the air-sea ^{13}C isotope flux estimated from sea-surface $\delta^{13}C$ measurements be consistent with the recent atmospheric $\delta^{13}C$ history and with an approximate preindustrial steady-state (Figure 3.12), constrain n to be less than 2, which agrees with the range we estimate from ocean bomb radiocarbon data. Table 3.4 lists the values for $\bar{k}$ and n estimated from the various approaches we have presented. Our estimate of the global mean air-sea gas transfer velocity for ice-free water at a Schmidt number of 660 – 21±2 cm / hour – matches well with earlier estimates based on ocean bomb radiocarbon [*Broecker et al.*, 1985], natural radiocarbon [*Broecker and Peng*, 1982], and radon-222 [*Peng et al.*, 1979].

If we take $\bar{k}$ = 21±2 cm / hour and n = 0.9±0.4, our ocean transport simulations suggest that the total amount of bomb radiocarbon in the ocean was some $305\pm24 \times 10^{26}$ atoms at the beginning of 1975 (very similar to the estimate of *Broecker et al.* [1995] and somewhat higher than that of *Peacock* [2004]) and $368\pm21 \times 10^{26}$ atoms at the middle of 1994 (very similar to the estimate of *Key et al.* [2004] when adjusted for the ocean volume excluded from their inventory). We found no indication from observations of ocean bomb or natural radiocarbon uptake that the global mean air-sea gas transfer velocity is much lower than the original estimates based on GEOSECS, as *Hesshaimer et al.* [1994] argue.

Some earlier studies support our result of a relatively weak latitudinal variation in the mean air-sea gas transfer velocity. These include the radon-222 profiles evaluated by *Peng et al.* [1979], reflecting gas transfer velocity averaged over a few days, which

showed little effect of windspeed and a fairly weak latitudinal gradient, and the study of

preindustrial ^{14}C by *Braziunas et al.* [1995], which found it necessary to revise the mean

air-sea transfer velocity in the Southern Ocean (south of 50°S) down to ~31 cm / hour to

account for the relatively small north-south Δ^{14}C gradient found in tree rings. A low

dependence of the gas transfer velocity on windspeed was also found to be most

consistent with preindustrial steady-state for the air-sea ^{13}C isotope flux in an analysis by

Heimann and Monfray [1989] based on sparse GEOSECS measurements of sea-surface

δ^{13}C.

The formulations for quadratic or cubic dependence of gas transfer on windspeed

proposed by *Wanninkhof* [1992] and *Wanninkhof and McGillis* [1999] respectively were

largely based on field studies that used tracer release experiments or eddy covariance

measurements of gas fluxes to evaluate the dependence of gas exchange on windspeed,

typically over a few days to weeks. Extrapolating from the results of a few measurement

campaigns to a relationship with windspeed suitable for use globally is inherently very

uncertain, though. Direct measurement of air-sea gas fluxes is difficult and is subject to a

number of sources of potential and systematic error, despite recent technical

improvements [e.g. *Fairall et al.*, 2000]. Also, the apparent dependence of gas exchange

on a variety of factors not directly tied to windspeed, including surfactants, rain, and

wave height [*Frost and Upstill-Goddard*, 1999; *Woolf*, 2005], means that the gas transfer

velocity at a given windspeed could vary considerably between places and seasons

depending on these other conditions. This is particularly true for extrapolations of the

transfer velocity to high windspeed, where theory and laboratory evidence suggest that

the gas transfer velocity saturates under some conditions [*Komori et al.*, 1993; *Donelan et*

al., 2004]. As an example of the influence of factors other than windspeed, *McGillis et al.* [2004] found that the gas transfer velocity inferred from CO_2 eddy covariance in the eastern equatorial Pacific varied little with windspeed but was strongly affected by temperature gradients in the ocean mixed layer, which promoted surface turbulence.

Our technique of deducing a parameterization of the gas transfer velocity from observations of large-scale air-sea carbon isotope exchanges implicitly averages across this variability, resulting in a parameterization that represents regional-scale gas exchange over timescales of months to decades. Accurate long-term direct measurements of gas exchange at many representative sites would greatly improve understanding of the relative importance of different factors in governing variability in air-sea exchange across seasons and ocean regions and help suggest better parameterizations based on windspeed or other surface properties that can be determined remotely.

A recent review of field and laboratory measurements of the gas transfer velocity over a wide range of windspeeds [*Zhao et al.*, 2003] found an overall power law exponent of 1.35, only slightly higher than our result of 0.9±0.4. *Zhao et al.* also propose that the gas transfer velocity is better correlated with whitecap coverage than with windspeed. This would be because whitecap coverage reflects both windspeed and other factors that influence the gas transfer velocity, such as the presence of organic surfactant films that inhibit turbulence and the degree to which waves are fully developed at the given wind stress (which depends on the consistency of the wind direction and the distance from shore). It would be worth examining whether a parameterization based on whitecap coverage would better account for the regional variability we found in the mean gas transfer velocity, compared with a parameterization based only of windspeed.

Whitecap coverage can be remotely determined using satellite instrumentation similar to that used for sensing windspeed [*Monahan*, 2002]. Sea-surface mean square slope is another quantity that can be sensed remotely from microwave backscatter measurements and has been suggested to predict the gas transfer velocity better than windspeed [*Frew et al.*, 2004; *Turney et al.*, 2005].

3.7.2 Implications for air-sea CO$_2$ fluxes

We examined the effect of air-sea gas exchange parameterizations on the air-sea CO$_2$ flux implied by the climatology of air-sea pCO$_2$ difference compiled by *Takahashi et al.* [2002] for a nominal year of 1995 (Figure 3.13). The total uptake is sensitive to n as well as $\overline{k}$, since the tropical oceans, with low mean windspeeds, tend to release CO$_2$ while the high-latitude oceans, with higher mean windspeeds, tend to take it up. With this surface pCO$_2$ climatology, the predicted anthropogenic uptake is 1.8 Pg C / year using our parameterization of the gas transfer velocity dependence on windspeed, 2.5 Pg C / year using the *Wanninkhof* [1992] quadratic dependence, and 3.0 Pg C / year assuming the *Wanninkhof and McGillis* [1999] cubic dependence (Figure 3.13a). The uncertainty in ocean CO$_2$ uptake estimated using this method is large, because small adjustments to sea-surface pCO$_2$ due to, for example, the skin temperature correction for evaporative cooling [*Van Scoy et al.*, 1995; *Ward et al.*, 2004] and respiration by microorganisms in the surface microlayer [*Garabetian*, 1991], as well as to errors induced by lack of sampling in some seasons and regions, have a large impact on the inferred global uptake. Independent observational estimates of anthropogenic ocean CO$_2$ uptake include 2.2±0.3 Pg C / year for around 1995 based on the C* method for estimating the anthropogenic

enhancement of ocean DIC combined with several ocean circulation models [*Mikaloff Fletcher et al.*, in press], 2.0±0.4 Pg C / year for the 1990s based on water ages inferred from ocean CFC measurements [*McNeil et al.*, 2003], and 2.4±0.7 Pg C / year for the 1990s based on atmospheric oxygen measurements [*Plattner et al.*, 2002].

Figure 3.13b shows the CO_2 flux by latitude estimated from the *Takahashi et al.* [2002] pCO_2 climatology using our gas transfer velocity parameterization compared with quadratic and cubic dependences on windspeed. Our lower windspeed dependence implies less CO_2 uptake in the Southern Ocean and shifts the maximum uptake there north by several degrees, which resolves part of the discrepancy between the high Southern Ocean CO_2 uptake implied by this pCO_2 climatology and a quadratic or cubic dependence of gas exchange on windspeed and the low Southern Ocean CO_2 uptake inferred from the stable atmospheric CO_2 concentrations measured when going across the Southern Ocean [*Roy et al.*, 2003]. The regional distribution of the ocean CO_2 uptake implied by a quadratic dependence on windspeed is used as a prior constraint in many inversions for regional CO_2 fluxes that are based on atmospheric CO_2 measurements [e.g. *Gurney et al.*, 2003], so adopting a different dependence on windspeed could also affect the regional CO_2 sources and sinks inferred from such inversions. For example, the network of CO_2 observation stations does not distinguish land from ocean carbon sources and sinks in the tropics, so this assignment depends on the use of other information, such as the distribution of the air-sea CO_2 flux [e.g. *Krakauer et al.*, 2004]. If CO_2 outgassing from the equatorial ocean is more intense than previously assumed, a smaller tropical land source might be required to explain the observed patterns in atmospheric CO_2 concentration.

Our higher estimate for the gas transfer velocity in the eastern equatorial Pacific highlights the potential significance of pCO_2 variations there with ENSO [*Feely et al.*, 1999; *Feely et al.*, 2004b] for interannual variability in ocean CO_2 uptake. Conversely, a smaller dependence of gas exchange on windspeed makes it less likely that changes in storm frequencies are a major contributor to interannual variability in the ocean sink [*Bates*, 2002; *Perrie et al.*, 2004].

3.7.3 Estimating gas transfer velocities from carbon isotope distributions: Limitations and directions for improvement

Our analysis attempted to find the power law relationship of the gas transfer velocity with a particular satellite-based windspeed climatology that best fit a variety of atmosphere and ocean carbon isotope observations. This wind climatology could be supplemented with other satellite products to investigate whether using different wind climatologies makes any difference for the best-fit parameterization of gas transfer velocity, and the possible impact of interannual variability in winds could be checked using satellite products as well as reanalysis wind fields.

Given our finding of an approximately linear relationship of the gas transfer velocity to windspeed, it may be better to use, for example, arithmetic mean windspeed instead of the root-mean-square we used, which is best if the relationship of gas transfer velocity to windspeed is close to quadratic [cf. *Wanninkhof et al.*, 2004; *Olsen et al.*, 2005 for discussions of the impact of using different wind products and moments]. Also, a more complex function for the dependence of the gas transfer velocity on windspeed, in which, for example, the transfer velocity levels off at low windspeeds and plateaus at

high windspeeds, may well better represent the variability in the transfer velocity over a variety of time and space scales than the simple power law relationship that we assumed.

Some of the data sets that we used to calculate the air-sea bomb radiocarbon flux could be improved. The zonal distribution of atmospheric $\Delta^{14}C$ in the 1960s, when gradients were very large, should be revisited in light of expanded tropical tree ring measurements [*Hua et al.*, 1999; *Hua and Barbetti*, 2004].

Judging by the differences we found between methods based on potential alkalinity and on silica for estimating the pre-bomb ocean $\Delta^{14}C$ distribution, which is used to determine the bomb ^{14}C component in post-bomb $\Delta^{14}C$ measurements, the pre-bomb $\Delta^{14}C$ distribution is a significant source of uncertainty. This is particularly important for the Southern Ocean, where because of more extensive mixing the absolute bomb $\Delta^{14}C$ enhancements tend to be smaller and thus harder to quantify, and where few early $\Delta^{14}C$ measurements were made [*Broecker et al.*, 1960]. Measurements of $\Delta^{14}C$ in banded ahermatypic corals [*Goldstein et al.*, 2001; *Frank et al.*, 2004], which grow in cold water, could help calibrate the pre-bomb $\Delta^{14}C$ profile in the Southern Ocean. Coral $\Delta^{14}C$ timeseries in general provide unique chronologies of bomb radiocarbon arrival, and could supplement single measurements of water $\Delta^{14}C$ such as the ones in GLODAP as evidence for air-sea gas transfer velocity.

Another uncertainty in our ocean bomb ^{14}C results comes from our ocean transport model. While our model appears to represent the global inventory and latitudinal distribution of tracers such as CFCs and bomb ^{14}C quite accurately over decadal timescales, it is harder to validate its skill in assigning uptake to smaller regions, especially given the low resolution imparted by using regional pulse functions.

Intercomparison of bomb radiocarbon distribution dependence on air-sea transfer velocity over different transport models, similar to the OCMIP-3 project of solving for best-fit air-sea CO_2 fluxes from different models [*Mikaloff Fletcher et al.*, in press], would at least permit better assessment of the magnitude of transport error. Ultimately, a fully inverse approach, where ocean circulation fields and the distribution of the mean air-sea gas transfer velocity are estimated simultaneously using measurements of bomb ^{14}C together with other ocean tracers [cf. *Schlitzer*, 2000] within an ocean data assimilation framework such as ECCO, is likely to be the most effective way to utilize the large number of available ocean $\Delta^{14}C$ measurements to infer detailed spatial patterns in gas transfer velocity.

We have shown that the 1990s rate of decline in and latitudinal profile of the $\Delta^{14}C$ of atmospheric CO_2 reflect the latitudinal distribution of the air-sea gas transfer velocity. Continued measurement of atmospheric $\Delta^{14}C$ and of sea-surface $\Delta^{14}C$ in the Southern Ocean would therefore provide information about the mean rate of air-sea gas exchange in the Southern Ocean averaged over the atmospheric transport timescale (a few months), and in principle could even detect seasonal and interannual variability in the Southern Ocean transfer velocity, although the precision requirement is high. Given the importance of Southern Ocean gas exchange to climate and to CO_2 uptake [*Liss et al.*, 2004], a long-term measurement program should be encouraged.

We have also shown that the ongoing air-sea isotopic flux of ^{13}C, as well as the preindustrial flux, provides information about the windspeed dependence of the gas transfer velocity if the spatial distribution of the air-sea $\delta^{13}C$ disequilibrium is well known. Further work is needed to find the best way of estimating this distribution from

available measurements, possibly replacing the simple interpolation that we used with a more sophisticated approach using ocean transport models to map ocean surface $\delta^{13}C$ in a way consistent with measurements, and to more fully assess the uncertainties in $\delta^{13}C$ measurements and in the equilibrium air-sea isotopic fractionation.

3.8 Conclusions

The air-sea gas transfer velocity is important for quantifying the ocean gas exchange, and both field measurements and indirect inference from tracer distributions can help in developing a consistent formulation for it. We have estimated the mean gas transfer velocity both by region and as a function of climatological monthly windspeed from ocean bomb carbon-14 measurements as well as from other carbon-14 and carbon-13 data. Although many of the approaches we used yield substantial uncertainties, our results support a roughly linear increase of gas transfer velocity with windspeed in the global ocean (best-fit exponent: 0.9±0.4; global mean rate: 21±2 cm / hour at a Schmidt number of 660).

To account for model transport error, we recommend either comparing carbon-14 distributions for multiple models or else solving for transport simultaneously with air-sea exchange. High-precision measurement of atmospheric carbon-14 may be able to provide independent information on air-sea exchange, especially for the Southern Ocean.
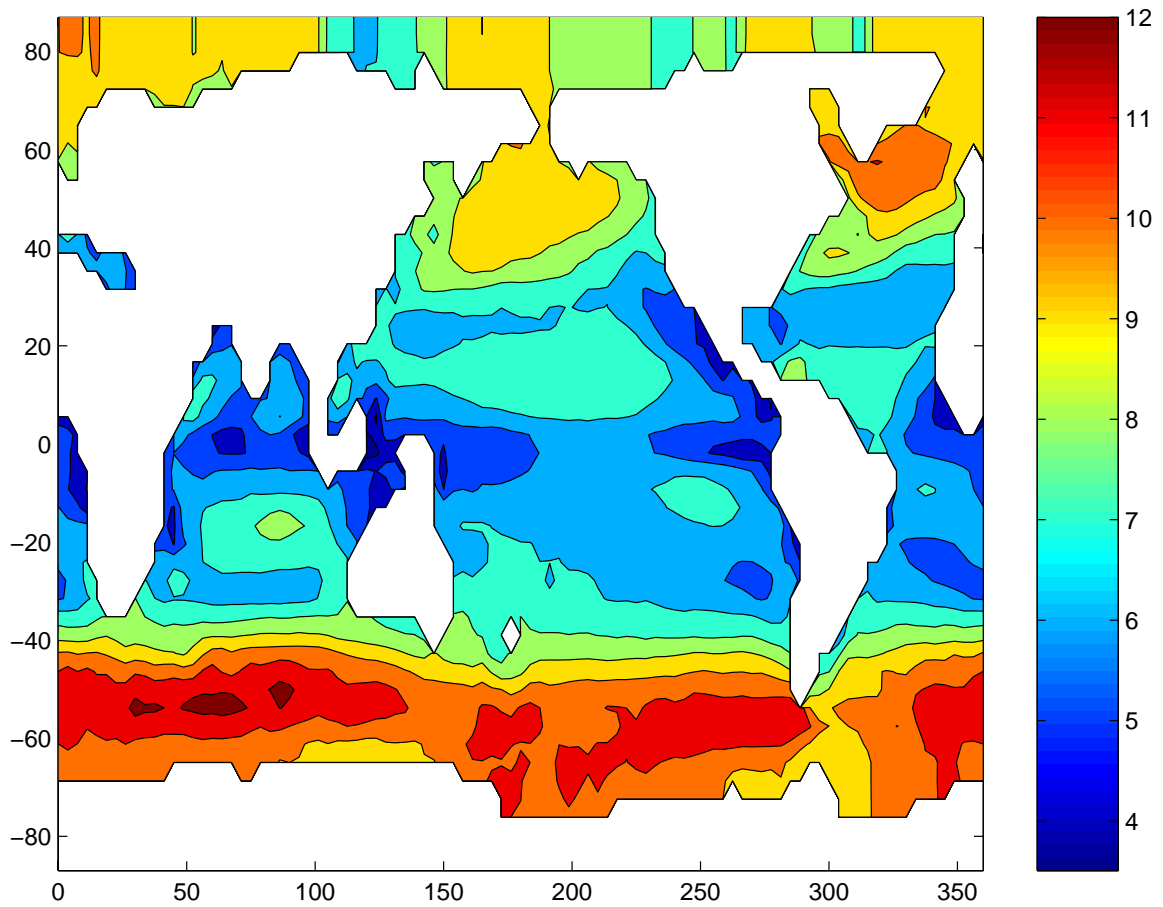
Figure 3.1. Annual-mean root-mean-square windspeed (m/s) over the ocean, at 10 m height, from the monthly climatology of *Boutin and Etcheto* [1997; *Orr et al.*, 2001], derived from satellite (SSM/I) data. We used the monthly climatology to explore the consequences of different dependences of the air-sea gas transfer velocity on windspeed on ocean carbon-14 uptake. The RMS windspeed varies from 5-6 m/s near the equator to around 11 m/s in the Southern Ocean.
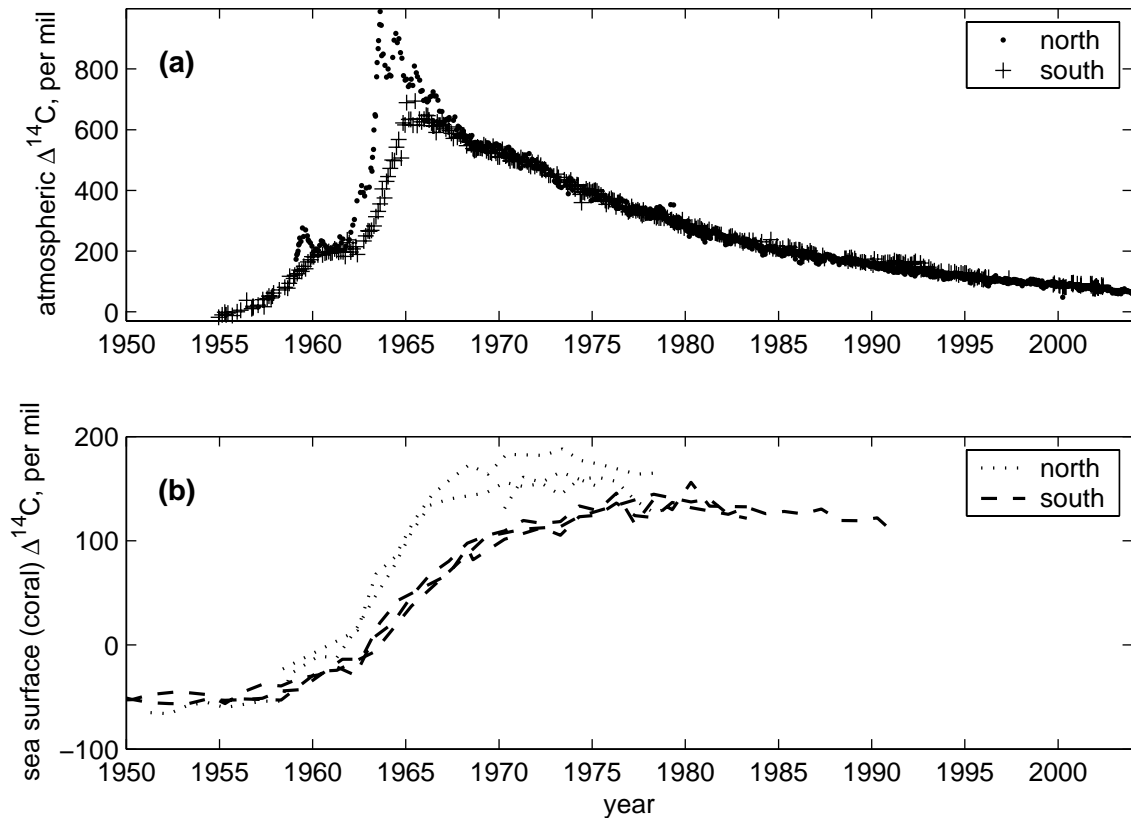
Figure 3.2. Representative northern and southern hemisphere observational timeseries of $\Delta^{14}C$ for CO_2 in air and for DIC in the upper ocean, showing the bomb radiocarbon spike. (a) Measurements of $\Delta^{14}C$ in atmospheric CO_2 in central Europe (46°-48°N) [*Levin and Kromer*, 2004] and in New Zealand (41°S) [G. Brailsford, personal communication, updating *Manning et al.*, 1990], at approximately fortnightly resolution. (b) Measurements of $\Delta^{14}C$ in subtropical (20°-25° N and S) surface coral, at approximately annual resolution. The northern corals are from Florida [*Druffel*, 1989] and Oahu and French Frigate Reef in Hawaii [*Druffel*, 1987]. The southern corals are from Abraham Reef, Heron Island, and Lady Musgrave Island, all in the Great Barrier Reef off Australia [*Druffel and Griffin*, 1995].
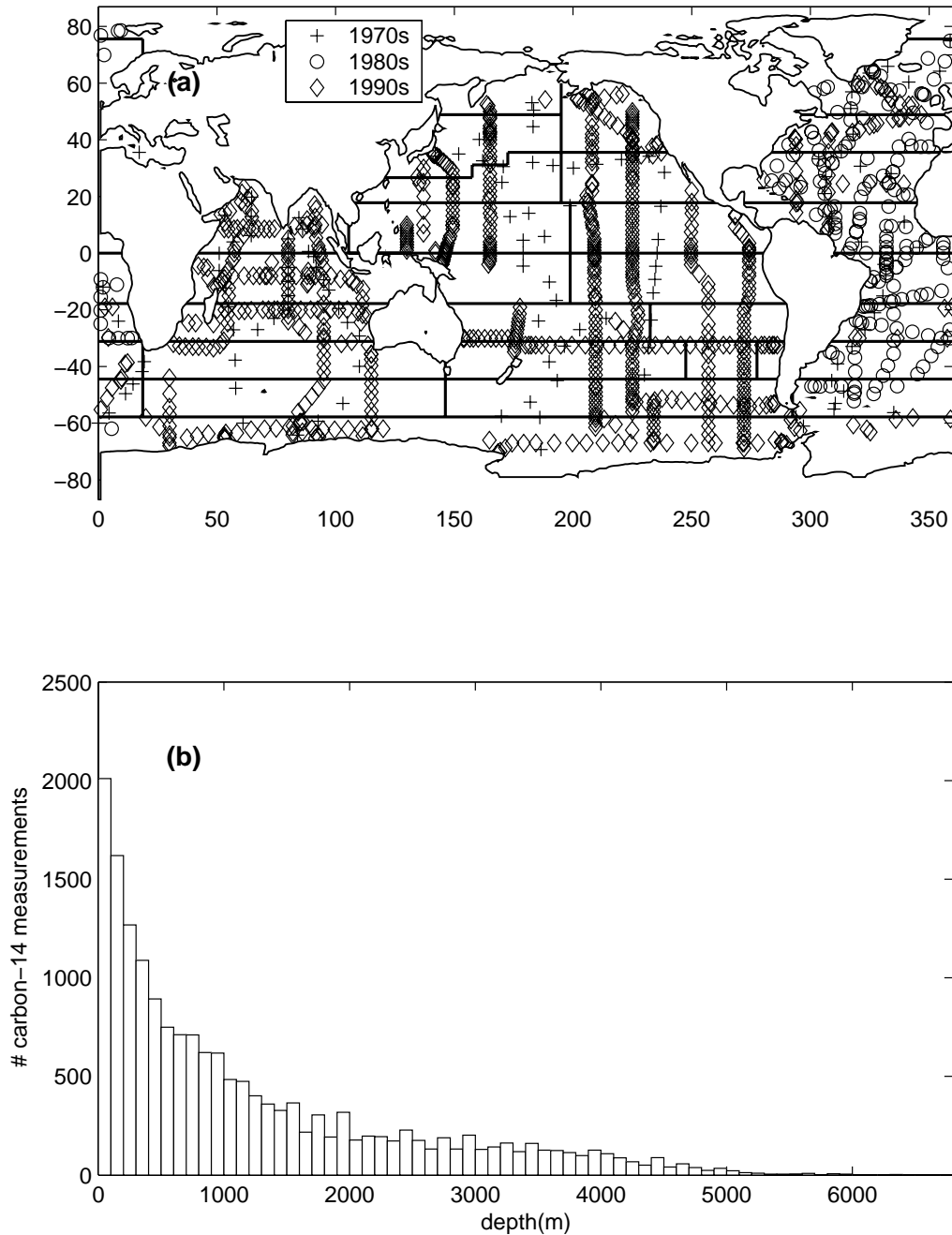
Figure 3.3. Distribution of the ocean radiocarbon measurements used in this analysis [*Key et al.*, 2004]. (a) Location of measurements, grouped by decade. The 1970s measurements were made as part of GEOSECS, the 1990s measurements mostly as part of WOCE. The thick lines are the boundaries between the 30 ocean regions we use as basis regions for transport pulse functions. (b) Depth distribution of measurements (100-m bins).
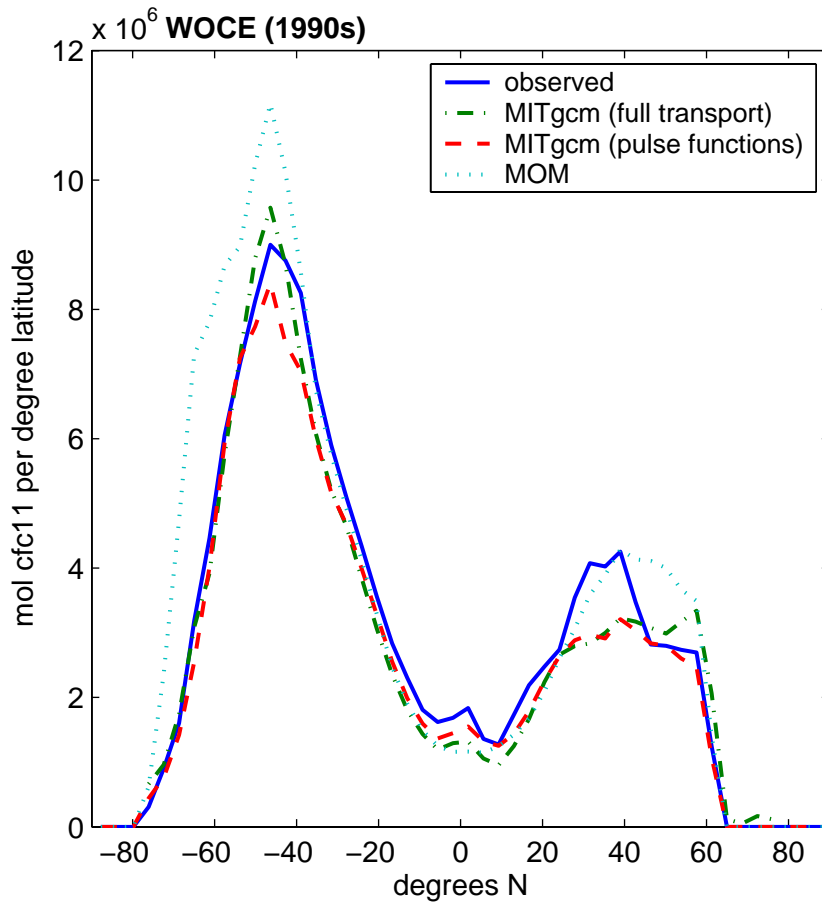
Figure 3.4. Modeled 1994 latitudinal distribution of the chlorofluorocarbon CFC-11 with the OCMIP gas transfer velocity parameterization, compared to a gridded distribution based on observations [*Key et al.*, 2004]. For MITgcm, modeled distributions derived using both full transport fields and regional pulse functions are shown; we used the latter to model bomb radiocarbon uptake. We used MOM for reconstructing preindustrial sea-surface $\Delta^{14}C$ and $\delta^{13}C$. The modeled distributions are summed only over the grid cells for which the gridded distribution is available, largely excluding, for example, the Arctic Ocean.

(a) inventory: GEOSECS (1970s)

(b) inventory: WOCE (1990s)
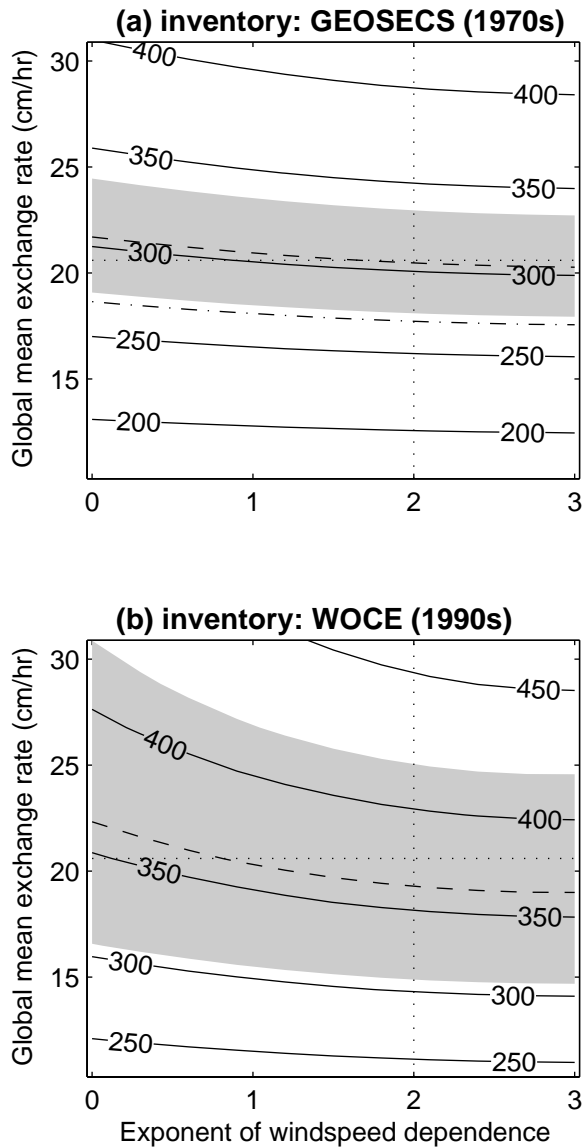
Figure 3.5. Our model-predicted total ocean bomb radiocarbon amount, in 10^{26} atoms, at the middle of the (a) GEOSECS and (b) WOCE measurement programs (1975.0 and 1994.5, respectively), when the model is run with air-sea gas exchange following Equation 4 with different values of the windspeed dependence exponent n and the global mean rate $\overline{k}$. Corresponding observation-based amounts from *Broecker et al.* [1995] ($305\pm30 \times 10^{26}$ atoms; dashed line and shading in (a)), *Peacock* [2004] ($270\pm25 \times 10^{26}$ atoms; dot-dashed line in (a)), and *Key et al.* [2004] ($364\pm55 \times 10^{26}$ atoms; dashed line and shading in (b)) are also shown. The dotted lines show the values for these parameters used in OCMIP [*Wanninkhof,* 1992].
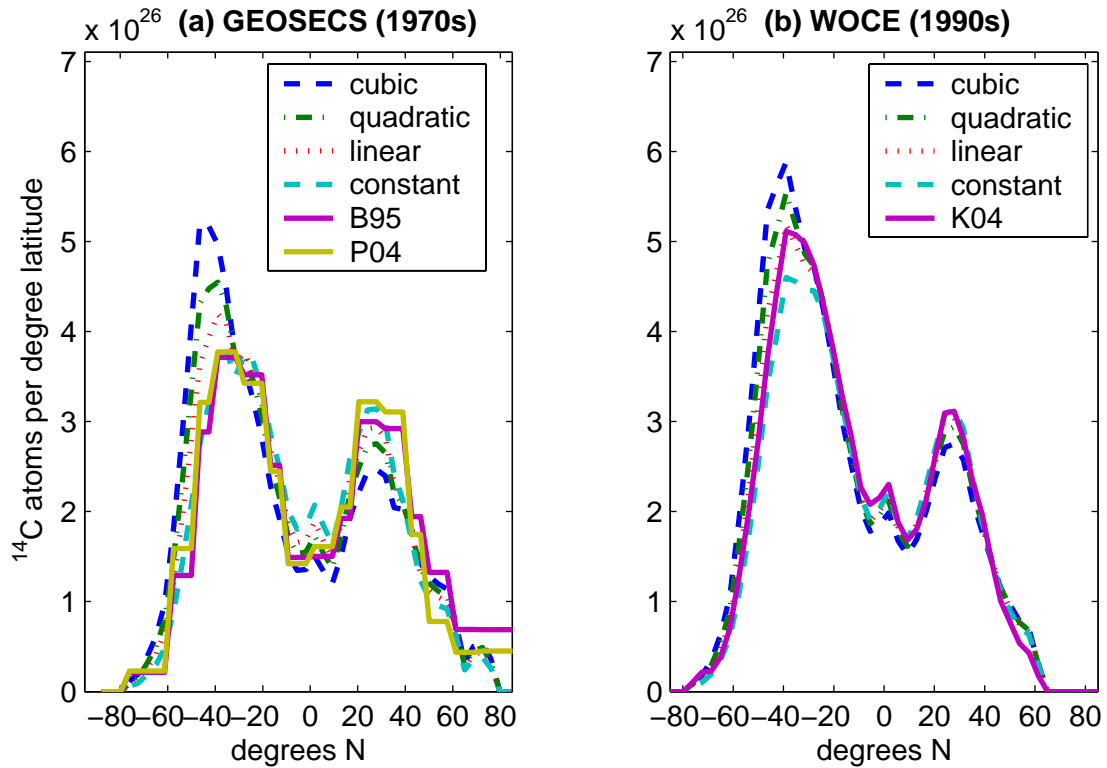
Figure 3.6. Modeled latitudinal distribution of bomb carbon-14 in the ocean, for a global mean gas transfer velocity $\bar{k}$ of 20.6 cm / hour and a dependence on windspeed ranging from cubic to none (n=3, 2, 1 or 0). A lower dependence on windspeed leads to relatively less uptake at the midlatitudes and more near the equator. In panel a, the 1975.0 modeled distribution is compared with extrapolations from GEOSECS observations in 10° bands by *Broecker et al.* [1995] and by *Peacock* [2004] (mean of her CFC- and anthropogenic CO_2-based extrapolation approaches). In panel b, the 1994.5 modeled distribution is compared to the GLODAP gridded distribution based on WOCE observations [*Key et al.*, 2004]; the modeled distribution is summed only over the grid cells for which the gridded distribution is available, excluding, for example, the Arctic Ocean.
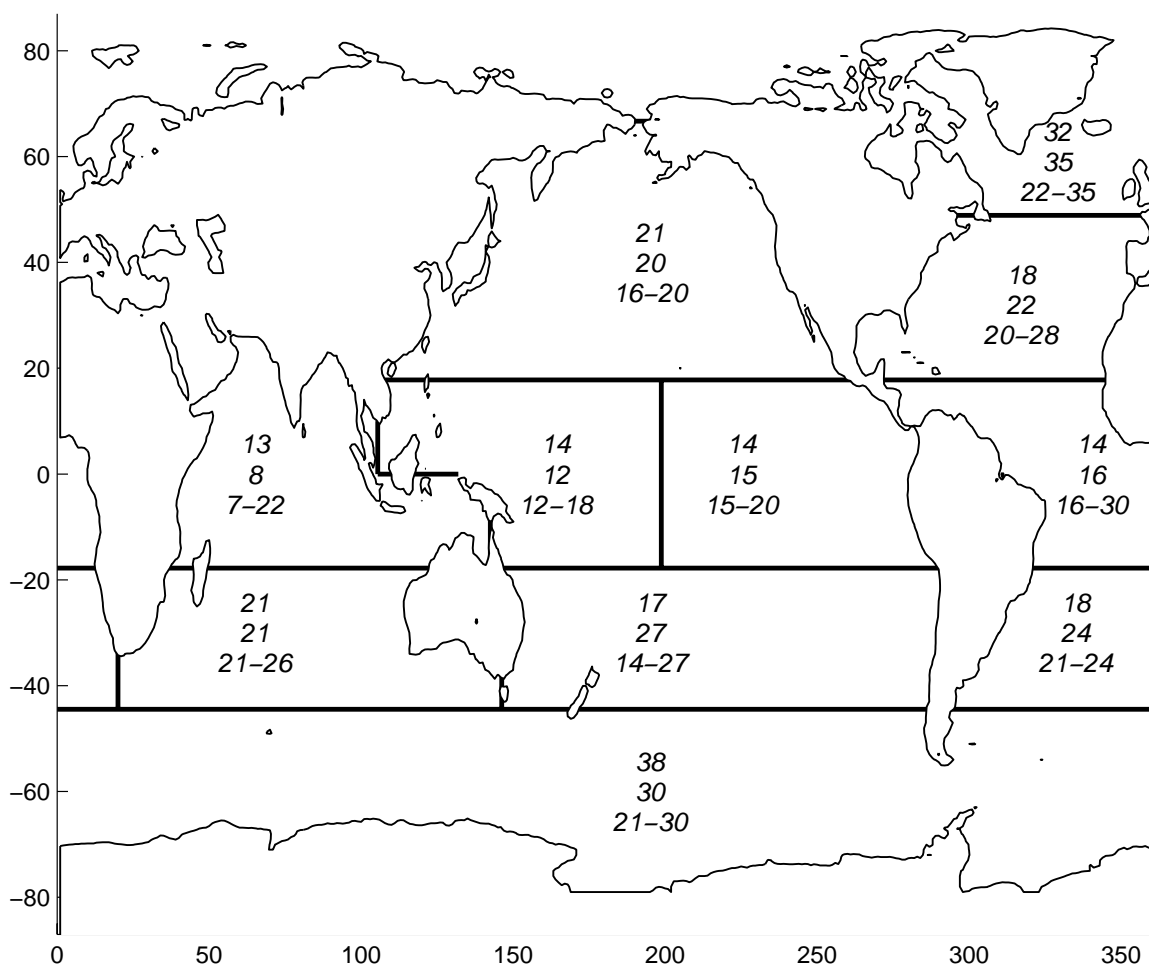
Figure 3.7. Mean air-sea gas transfer velocities over 11 regions (cm / hour), derived using the quadratic relationship with windspeed of *Wanninkhof* [1992; *Dutay et al.*, 2002] (top row in each region) and estimated by optimizing the fit to 1970s ocean bomb radiocarbon observations where potential alkalinity is used to determine the bomb component (second row); the third row gives a range of optimized fits obtained from variant optimizations that featured fitting integrated vertical profile amounts instead of individual measurements and/or using silicate instead of potential alkalinity or silicate measurements to help determine the bomb component. This range gives a better idea of the actual uncertainty in our results than the uncertainty obtained by assuming error in the measurements to be uncorrelated, which is around 1 cm / hour for each region.
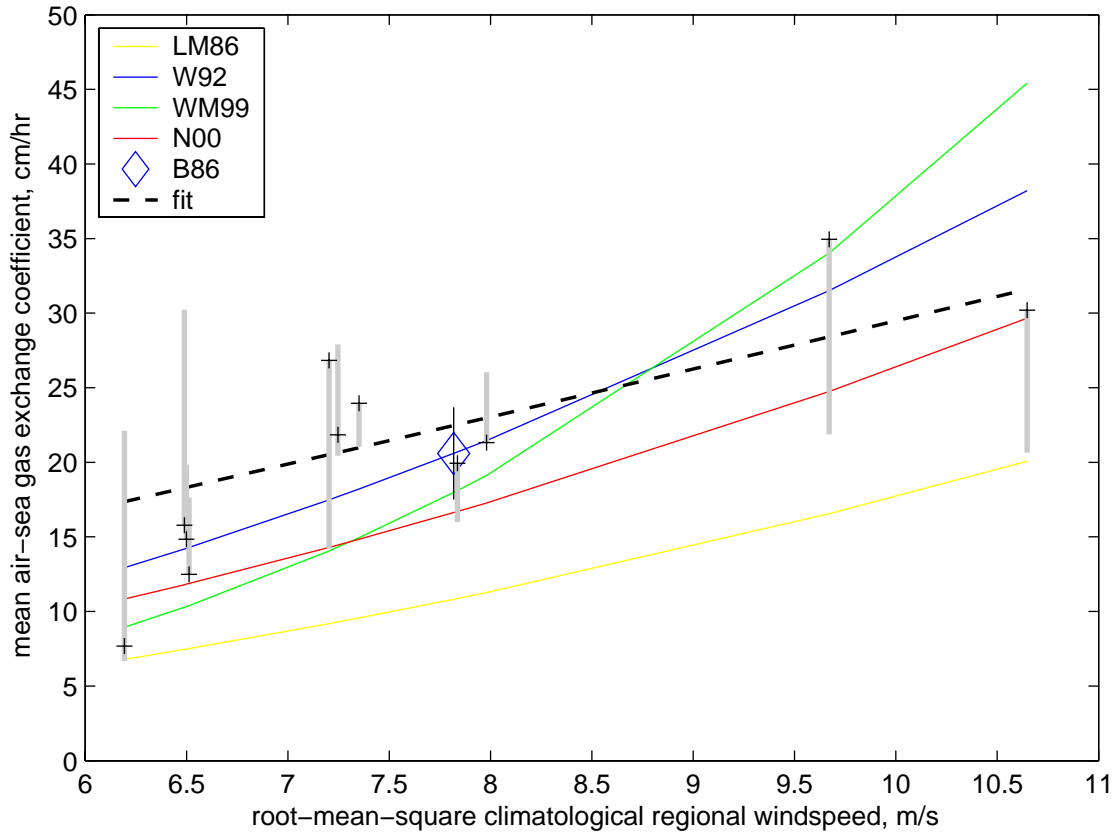
Figure 3.8. Regional air-sea gas transfer velocity estimated from optimizing the fit to ocean bomb carbon-14 measurements plotted against regional root mean square windspeed (crosses, with gray bars indicating the range from different optimization cases, which is taken to be the 1 standard deviation uncertainty range). Selected published formulations of air-sea gas exchange as a function of windspeed are shown for comparison: the piecewise linear relationship from *Liss and Merlivat* [1986] (here approximated as quadratic, following *Wanninkhof* [1992]); the quadratic relationship of *Wanninkhof* [1992]; the cubic relationship of *Wanninkhof and McGillis* [1999]; and the polynomial (quadratic and linear terms) relationship of *Nightingale et al.* [2000]. To graph these formulations, we calculated first and third moments of the windspeed distribution from the mean square (second moment) climatology assuming that windspeeds in each region followed a Rayleigh distribution. The diamond and error bar show, at the global root-mean-square windspeed, the global gas transfer velocity estimated from ocean radiocarbon evidence by *Broecker et al.* [1986]. The best-fit power law relationship to the regional windspeed is also drawn (dashed curve): it has an exponent of 1.11±0.37 and a global mean of 20.6±0.6 cm / hour.

(a) GEOSECS (1970s)

(b) WOCE (1990s)

Exponent of windspeed dependence
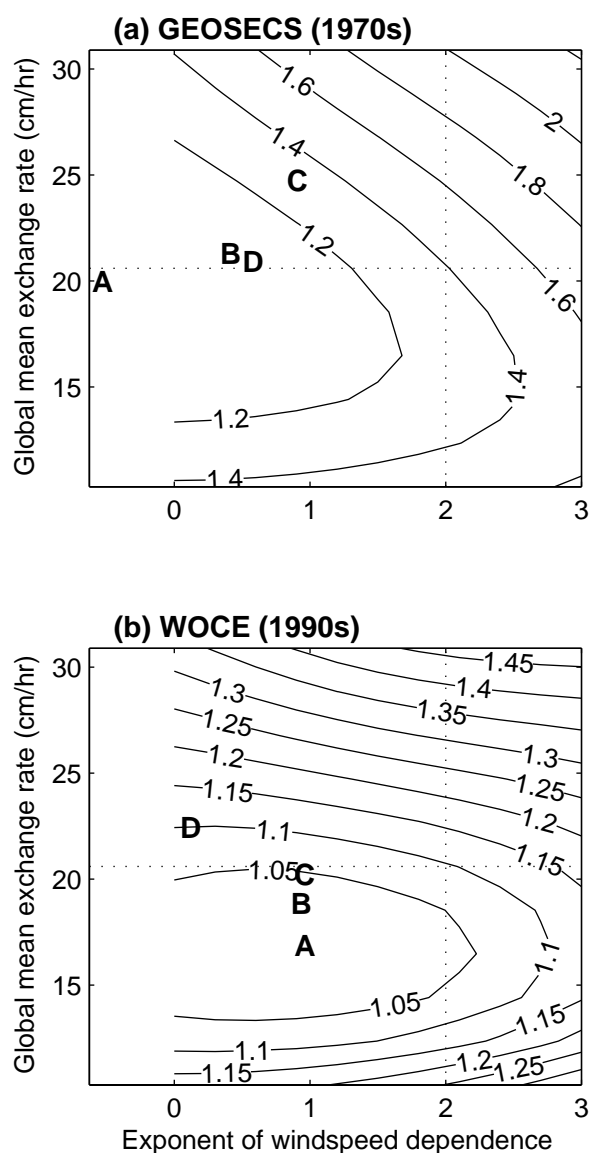
Figure 3.9. Minimizing the misfit of predicted vs. observed gas exchange as a function of the air-sea gas transfer velocity windspeed dependence exponent n and the global mean rate $\overline{k}$. (a) Misfit with GEOSECS (1970s) bomb radiocarbon observations; (b) misfit with WOCE (mostly 1990s) observations. The letters show the minimum-misfit point for different considered. The cases are: fit against individual measurements using either potential alkalinity (A) or silica (B) to estimate the background $\Delta^{14}C$; or fit against column amount computed from measured vertical profiles, again using potential alkalinity (C) or silica (D). The contour lines show the misfit function values, relative to their minima, for the case marked A. The dotted lines show the *Wanninkhof* [1992] values for the global mean gas transfer velocity and for the windspeed dependence exponent.
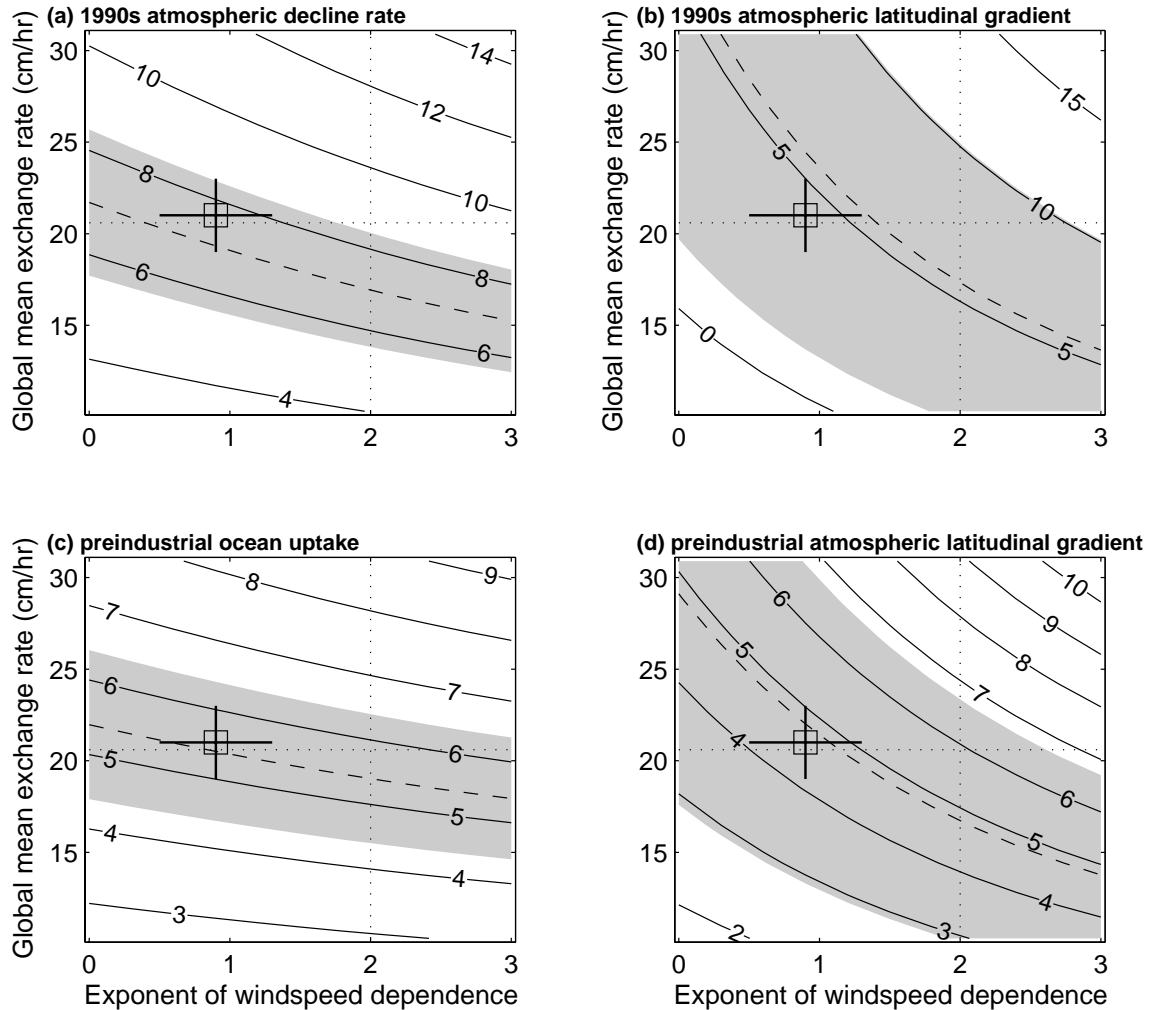
Figure 3.10. Effect of the air-sea gas exchange parameterization on predicted total ocean ^{14}C uptake and on latitudinal gradients in atmospheric Δ^{14}C. The dotted lines show the *Wanninkhof* [1992] values for the global mean gas transfer velocity and for the windspeed dependence exponent. The square and error bars mark the parameter values that we found to best fit ocean bomb radiocarbon measurements. The dashed lines show the approximate uptake or latitudinal gradients inferred from observations, and the shading shows the 1 standard deviation uncertainty range both by measurement error and by error in other components of the measured-modeled comparison, such as atmospheric transport. (a) Decline rate (in ‰ / year) of atmospheric Δ^{14}C around 1994, based on sea-surface Δ^{14}C interpolated from WOCE observations, atmospheric Δ^{14}C from atmospheric observations, and estimates of isotope fluxes due to biosphere exchange, cosmogenic ^{14}C production and fossil carbon emissions. Observations yield a decline rate of 7.0±1.4 ‰ / year. (b) Latitudinal gradient in mean-annual atmospheric Δ^{14}C (Llano de Hato, Venezuela [8°N] − Macquarie Island [54°S]) around 1994, based on sea-surface Δ^{14}C interpolated from WOCE observations, atmospheric Δ^{14}C from atmospheric observations, and estimates of isotope fluxes due to biosphere exchange, cosmogenic ^{14}C production, and fossil carbon emissions, calculated with the atmospheric transport model MATCH. Observations reported by *Levin and Hesshaimer* [2000] yield a difference of 5.6±4.5‰.

(c) Steady-state ocean ^{14}C uptake (in kg / year) assuming an estimated preindustrial sea-surface Δ^{14}C distribution and mean atmospheric Δ^{14}C at 0‰. For comparison, 5.4±1 kg / year would be needed to replace the decay of ^{14}C in the ocean DIC pool. (d) Steady-state latitudinal atmospheric Δ^{14}C gradient (Britain – New Zealand, in each hemisphere's summer; in permil) calculated with the atmospheric transport model MATCH, assuming an estimated preindustrial sea-surface Δ^{14}C distribution and mean atmospheric Δ^{14}C at 0‰. For comparison, preindustrial tree-ring measurements reported by *Hogg et al.* [2002] yield a difference of 4.8±1.6 ‰.
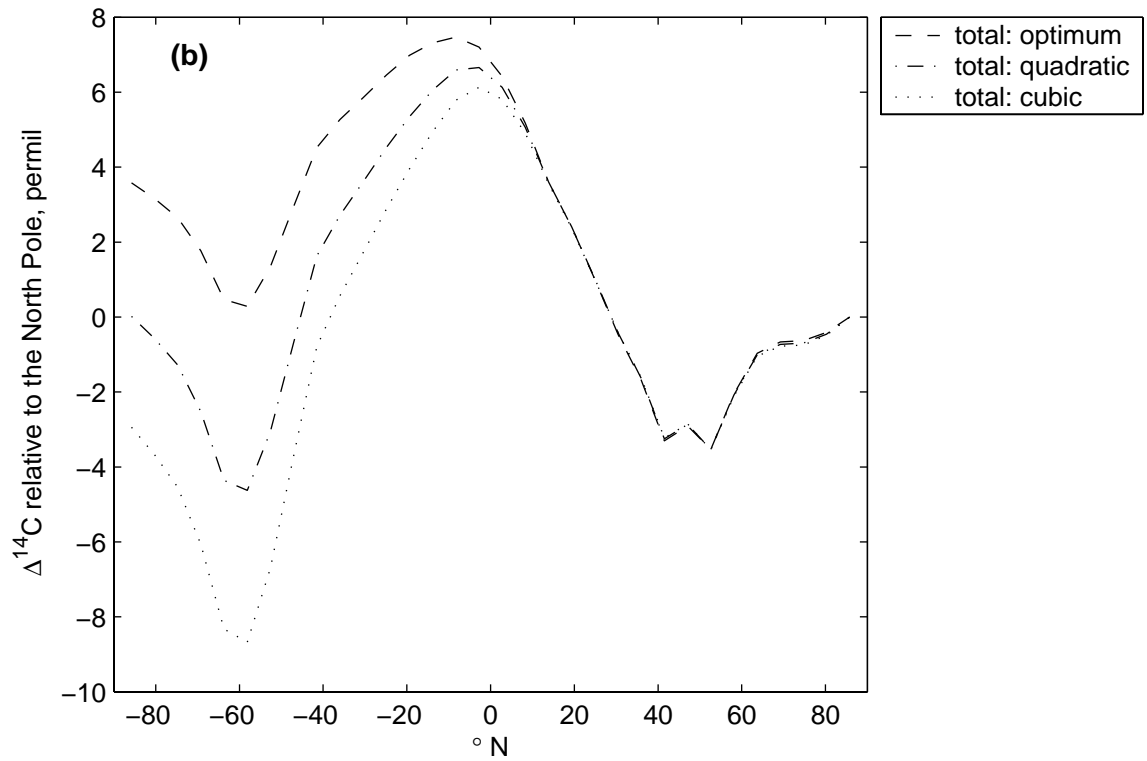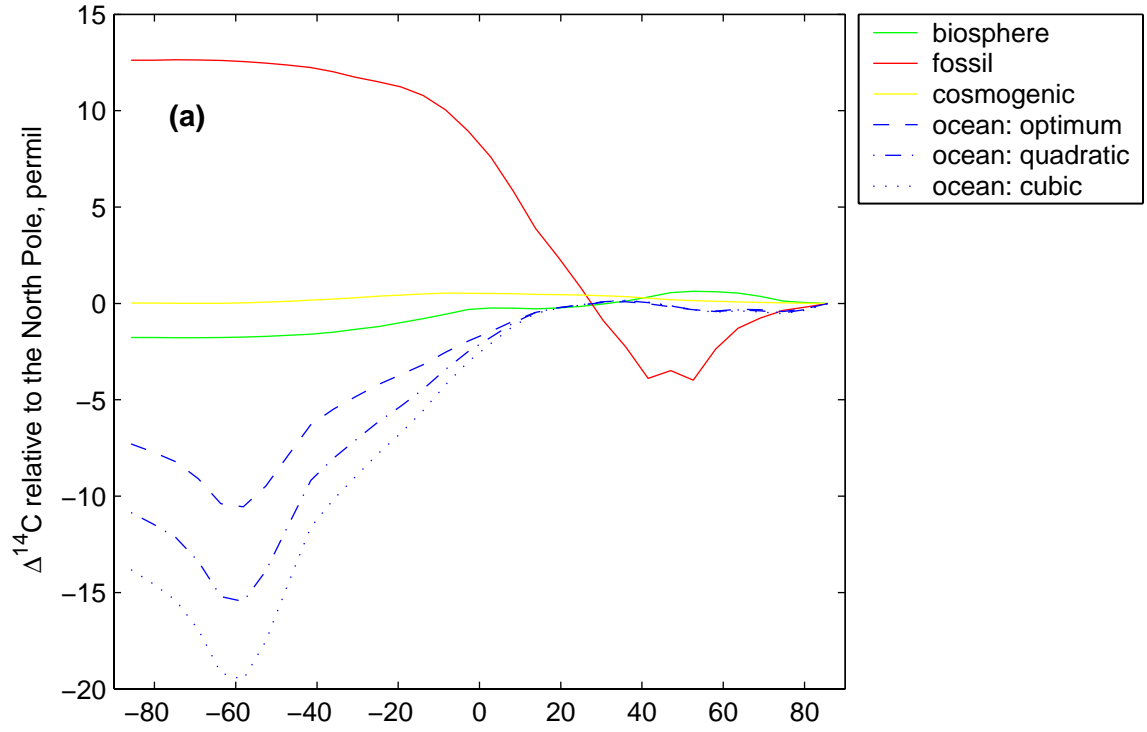
Figure 3.11. Predicted mean latitudinal gradient in $\Delta^{14}C$ of atmospheric CO_2 around 1994, taking into account the primary processes likely to cause spatial heterogeneities. We show the effect of modeled ocean uptake using measured sea-surface $\Delta^{14}C$ [*Key et al.*, 2004] and either our optimized parameterization of the increase of the gas transfer velocity with windspeed (close to linear, with an exponent n = 0.9) or quadratic or cubic parameterizations (n = 2 or 3). (a) Modeled contribution by process. Fossil fuel emissions, concentrated in the northern midlatitudes, dilute atmospheric ^{14}C, while respired CO_2 from the land biosphere contains high levels of bomb radiocarbon and leads to a smaller enhancement in $\Delta^{14}C$ over tropical forests and the northern midlatitudes. Exchange with ^{14}C-depleted carbon in the Southern Ocean reduces atmospheric $\Delta^{14}C$ in the southern midlatitudes, with the modeled magnitude of the depletion depending on the assumed dependence of the air-sea gas transfer velocity on windspeed. (b) Resultant modeled gradient. While the $\Delta^{14}C$ distribution in the northern hemisphere is unaffected by the assumed form of the air-sea gas transfer velocity, this form has a major influence on the $\Delta^{14}C$ distribution in the southern hemisphere.
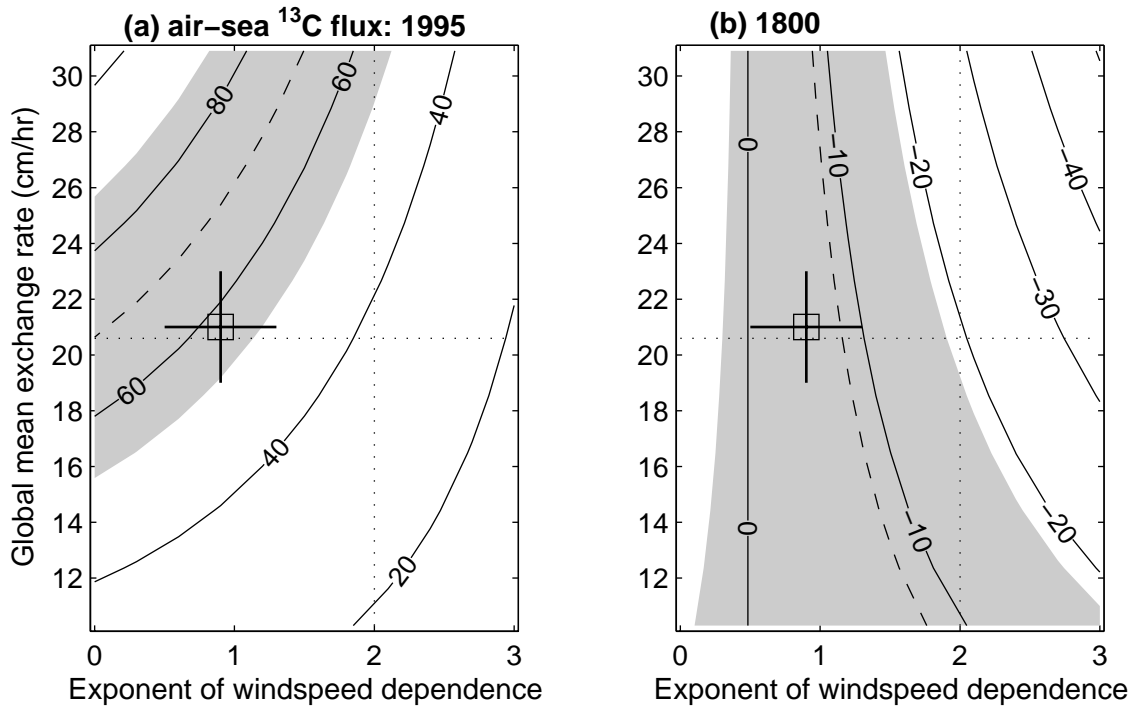
Figure 3.12. Effect of the air-sea gas exchange parameterization on the ^{13}C isotope flux into the ocean, in Pg C ‰ / year, derived from observations of sea-surface and atmosphere δ^{13}C, (a) for the mid-1990s and (b) preindustrially. The dashed line and shading in (a) shows the observation-based estimate (± 1 standard deviation) of 70±17 Pg C ‰ / year; the corresponding constraint for (b) is −8±10 Pg C ‰ / year. The dotted lines show the *Wanninkhof* [1992] values for the global mean gas transfer velocity and for the windspeed dependence exponent. The square and error bars mark the parameter values that we found to best fit ocean bomb radiocarbon measurements.
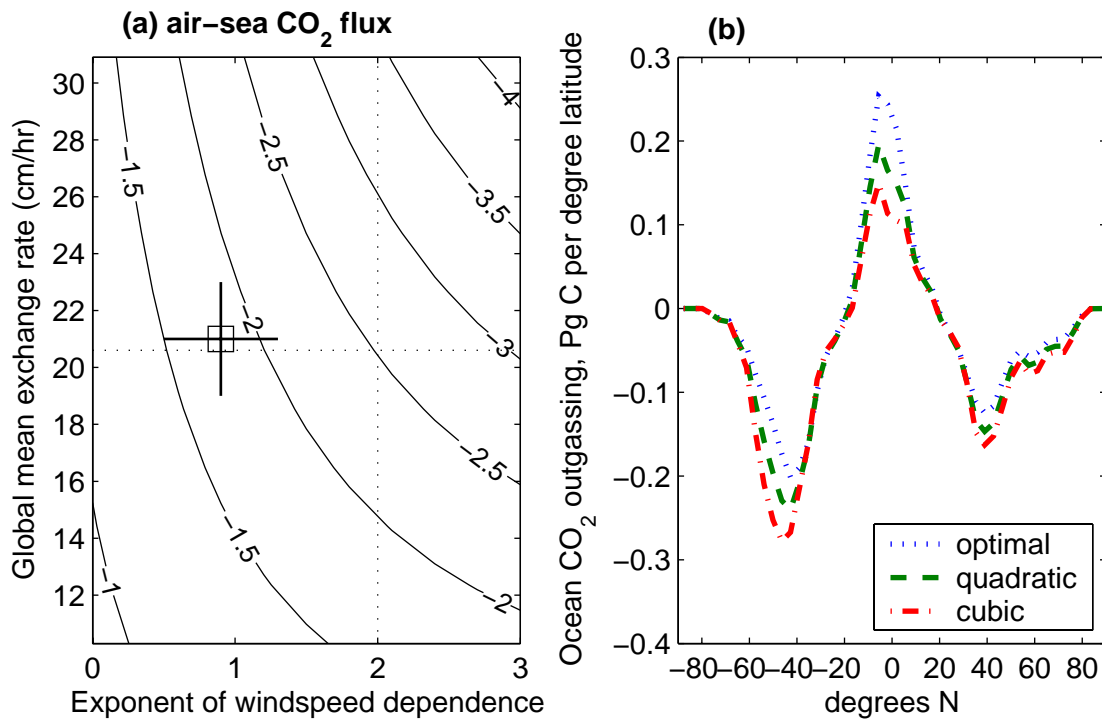
Figure 3.13. Effect of the air-sea gas transfer velocity parameterization on predicted air-sea flux of CO_2, based on the air-sea ΔpCO_2 climatology prepared by *Takahashi et al.* [2002] for 1995. (a) Predicted global ocean uptake of anthropogenic CO_2 (in Pg C / year) as a function of the air-sea gas exchange parameterization. To obtain the anthropogenic CO_2 flux, we corrected the total flux by 0.7 Pg C / year for the assumed steady-state ocean outgassing that balances an inflow of continental carbon [*Aumont et al.*, 2001]. The dashed lines show the *Wanninkhof* [1992] values for the global mean gas transfer velocity and for the windspeed dependence exponent. The square and error bars mark the parameter values that we found to best fit ocean bomb radiocarbon measurements. Observational estimates of this uptake have been around 2.0-2.4 Pg C / year. (b) Latitudinal distribution of the air-sea flux for our optimized parameter values and for parameterizations of air-sea gas exchange with quadratic or cubic dependences on windspeed.

Table 3.1. Rate of decline of atmospheric $\Delta^{14}C$ around 1994

Station	Latitude	$\Delta^{14}C$ of atmospheric CO_2 (‰)		rate of decline (‰ / year)
		1992.0[d]	1997.0[d]	
Schauinsland[a]	48°N	138	102	7.2
Jungfraujoch[a]	47°N	139	105	6.8
Pretoria[b]	26°S	148	117	6.3
Wellington[c]	41°S	153	114	7.7
Mean ± SD				7.0±0.6

a. *Levin and Kromer* [2004].
b. S. Woodbourne, personal communication, updating *Manning et al.* [1990].
c. G. Brailsford, personal communication, updating *Vogel* [1971].
d. For the northern hemisphere stations, calculated as the average of the preceding and subsequent summer (since atmospheric $\Delta^{14}C$ near the surface is more variable in winter than in summer).

Table 3.2. Modeled contributions of carbon fluxes to the rate of decline and latitudinal gradient in atmospheric Δ^{14}C around 1994

	Growth rate (‰ / year)	Latitudinal gradient[a] (‰)
Biosphere[b]	3.7±0.7	2.7±1.2
Fossil fuels[b]	−9.3±0.5	−7.8±1.6
Cosmogenic production[b]	6.2±0.6	0.5±0.6
Ocean		
Linear[c]	−8.2±0.6	8.9±2.6
Quadratic[c]	−9.3±0.7	12.2±3.4
Cubic[c]	−10.3±0.7	15.4±4.3
Model uncertainty[d]	±1.3	±3.5
Measured value	−7.0±0.6[e]	5.6±2.8[f]
Total uncertainty[g]	±1.4	±4.5

a.   Annual-mean Δ^{14}C at Llano de Hato, Venezuela (9°N), subtracted from that at Macquarie Island (54°S).
b.   Modeled effects (see Methods section); 1-SD uncertainties reflect approximate confidence in flux size, plus error in the atmospheric transport model (estimated from the spread in standardized regional pulse functions of models participating in the TransCom 3 intercomparison [*Gurney et al.*, 2003]) in the case of the latitudinal gradient.

c.   For air-sea gas transfer velocity formulations with the global mean rate the same as in the OCMIP formulation ($\bar{k}$ = 20.6 cm / hour in Equation 3) and a linear, quadratic, or cubic dependence on windspeed (n = 1, 2 or 3). The given uncertainties reflect confidence in the air-sea Δ^{14}C disequilibrium and in the transport model, assuming that the given formulation of gas exchange is correct.
d.   Overall uncertainty in the model prediction: sum of the uncertainties from the different components, assuming the quadratic dependence of air-sea gas exchange on windspeed for the ocean contribution.
e.   See Table 3.1.
f.   *Levin and Hesshaimer* [2000].
g.   Model plus measurement uncertainty contributions.

Table 3.3. Deriving the ^{13}C isotope flux out of the ocean around 1995 from the atmospheric ^{13}C budget

Observed or estimated quantities

Atmospheric CO_2	763.8[a]±3.2	Pg C
Fossil CO_2 emissions	6.4[b]±0.3	Pg C / year
Ocean anthropogenic CO_2 uptake	2.2[c]±0.3	Pg C / year
Atmospheric CO_2 rate of increase	3.2[d]±0.3	Pg C / year
Mean δ^{13}C of fossil emissions	−28.1±1	‰
Mean δ^{13}C of atmospheric CO_2	−7.91[e]±0.03	‰
Disequilibrium of terrestrial respiration	0.35[f]±0.1	‰
Terrestrial net primary productivity	55.4[f]±15	Pg C / year
Terrestrial photosynthesis ^{13}C discrimination	−19±1.5	‰
Rate of change in δ^{13}C of atmospheric CO_2	−0.018[e]±0.005	‰
River flow of terrestrial organic matter into ocean	0.4[g]±0.2	Pg C / year

Derived quantities

Land biosphere CO_2 uptake	1.0±0.5	Pg C / year

Atmospheric ^{13}C budget: Isotope fluxes

Fossil fuels	−128±9	Pg C ‰ / year
Land biosphere, from isotopic disequilibrium	19±8	Pg C ‰ / year
Land biosphere, from fractionation in net CO_2 uptake	18±10	Pg C ‰ / year
Storage in atmosphere (change in δ^{13}C)	−14±4	Pg C ‰ / year
Inferred disequilibrium isotope flux from ocean	77±16	Pg C ‰ / year
Sea-air isotope flux to balance river flow at steady state	−8±4	Pg C ‰ / year
Inferred total air-sea isotope flux	70±17	Pg C ‰ / year

Adopted values and 1-SD uncertainties were mostly based on those used in the similar calculations by *Heimann and Maier-Reimer* [1996] and *Gruber and Keeling* [2001], except as specified below.
a. From 1995 means of NOAA-CMDL flask measurements [*Conway et al.*, 1994] for remote stations, binned by latitude and averaged.
b. *Marland et al.* [2005]
c. *Mikaloff Fletcher et al* [in press]
d. Change over the 1990s in NOAA-CMDL flask measurements [*Conway et al.*, 1994] for remote stations, binned by latitude and averaged.
e. 1995 means and change over the 1990s in measurements from the CSIRO [*Francey et al.*, 2001] and Scripps [*Keeling et al.*, 1995] station networks, binned by latitude and averaged

f. CASA [*Potter et al.*, 1993] plant and soil carbon model; the disequilibrium was derived by weighting respiration pulse functions from CASA [*Thompson and Randerson*, 1999] with a time series of change in atmospheric $\delta^{13}C$ [*Francey et al.*, 1999].

g. *Aumont et al.* [2001]; we assumed this flux to have the same $\delta^{13}C$ as mean terrestrial photosynthesis

Table 3.4. Summary of ^{14}C and ^{13}C constraints on the global mean air-sea gas transfer velocity $\bar{k}$ and its windspeed dependence exponent n

Constraint	Implied $\bar{k}$ (cm / hour)	Implied n
Ocean bomb ^{14}C measurements		
Ocean total amount (WOCE)	15-31	
Fit of regional gas transfer velocities	20.6±0.6	1.11±0.37
Fit of $\bar{k}$, n directly	20.7±2.4	0.61±0.40
Overall	**21±2**	**0.9±0.4**
Other ^{14}C and ^{13}C measurements[*]		
Atmospheric $\Delta^{14}C$: 1990s decline rate	19±4	0.3 (0-1.6)
Atmospheric $\Delta^{14}C$: 1990s latitudinal gradient	24±11	1.3 (0-2.7)
Preindustrial ocean ^{14}C uptake	21±4	
Preindustrial atmospheric $\Delta^{14}C$ latitudinal gradient	22±9	1.1 (0-2.5)
Air-sea ^{13}C isotope flux, 1990s	25±6	0.1 (0-1.2)
Air-sea ^{13}C isotope flux, preindustrial		1.1 (0.3-1.9)

The ranges or 1-σ uncertainties given for the implied values of $\bar{k}$ and n are based on our estimates of measurement and model uncertainties, and/or on the spread between fits using different assumptions; see text for details.

[*] These measurements typically imply a range of compatible ($\bar{k}$, n) pairs (shown as the area shaded gray in Figure 3.10 and 12). The implied values given here are the compatible values of $\bar{k}$ or n if the other parameter is set to the best-fit value determined from the ocean bomb radiocarbon distribution (i.e. n = 0.9 or $\bar{k}$ = 21 cm / hour), which independently constrains both parameters. We left cells blank if the measurement does not meaningfully constrain $\bar{k}$ or n within the range of $\bar{k}$ = 10-31 cm / hour and n = 0-3.

Appendix: Terms in the Budget of $^{13}CO_2$ in the Atmosphere

3.A.1 Concepts

We begin with the number ratio ^{13}R of $^{13}C/^{12}C$ atoms:

$$^{13}R \equiv {}^{13}C / {}^{12}C, \qquad (1)$$

where we use ^{13}C and ^{12}C to refer to the number of atoms (or moles) of each isotope in a particular reservoir. The number of other, unstable carbon isotopes is normally negligible ($\sim 10^{-12}$ of the total), so for our purposes an excellent approximation is

$$C = {}^{13}C + {}^{12}C = (1 + {}^{13}R) \cdot {}^{12}C, \qquad (2)$$

where C is the total number of carbon atoms (or moles) in the reservoir.

The $^{13}C/^{12}C$ ratio is generally measured relative to the ratio in a reference material, and so is conveniently expressed in δ notation:

$$\delta^{13}C \equiv ({}^{13}R/{}^{13}R_0) - 1, \qquad (3)$$

where $^{13}R_0$ for the commonly accepted VPDB standard is 0.0112 [*Coplen et al.*, 2002]. Below, we will abbreviate $\delta^{13}C$ to δ and ^{13}R to R.

In interpreting change in reservoir $\delta^{13}C$, it is useful to separate changes in reservoir ^{12}C and ^{13}C content into a change in total carbon C at constant $\delta^{13}C$ and a change in $\delta^{13}C$ at constant C. The flux required to cause the latter is termed "isotope flux" or "isoflux" [e.g. *Battle et al.*, 2000], which we can define as

$$^{13}F \equiv C \cdot (\delta^{13}C)' = (C/^{13}R_0) \cdot (^{13}R)', \quad (4)$$

where the prime $'$ denotes the derivative with respect to time. Expressing the amount of carbon C as a mass, the isotope flux commonly has units of Pg C $\cdot$ ‰ / year.

We now consider the carbon flux and ^{13}C isotope flux into a reservoir such as the atmosphere where the carbon flux can be separated into component fluxes F_i with distinct isotope ratios $^{13}R_i$ or δ_i. We have for the carbon flux

$$C' = \sum_i F_i \qquad (5)$$

and by (1) and (2)

$$(^{13}C)' = \sum_i (R_i/(1 + R_i)) \cdot F_i \qquad (6)$$

and

$$(^{12}C)' = \sum_i (1/(1 + R_i)) \cdot F_i, \qquad (7)$$

so that by (3) and (4)

$$^{13}F = \sum_i \left(1 + \frac{(\delta - \delta_i)R_0}{1 + (\delta_i + 1)R_0}\right)(\delta_i - \delta)F_i . \qquad (8)$$

As expected, no isotopic flux results from any carbon flux with the same isotopic composition as that of the reservoir, because then δ_i is equal to δ.

Since in the large-scale CO_2 fluxes of interest here the difference in isotopic composition $|\delta - \delta_i|$ is generally less than 30‰ while R_0 is about 10^{-2}, the term

$\dfrac{(\delta - \delta_i)R_0}{1 + (\delta_i + 1)R_0}$ in (8) is at most of order $3 \cdot 10^{-4}$, so that

$$^{13}F \approx \sum_i (\delta_i - \delta) \cdot F_i. \qquad (9)$$

For simplicity we will use the expression (9) in the following sections, although the exact form (8) could be straightforwardly substituted.

A final needed result: if a flux F_i has an isotopic fractionation α_i operating, so that

$$R_i = \alpha_i \cdot \overline{R}_i , \qquad (10)$$

where $\overline{R}_i$ is the bulk isotopic composition of the source reservoir, then by (3),

$$\delta_i = \alpha_i \cdot \overline{\delta_i} + (\alpha_i - 1). \qquad (11)$$

3.A.2 Application to the atmospheric budget

Based on the above, we can formulate equations for the isotope flux into the atmosphere over timescales of a few years. The major fluxes are due to fossil-fuel burning, air-sea exchange, and air-biosphere exchange, so that

$$F = \sum_i F_i \approx (F_f + F_o + F_b), \qquad (12)$$

where the subscripts f, o, and b refer to the fossil, ocean and biosphere fluxes respectively.

3.A2.1 Fossil fuel burning

Applying (9),

$$^{13}F_f = (\delta_f - \delta) \cdot F_f, \qquad (13)$$

where F_f is the fossil carbon flux, δ_f is its (mean) isotopic composition, and δ is the atmospheric composition.

3.A.2.2 Air-sea exchange

The air-sea exchange is the sum of fluxes in and out of the ocean, so that the carbon flux into the atmosphere at a given spot is given by

$$F_o = k_w \cdot A \cdot (P_o - P_a), \qquad (14)$$

where k_w is a gas transfer velocity, A is the solubility of CO_2 in seawater, P_o is the CO_2 partial pressure at equilibrium with the ocean water, and P_a is the air CO_2 partial pressure. By (9), the isotopic flux is then given by

$$^{13}F_o = k_w \cdot A \cdot [(\delta_{oa} - \delta)P_o - (\delta_{ao} - \delta)P_a], \qquad (15)$$

where δ_{oa} and δ_{ao} are the isotopic compositions of the sea-to-air and air-to-sea fluxes respectively. If the respective fractionations against ^{13}C are given by the fractionation factors α_{oa} and α_{ao}, substituting in (11) yields

$$^{13}F_o = (k_w A/R_0) \cdot [(\alpha_{oa}R_o - R)P_o - (\alpha_{ao}R_a - R)P_a]. \qquad (16)$$

Here R_a is the local atmospheric isotope ratio, which may be different from the overall atmospheric value R.

3.A.2.3 Air-biosphere exchange

The air-biosphere flux is also the sum of a photosynthetic flux out of the atmosphere and a "respiration" (actually including inorganic oxidation, such as fire) flux into the atmosphere. Thus

$$F_b = F_{ba} - F_{ab}. \qquad (17)$$

If the photosynthetic fractionation is α_{ab} and oxidation does not fractionate carbon isotopes ($\alpha_{ba} = 1$), the corresponding isotope flux is

$$^{13}F_b = (\delta_b - \delta)F_{ba} - (\alpha_{ab}\delta_a + (\alpha_{ab} - 1) - \delta) \, F_{ab}. \qquad (18)$$

If we assume that photosynthesis and "respiration" rates, averaged over a suitable time and space domain, are equal, then (18) simplifies to

$$^{13}F_b = (\delta_b - \alpha_{ab}\delta_a + (\alpha_{ab} - 1)) \, F_{ab}. \qquad (19)$$

Assuming also that the fractionation factor α_{ab} is constant with time, the biospheric composition δ_b, and hence the isotopic flux $^{13}F_b$ can be calculated from the local atmospheric history $\delta_a(t)$ if we postulate a Green's function $G(\tau)$ that is constant in time and describes the oxidation rate of a unit amount of fixed carbon as a function of the time since the carbon was fixed. Then we have

$$^{13}F_b(t) = \alpha_{ab} \cdot F_{ab} \cdot \int_{\tau=0}^{\infty} [\delta_a(t - \tau) - \delta_a(t)]G(\tau)d\tau . \qquad (20)$$

The reasonable assumption that the long-term trend in local atmospheric $\delta^{13}C$ is similar to the trend in overall atmospheric $\delta^{13}C$ allows substituting $\delta(t)$ for $\delta_a(t)$ in (20).

References

Adams, J. M. and G. Piovesan (2005), Long series relationships between global interannual CO_2 increment and climate: Evidence for stability and change in role of the tropical and boreal-temperate zones, *Chemosphere*, *59*(11), 1595-1612.

Alley, R. B., C. A. Shuman, D. A. Meese, et al. (1997), Visual-stratigraphic dating of the GISP2 ice core: Basis, reproducibility, and application, *J. Geophys. Res.*, *102*(C12), 26367-26381.

Andres, R. J., G. Marland, I. Fung, et al. (1996), A 1°×1° distribution of carbon dioxide emissions from fossil fuel consumption and cement manufacture, 1950-1990, *Global Biogeochem. Cycles*, *10*(3), 419-429.

Angert, A., S. Biraud, C. Bonfils, et al. (2004), CO_2 seasonality indicates origins of post-Pinatubo sink, *Geophys. Res. Lett.*, *31*(11).

Asher, W., Q. Wang, E. C. Monahan, et al. (1998), Estimation of air-sea gas transfer velocities from apparent microwave brightness temperature, *Marine Tech. Soc. J.*, *32*(2), 32-40.

Aster, R. C., B. Borchers and C. H. Thurber (2005), *Parameter Estimation and Inverse Problems*, 301 pp., Elsevier Academic Press.

Aumont, O., J. C. Orr, P. Monfray, et al. (2001), Riverine-driven interhemispheric transport of carbon, *Global Biogeochem. Cycles*, *15*(2), 393-405.

Bacastow, R. B., C. D. Keeling, T. J. Lueker, et al. (1996), The C-13 Suess effect in the world surface oceans and its implications for oceanic uptake of CO_2: Analysis of observations at Bermuda, *Global Biogeochem. Cycles*, *10*(2), 335-346.

Baillie, M. G. L. and M. A. R. Munro (1988), Irish tree rings, Santorini and volcanic dust veils, *Nature*, *332*, 344-346.

Bakwin, P. S., P. P. Tans, C. L. Zhao, et al. (1995), Measurements of carbon-dioxide on a very tall tower, *Tellus*, *47*(B5), 535-549.

Barber, V. A., G. P. Juday and B. P. Finney (2000), Reduced growth of Alaskan white spruce in the twentieth century from temperature-induced drought stress, *Nature*, *405*(6787), 668-673.

Bates, N. R. (2002), Interannual variability in the global uptake of CO_2, *Geophys. Res. Lett.*, *29*(5).

Battle, M., M. L. Bender, P. P. Tans, et al. (2000), Global carbon sinks and their variability inferred from atmospheric O_2 and delta ^{13}C, *Science*, *287*(5462), 2467-2470.

Bert, D., S. W. Leavitt and J. L. Dupouey (1997), Variations of wood delta ^{13}C and water-use efficiency of *Abies alba* during the last century, *Ecology*, *78*(5), 1588-1596.

Bousquet, P., P. Ciais, P. Peylin, et al. (1999a), Inverse modeling of annual atmospheric CO_2 sources and sinks 1. Method and control inversion, *J. Geophys. Res.*, *104*(D21), 26161-26178.

Bousquet, P., P. Peylin, P. Ciais, et al. (2000), Regional changes in carbon dioxide fluxes of land and oceans since 1980, *Science*, *290*(5495), 1342-1346.

Bousquet, P., P. Peylin, P. Ciais, et al. (1999b), Inverse modeling of annual atmospheric CO_2 sources and sinks 2. Sensitivity study, *J. Geophys. Res.*, *104*(D21), 26179-26193.

Boutin, J. and J. Etcheto (1996), Consistency of Geosat, SSM/I, and ERS-1 global surface wind speeds - Comparison with in situ data, *Journal of Atmospheric and Oceanic Technology*, *13*(1), 183-197.

Boutin, J. and J. Etcheto (1997), Long-term variability of the air-sea CO_2 exchange coefficient: Consequences for the CO_2 fluxes in the equatorial Pacific ocean, *Global Biogeochem. Cycles*, *11*(3), 453-470.

Boyer, T. P., C. Stephens, J. I. Antonov, et al. (2002), *World Ocean Atlas 2001, Volume 2: Salinity*, 165 pp., US Government Printing Office, Washington.

Bradley, R. S. and P. D. Jones (1995), Records of explosive volcanic eruptions over the last 500 years, in *Climate Since A.D. 1500*, edited by R. S. Bradley and P. D. Jones, pp. 606-622, Routledge, London.

Braswell, B. H., D. S. Schimel, E. Linder, et al. (1997), The response of global terrestrial ecosystems to interannual temperature variability, *Science*, *278*(5339), 870-872.

Braziunas, T. F., I. Y. Fung and M. Stuiver (1995), The preindustrial atmospheric $^{14}CO_2$ latitudinal gradient as related to exchanges among atmospheric, oceanic, and terrestrial reservoirs, *Global Biogeochem. Cycles*, *9*(4), 565-584.

Briffa, K., P. Jones, F. Schweingruber, et al. (1998), Influence of volcanic eruptions on Northern Hemisphere summer temperature over the past 600 years, *Nature*, *393*(6684), 450-455.

Briffa, K. R., T. J. Osborn, F. H. Schweingruber, et al. (2001), Low-frequency temperature variations from a northern tree ring density network, *J. Geophys. Res.*, *106*(D3), 2929-2941.

Briffa, K. R., T. J. Osborn, F. H. Schweingruber, et al. (2002), Tree-ring width and density data around the Northern Hemisphere: Part 1, local and regional climate signals, *Holocene*, *12*(6), 737-757.

Broecker, W., R. Gerard, M. Ewing, et al. (1960), Natural radiocarbon in the Atlantic Ocean, *J. Geophys. Res.*, *65*(9), 2903-2931.

Broecker, W. S., J. R. Ledwell, T. Takahashi, et al. (1986), Isotopic versus micrometeorological ocean CO_2 fluxes - a serious conflict, *J. Geophys. Res.*, *91*(C9), 517-527.

Broecker, W. S. and T.-H. Peng (1982), *Tracers in the sea*, 690 pp., Lamont-Doherty Geological Observatory, Palisades, NY.

Broecker, W. S., T. H. Peng, G. Ostlund, et al. (1985), The distribution of bomb radiocarbon in the ocean, *J. Geophys. Res.*, *90*(C4), 6953-6970.

Broecker, W. S., S. Sutherland, W. Smethie, et al. (1995), Oceanic radiocarbon - Separation of the natural and bomb components, *Global Biogeochem. Cycles*, *9*(2), 263-288.

Caldeira, K., G. H. Rau and P. B. Duffy (1998), Predicted net efflux of radiocarbon from the ocean and increase in atmospheric radiocarbon content, *Geophys. Res. Lett.*, *25*(20), 3811-3814.

Caldeira, K. and M. E. Wickett (2003), Anthropogenic carbon and ocean pH, *Nature*, *425*(6956), 365-365.

Ciais, P., P. P. Tans, M. Trolier, et al. (1995), A large northern-hemisphere terrestrial CO_2 sink indicated by the C-13/C-12 ratio of atmospheric CO_2, *Science*, *269*(5227), 1098-1102.

Cohan, D. S., J. Xu, R. Greenwald, et al. (2002), Impact of atmospheric aerosol light scattering and absorption on terrestrial net primary productivity, *Global Biogeochem. Cycles*, *16*(4), 1090 doi:10.1029/2001GB001441.

Colenutt, M. E. and B. H. Luckman (1996), Dendroclimatic characteristics of Alpine larch (*Larix lyalli* Parl.) at treeline sites in western Canada, in *Tree Rings, Environment and Humanity: Proceedings of the International Conference, Tucson, Arizona, 17-21 May 1994*, edited by J. S. Dean, et al., pp. 143-154, Radiocarbon, Dept. of Geosciences, University of Arizona, Tucson.

Contributors (2003), IGBP PAGES/World Data Center for Paleoclimatology (http://www.ngdc.noaa.gov/paleo/treering.html), NOAA/NGDC Paleoclimatology Program, Boulder.

Conway, T. J., P. P. Tans, L. S. Waterman, et al. (1994), Evidence for interannual variability of the carbon cycle from National Oceanic and Atmospheric Administration/Climate Monitoring and Diagnostics Laboratory Global Air Sampling Network, *J. Geophys. Res.*, *99*(D11), 23831-23855.

Coplen, T. B., J. K. Bohlke, P. De Bievre, et al. (2002), Isotope-abundance variations of selected elements - (IUPAC Technical Report), *Pure and Applied Chemistry*, *74*(10), 1987-2017.

Craig, H. (1957), The natural distribution of radiocarbon and the exchange time of carbon dioxide between the atmosphere and the sea, *Tellus*, *9*, 1-17.

Crowley, T. J. (2000), Causes of climate change over the past 1000 years, *Science*, *289*(5477), 270-277.

Crowley, T. J., T. M. Quinn, F. W. Taylor, et al. (1997), Evidence for a volcanic cooling signal in a 335-year coral record from New Caledonia, *Paleoceanography*, *12*(5), 633-639.

Damon, P. E. and R. E. Sternberg (1989), Global production and decay of radiocarbon, *Radiocarbon*, *31*(3), 697-703.

D'Arrigo, R. D. and G. C. Jacoby (1999), Northern North American tree-ring evidence for regional temperature changes after major volcanic events, *Climatic Change*, *41*(1), 1-15.

Ditmar, P., J. Kusche and R. Klees (2003), Computation of spherical harmonic coefficients from gravity gradiometry data to be acquired by the GOCE satellite: regularization issues, *J. Geodesy*, *77*(7-8), 465-477.

Donelan, M. A., B. K. Haus, N. Reul, et al. (2004), On the limiting aerodynamic roughness of the ocean in very strong winds, *Geophys. Res. Lett.*, *31*(18).

Druffel, E. M. and H. E. Suess (1983), On the radiocarbon record in banded corals: Exchange parameters and net transport of $^{14}CO_2$ between atmosphere and surface ocean, *Journal of Geophysical Research-Oceans and Atmospheres*, *88*(NC2), 1271-1280.

Druffel, E. R. M. (1987), Bomb radiocarbon in the Pacific: Annual and seasonal timescale variations, *J. Mar. Res.*, *45*, 667-698.

Druffel, E. R. M. (1989), Decade time scale variability of ventilation in the North Atlantic: High-precision measurements of bomb radiocarbon in banded corals, *J. Geophys. Res.*, *94*(C3), 3271-3285.

Druffel, E. R. M. and S. Griffin (1995), Regional variability of surface ocean radiocarbon from southern great barrier reef corals, *Radiocarbon*, *37*(2), 517-524.

Dutay, J. C., J. L. Bullister, S. C. Doney, et al. (2002), Evaluation of ocean model ventilation with CFC-11: comparison of 13 global ocean models, *Ocean Modelling*, *4*(2), 89-120.

England, M. H., V. Garcon and J. F. Minster (1994), Chlorofluorocarbon uptake in a world ocean model 1. Sensitivity to the surface gas forcing, *J. Geophys. Res.*, *99*(C12), 25215-25233.

Enting, I. G. (2002), *Inverse Problems in Atmospheric Constituent Transport*, 392 pp., Cambridge University Press, Cambridge, New York.

Esbensen, S. K. and Y. Kushnir (1981), The Heat Budget of the Global Ocean: An Atlas Based on Estimates from Marine Surface Observations, Oregon State University, Corvallis.

Fairall, C. W., J. E. Hare, J. B. Edson, et al. (2000), Parameterization and micrometeorological measurement of air-sea gas transfer, *Boundary-Layer Meteorology*, *96*(1-2), 63-105.

Fan, S., M. Gloor, J. Mahlman, et al. (1998), A large terrestrial carbon sink in North America implied by atmospheric and oceanic carbon dioxide data and models, *Science*, *282*(5388), 442-446.

Fasham, M. J. R. (2003), *Ocean biogeochemistry : the role of the ocean carbon cycle in global change*, 297 pp., Springer, Berlin; New York.

Feely, R. A., C. L. Sabine, K. Lee, et al. (2004a), Impact of anthropogenic CO_2 on the $CaCO_3$ system in the oceans, *Science, 305*(5682), 362-366.

Feely, R. A., R. Wanninkhof, W. McGillis, et al. (2004b), Effects of wind speed and gas exchange parameterizations on the air-sea CO_2 fluxes in the equatorial Pacific Ocean, *J. Geophys. Res.*, *109*(C8).

Feely, R. A., R. Wanninkhof, T. Takahashi, et al. (1999), Influence of El Niño on the equatorial Pacific contribution to atmospheric CO_2 accumulation, *Nature*, *398*(6728), 597-601.

Francey, R. J., C. E. Allison, D. M. Etheridge, et al. (1999), A 1000-year high precision record of $\delta^{13}C$ in atmospheric CO_2, *Tellus*, *51*(2), 170-193.

Francey, R. J., C. E. Allison, C. M. Trudinger, et al. (2001), The interannual variation in global atmospheric delta^{13}C and its link to net terrestrial exchange, in *Sixth International Carbon Dioxide Conference, Extended Abstracts*, pp. 43-46, Organizing Committee of Sixth International Carbon Dioxide Conference, Sendai, Japan.

Frank, N., M. Paterne, L. Ayliffe, et al. (2004), Eastern North Atlantic deep-sea corals: tracing upper intermediate water Delta C-14 during the Holocene, *Earth Planet. Sci. Lett.*, *219*(3-4), 297-309.

Frew, N. M., E. J. Bock, U. Schimpf, et al. (2004), Air-sea gas transfer: Its dependence on wind stress, small-scale roughness, and surface films, *J. Geophys. Res.*, *109*(C8).

Fritts, H. C. (1976), *Tree rings and climate*, 579 pp., Academic Press, London and New York.

Frost, T. and R. C. Upstill-Goddard (1999), Air-sea gas exchange into the millennium: Progress and uncertainties, in *Oceanography and Marine Biology, Vol 37*, pp. 1-45.

Gao, F. (1994), Fitting smoothing splines to data from multiple sources, *Commun. Stat.-Theory Methods*, *23*(6), 1665-1698.

Garabetian, F. (1991), ^{14}C-glucose uptake and ^{14}C-CO_2 production in surface microlayer and surface-water samples: influence of UV and visible radiation, *Marine Ecology-Progress Series*, *77*(1), 21-26.

Gervais, B. R. and G. M. MacDonald (2001), Tree-ring and summer-temperature response to volcanic aerosol forcing at the northern tree-line, Kola Peninsula, Russia, *Holocene*, *11*(4), 499-505.

Gloor, M., N. Gruber, T. M. C. Hughes, et al. (2001), Estimating net air-sea fluxes from ocean bulk data: Methodology and application to the heat cycle, *Global Biogeochem. Cycles*, *15*(4), 767-782.

Gloor, M., N. Gruber, J. Sarmiento, et al. (2003), A first estimate of present and preindustrial air-sea CO_2 flux patterns based on ocean interior carbon measurements and models, *Geophys. Res. Lett.*, *30*(1), 1010.

Goldstein, S. J., D. W. Lea, S. Chakraborty, et al. (2001), Uranium-series and radiocarbon geochronology of deep-sea corals: implications for Southern Ocean ventilation rates and the oceanic carbon cycle, *Earth Planet. Sci. Lett.*, *193*(1-2), 167-182.

Golub, G. H., P. C. Hansen and D. P. O'Leary (1999), Tikhonov regularization and total least squares, *SIAM J. Matrix Anal. Appl.*, *21*(1), 185-194.

Golub, G. H., M. Heath and G. Wahba (1979), Generalized cross-validation as a method for choosing a good ridge parameter, *Technometrics*, *21*(2), 215-223.

Goslar, T. (2001), Absolute production of radiocarbon and the long-term trend of atmospheric radiocarbon, *Radiocarbon*, *43*(2B), 743-749.

Gower, S. T., K. A. Vogt and C. C. Grier (1992), Carbon Dynamics of Rocky-Mountain Douglas-Fir - Influence of Water and Nutrient Availability, *Ecological Monographs*, *62*(1), 43-65.

Graumlich, L. J., L. B. Brubaker and C. C. Grier (1989), Long-term trends in forest net primary productivity - Cascade Mountains, Washington, *Ecology*, *70*(2), 405-410.

Grier, C. C. and R. S. Logan (1977), Old-growth *Pseudotsuga menziesii* communities of a western Oregon watershed: Biomass distribution and production budgets, *Ecological Monographs*, *47*(4), 373-400.

Groisman, P. Y. (1992), Possible climate consequences of the Pinatubo eruption: An empirical approach, *Geophys. Res. Lett.*, *19*(15), 1603-1606.

Gruber, N., M. Gloor, S. M. Fan, et al. (2001), Air-sea flux of oxygen estimated from bulk data: Implications for the marine and atmospheric oxygen cycles, *Global Biogeochem. Cycles*, *15*(4), 783-803.

Gruber, N. and C. D. Keeling (2001), An improved estimate of the isotopic air-sea disequilibrium of CO_2: Implications for the oceanic uptake of anthropogenic CO_2, *Geophys. Res. Lett.*, *28*(3), 555-558.

Gruber, N., C. D. Keeling, R. B. Bacastow, et al. (1999), Spatiotemporal patterns of carbon-13 in the global surface oceans and the oceanic Suess effect, *Global Biogeochem. Cycles*, *13*(2), 307-335.

Gruber, N., J. L. Sarmiento and T. F. Stocker (1996), An improved method for detecting anthropogenic CO_2 in the oceans, *Global Biogeochem. Cycles*, *10*(4), 809-837.

Gu, L., D. Baldocchi, S. B. Verma, et al. (2002), Advantages of diffuse radiation for terrestrial ecosystem productivity, *J. Geophys. Res.*, *107*(D5-D6), 4050.

Gu, L., D. D. Baldocchi, S. C. Wofsy, et al. (2003), Response of a deciduous forest to the Mount Pinatubo eruption: Enhanced photosynthesis, *Science*, *299*(5615), 2035-2038.

Gu, L., J. D. Fuentes, H. H. Shugart, et al. (1999), Responses of net ecosystem exchanges of carbon dioxide to changes in cloudiness: Results from two North American deciduous forests, *J. Geophys. Res.*, *104*(D24), 31421-31434.

Gurney, K. R., R. M. Law, A. S. Denning, et al. (2002), Towards robust regional estimates of CO_2 sources and sinks using atmospheric transport models, *Nature*, *415*(6872), 626-630.

Gurney, K. R., R. M. Law, A. S. Denning, et al. (2003), TransCom 3 CO_2 inversion intercomparison: 1. Annual mean control results and sensitivity to transport and prior flux information, *Tellus*, *55*(B2), 555-579.

Hammer, C. U., H. B. Clausen and W. Dansgaard (1980), Greenland Ice-Sheet Evidence of Post-Glacial Volcanism and Its Climatic Impact, *Nature*, *288*(5788), 230-235.

Hansen, J., R. Ruedy, J. Glascoe, et al. (1999), GISS analysis of surface temperature change, *J. Geophys. Res.*, *104*, 30997-31022.

Hansen, J., R. Ruedy, M. Sato, et al. (1996), Global surface air temperature in 1995: Return to pre-Pinatubo level, *Geophys. Res. Lett.*, *23*(13), 1665-1668.

Hansen, P. C. (1998), *Rank-Deficient and Discrete Ill-Posed Problems: Numerical Aspects of Linear Inversion*, 247 pp., Society for Industrial and Applied Mathematics, Philadelphia.

Heimann, M. and E. Maier-Reimer (1996), On the relations between the oceanic uptake of CO_2 and its carbon isotopes, *Global Biogeochem. Cycles*, *10*(1), 89-110.

Heimann, M. and P. Monfray (1989), Spatial and Temporal Variation of the Gas Exchange Coefficient for CO_2: 1. Data Analysis and Global Validation, pp. 29, Max-Planck-Institut für Meteorologie, Hamburg.

Hesshaimer, V., M. Heimann and I. Levin (1994), Radiocarbon evidence for a smaller oceanic carbon-dioxide sink than previously believed, *Nature*, *370*(6486), 201-203.

Hogg, A. G., F. G. McCormac, T. F. G. Higham, et al. (2002), High-precision radiocarbon measurements of contemporaneous tree-ring dated wood from the British Isles and New Zealand: AD 1850-950, *Radiocarbon*, *44*(3), 633-640.

Hua, Q. and M. Barbetti (2004), Review of tropospheric bomb ^{14}C data for carbon cycle modeling and age calibration purposes, *Radiocarbon*, *46*(3), 1273-1298.

Hua, Q., M. Barbetti, M. Worbes, et al. (1999), Review of radiocarbon data from atmospheric and tree ring samples for the period 1945-1997 AD, *Iawa J.*, *20*(3), 261-283.

Hubick, K. and G. Farquhar (1989), Carbon isotope discrimination and the ratio of carbon gained to water lost in barley cultivars, *Plant Cell Environ.*, *12*(8), 795-804.

Ito, T., J. Marshall and M. Follows (2004), What controls the uptake of transient tracers in the Southern Ocean?, *Global Biogeochem. Cycles*, *18*(2).

Jacoby, G., R. D'Arrigo and B. H. Luckman (1996), Millennial and near-millennial scale dendroclimatic studies in northern North America, in *Climatic Variations and Forcing Mechanisms of the Last 2000 years*, edited by P. D. Jones, et al., pp. 67-84, Springer-Verlag, Berlin and New York.

Jähne, B. and H. Haussecker (1998), Air-water gas exchange, *Annual Review of Fluid Mechanics*, *30*, 443-468.

Jihong, C. D. and E. Mosley-Thompson (1999), The Pinatubo eruption in South Pole snow and its potential value to ice-core paleovolcanic records, *Annals of Glaciology*, *29*, 99-105.

Jones, C. and P. Cox (2001), Modeling the volcanic signal in the atmospheric CO_2 record, *Global Biogeochem. Cycles*, *12*(2), 453-465.

Joos, F. (1996), An efficient and accurate representation of complex oceanic and biospheric models of anthropogenic carbon uptake, *Tellus. Series B, Chemical and physical meteorology*, *48*(3), 397-417.

Kaminski, T., P. J. Rayner, M. Heimann, et al. (2001), On aggregation errors in atmospheric transport inversions, *J. Geophys. Res.*, *106*(D5), 4703-4715.

Keeling, C. D., R. B. Bacastow, A. E. Bainbridge, et al. (1976), Atmospheric carbon-dioxide variations at Mauna-Loa Observatory, Hawaii, *Tellus*, *28*(6), 538-551.

Keeling, C. D., T. P. Whorf, M. Wahlen, et al. (1995), Interannual extremes in the rate of rise of atmospheric carbon-dioxide since 1980, *Nature*, *375*(6533), 666-670.

Key, R. M., A. Kozyr, C. L. Sabine, et al. (2004), A global ocean carbon climatology: Results from Global Data Analysis Project (GLODAP), *Global Biogeochemical Cycles*, *18*(4), GB4031.

Key, R. M., P. D. Quay, P. Schlosser, et al. (2002), WOCE radiocarbon IV: Pacific Ocean results; P10, P13N, P14C, P18, P19 & S4P, *Radiocarbon*, *44*(1), 239-392.

Kiehl, J. T., J. J. Hack, G. B. Bonan, et al. (1998), The National Center for Atmospheric Research Community Climate Model: CCM3, *J. Climate*, *11*(6), 1131-1149.

Kobak, K. I., I. Y. Turchinovich, N. Y. Kondrasheva, et al. (1996), Vulnerability and adaptation of the larch forest in eastern Siberia to climate change, *Water Air Soil Pollut.*, *92*(1-2), 119-127.

Komori, S., R. Nagaosa and Y. Murakami (1993), Turbulence structure and mass-transfer across a sheared air-water interface in wind-driven turbulence, *J. Fluid Mech.*, *249*, 161-183.

Krakauer, N. Y. and J. T. Randerson (2003), Do volcanic eruptions enhance or diminish net primary production? Evidence from tree rings, *Global Biogeochem. Cycles*, *17*(4), doi: 10.1029/2003GB002076.

Krakauer, N. Y., T. Schneider, J. T. Randerson, et al. (2004), Using generalized cross-validation to select parameters in inversions for regional carbon fluxes, *Geophys. Res. Lett.*, *31*(19), doi: 10.1029/2004020323.

Langenfelds, R. L., R. J. Francey, B. C. Pak, et al. (2002), Interannual growth rate of atmospheric CO_2 and its delta^{13}C, H_2, CH_4, and CO between 1992 and 1999 linked to biomass burning, *Global Biogeochem. Cycles*, *16*(3), 1048.

Langway, C. C., H. B. Clausen and C. U. Hammer (1988), An interhemispheric volcanic time marker in ice cores from Greenland and Antarctica, *Annals of Glaciology*, *10*, 102-108.

Law, R. M., Y. H. Chen and K. R. Gurney (2003), TransCom 3 CO_2 inversion intercomparison: 2. Sensitivity of annual mean results to data choices, *Tellus*, *55*(B2), 580-595.

Leavitt, S. W. and A. Long (1991), Seasonal Stable-Carbon Isotope Variability in Tree Rings - Possible Paleoenvironmental Signals, *Chem. Geol.*, *87*(1), 59-70.

LeBlanc, D. C. (1996), Using tree rings to study forest decline: An epidemiological approach based on estimated annual wood volume increment, in *Tree Rings, Environment and Humanity: Proceedings of the International Conference, Tucson, Arizona, 17-21 May 1994*, edited by J. S. Dean, et al., pp. 437-449, Radiocarbon, Dept. of Geosciences, University of Arizona, Tucson.

Lee, Y. A. and L. J. Fang (2000), A possible volcanic signal in NCEP/NCAR reanalysis data, *Terr. Atmos. Ocean. Sci.*, *11*(4), 895-908.

Levin, I. and V. Hesshaimer (2000), Radiocarbon - A unique tracer of global carbon cycle dynamics, *Radiocarbon*, *42*(1), 69-80.

Levin, I. and B. Kromer (2004), The Tropospheric $^{14}CO_2$ level in Mid-Latitudes of the Northern Hemisphere (1959–2003), *Radiocarbon*, *46*(3), 1261-1272.

Levin, I., B. Kromer, M. Schmidt, et al. (2003), A novel approach for independent budgeting of fossil fuel CO_2 over Europe by $^{14}CO_2$ observations, *Geophys. Res. Lett.*, *30*(23), art. no.-2194.

Levin, I., B. Kromer, D. Wagenbach, et al. (1987), Carbon isotope measurements of atmospheric CO_2 at a coastal station in Antarctica, *Tellus*, *39B*(1-2), 89-95.

Lindzen, R. S. and C. Giannitsis (1998), On the climatic implications of volcanic cooling, *J. Geophys. Res.*, *103*(D6), 5929-5941.

Lingenfelter, R. E. (1963), Production of carbon-14 by cosmic-ray neutrons, *Reviews of Geophysics*, *1*(1), 35-55.

Linick, T. W. (1980), Bomb-produced C-14 in the surface-water of the Pacific Ocean, *Radiocarbon*, *22*(3), 599-606.

Liss, P. S., A. L. Chuck, S. M. Turner, et al. (2004), Air-sea gas exchange in Antarctic waters, *Antarctic Sci.*, *16*(4), 517-529.

Liss, P. S. and L. Merlivat (1986), Air-sea gas exchange rates: introduction and synthesis, in *The Role of Air-Sea Exchange in Geochemical Cycling*, edited by P. Buat-Ménard, pp. 113-129, D. Reidel, Dordrecht.

Lough, J. M. and H. C. Fritts (1987), An assessment of the possible effects of volcanic eruptions on North American climate using tree-ring data , 1602 to 1900 A.D., *Climatic Change*, *10*(3), 219-239.

Lucht, W., I. C. Prentice, R. B. Myneni, et al. (2002), Climatic control of the high-latitude vegetation greening trend and Pinatubo effect, *Science*, *296*(5573), 1687-1689.

Mahowald, N. M., P. J. Rasch, B. E. Eaton, et al. (1997), Transport of [222]radon to the remote troposphere using the Model of Atmospheric Transport and Chemistry and assimilated winds from ECMWF and the National Center for Environmental Prediction/NCAR, *J. Geophys. Res.*, *102*(D23), 28139-28151.

Manning, M. R., D. C. Lowe, W. H. Melhuish, et al. (1990), The use of radiocarbon measurements in atmospheric studies, *Radiocarbon*, *32*(1), 37-58.

Marland, G., T. A. Boden and R. J. Andres (2005), Global, regional, and national fossil fuel CO_2 emissions, in *Trends: A Compendium of Data on Global Change.*, Carbon Dioxide Information Analysis Center, Oak Ridge National Laboratory, U.S. Department of Energy.

Marshall, J., A. Adcroft, C. Hill, et al. (1997), A finite-volume, incompressible Navier Stokes model for studies of the ocean on parallel computers, *J. Geophys. Res.*, *102*(C3), 5753-5766.

Masiello, C. A., E. R. M. Druffel and J. E. Bauer (1998), Physical controls on dissolved inorganic radiocarbon variability in the California Current, *Deep-Sea Res.*, *45*(4-5), 617-642.

McGillis, W. R., J. B. Edson, J. E. Hare, et al. (2001), Direct covariance air-sea CO_2 fluxes, *J. Geophys. Res.*, *106*(C8), 16729-16745.

McGillis, W. R., J. B. Edson, C. J. Zappa, et al. (2004), Air-sea CO_2 exchange in the equatorial Pacific, *J. Geophys. Res.*, *109*(C8).

McKee, K. L., I. C. Feller, M. Popp, et al. (2002), Mangrove isotopic (delta ^{15}N and delta ^{13}C) fractionation across a nitrogen vs. phosphorus limitation gradient, *Ecology*, *83*(4), 1065-1075.

McNeil, B. I., R. J. Matear, R. M. Key, et al. (2003), Anthropogenic CO_2 uptake by the ocean based on the global chlorofluorocarbon data set, *Science*, *299*(5604), 235-239.

Michalak, A. M., L. Bruhwiler and P. P. Tans (2004), A geostatistical approach to surface flux estimation of atmospheric trace gases, *J. Geophys. Res.*, *109*(D14).

Michalak, A. M., A. Hirsch, L. Bruhwiler, et al. (2005), Maximum likelihood estimation of covariance parameters for Bayesian atmospheric trace gas surface flux inversions, *J. Geophys. Res.*, *110*(D24).

Mikaloff Fletcher, S. E., N. Gruber, A. R. Jacobson, et al. (in press), Inverse estimates of anthropogenic CO_2 uptake, transport, and storage by the ocean, *Global Biogeochemical Cycles*, doi: 10.1029/2005GB002530.

Molineaux, B. and P. Ineichen (1996), Impact of Pinatubo aerosols on the seasonal trends of global, direct and diffuse irradiance in two northern mid-latitude sites, *Solar Energy*, *58*(1-3), 91-101.

Monahan, E. C. (2002), Oceanic whitecaps: Sea surface features detectable via satellite that are indicators of the magnitude of the air-sea gas transfer coefficient, *Proc. Indian Acad. Sci.-Earth Planet. Sci*, *111*(3), 315-319.

Murnane, R. J., J. L. Sarmiento and C. Le Quéré (1999), Spatial distribution of air-sea CO_2 fluxes and the interhemispheric transport of carbon by the oceans, *Global Biogeochem. Cycles*, *13*(2), 287-305.

Myneni, R. B., C. J. Tucker, G. Asrar, et al. (1998), Interannual variations in satellite-sensed vegetation index data from 1981 to 1991, *J. Geophys. Res.*, *103*(D6), 6145-6160.

Nightingale, P. D., G. Malin, C. S. Law, et al. (2000), In situ evaluation of air-sea gas exchange parameterizations using novel conservative and volatile tracers, *Global Biogeochem. Cycles*, *14*(1), 373-387.

Niyogi, D., H. I. Chang, V. K. Saxena, et al. (2004), Direct observations of the effects of aerosol loading on net ecosystem CO2 exchanges over different landscapes, *Geophys. Res. Lett.*, *31*(20).

Nydal, R. (2000), Radiocarbon in the ocean, *Radiocarbon*, *42*(1), 81-98.

Olsen, A., R. Wanninkhof, J. A. Trinanes, et al. (2005), The effect of wind speed products and wind speed-gas exchange relationships on interannual variability of the air-sea CO2 gas transfer velocity, *Tellus*, *57*(2), 95-106.

Olsen, S. C. and J. T. Randerson (2004), Differences between surface and column atmospheric CO_2 and implications for carbon cycle research, *J. Geophys. Res.*, *109*, D02301, doi:10.1029/2003JD003968.

Orr, J. C., V. J. Fabry, O. Aumont, et al. (2005), Anthropogenic ocean acidification over the twenty-first century and its impact on calcifying organisms, *Nature*, *437*(7059), 681-686.

Orr, J. C., E. Maier-Reimer, U. Mikolajewicz, et al. (2001), Estimates of anthropogenic carbon uptake from four three- dimensional global ocean models, *Global Biogeochem. Cycles*, *15*(1), 43-60.

Ostlund, H. G. and M. Stuiver (1980), Geosecs Pacific Radiocarbon, *Radiocarbon*, *22*(1), 25-53.

Pacanowski, R. C., K. Dixon and A. Rosati (1993), The GFDL modular ocean model users guide, pp. 46, Geophysical Fluid Dynamics Laboratory, Princeton.

Palais, J. M., M. S. Germani and G. A. Zielinski (1992), Interhemispheric transport of volcanic ash from a 1259 AD volcanic-eruption to the Greenland and Antarctic Ice Sheets, *Geophys. Res. Lett.*, *19*(8), 801-804.

Parker, R. L. and M. K. McNutt (1980), Statistics for the one-norm misfit measure, *J. Geophys. Res.*, *85*, 4429-4430.

Peacock, S. (2004), Debate over the ocean bomb radiocarbon sink: Closing the gap, *Global Biogeochem. Cycles*, *18*, GB2022.

Peacock, S., M. Maltrud and R. Bleck (2005), Putting models to the data test: a case study using Indian Ocean CFC-11 data, *Ocean Modelling*, *9*(1), 1-22.

Peng, T. H., W. S. Broecker, G. G. Mathieu, et al. (1979), Radon evasion rates in the Atlantic and Pacific Oceans as determined during the Geosecs Program, *Journal of Geophysical Research-Oceans and Atmospheres*, *84*(NC5), 2471-2486.

Penuelas, J. and M. Estiarte (1997), Trends in plant carbon concentration and plant demand for N throughout this century, *Oecologia*, *109*(1), 69-73.

Perrie, W., W. Q. Zhang, X. J. Ren, et al. (2004), The role of midlatitude storms on air-sea exchange of CO2, *Geophys. Res. Lett.*, *31*(9).

Plattner, G. K., F. Joos and T. F. Stocker (2002), Revision of the global carbon budget due to changing air-sea oxygen fluxes, *Global Biogeochem. Cycles*, *16*(4), art. no.-1096.

Porter, S. C. (1986), Pattern and forcing of Northern Hemishpere glacier variations during the last millennium, *Quaternary Research*, *26*(1), 27-48.

Potter, C. S., J. T. Randerson, C. B. Field, et al. (1993), Terrestrial ecosystem production - a process model based on global satellite and surface data, *Global Biogeochem. Cycles*, *7*(4), 811-841.

Prentice, I. C., G. D. Farquhar, M. J. R. Fasham, et al. (2001), The Carbon Cycle and Atmospheric Carbon Dioxide, in *Climate Change 2001 : The Scientific Basis :*

Contribution of Working Group I to the Third Assessment Report of the Intergovernmental Panel on Climate Change, edited by J. T. Houghton, et al., pp. 183-238, Cambridge University Press, Cambridge, U.K. and New York.

Primeau, F. (2005), Characterizing transport between the surface mixed layer and the ocean interior with a forward and adjoint global ocean transport model, *J. Phys. Oceanogr.*, *35*(4), 545-564.

Quay, P., S. King, D. White, et al. (2000), Atmospheric ^{14}CO: A tracer of OH concentration and mixing rates, *J. Geophys. Res.*, *105*(D12), 15147-15166.

Quay, P., R. Sonnerup, T. Westby, et al. (2003), Changes in the $^{13}C/^{12}C$ of dissolved inorganic carbon in the ocean as a tracer of anthropogenic CO_2 uptake, *Global Biogeochem. Cycles*, *17*(1), art. no.-1004.

Randerson, J. T., I. G. Enting, E. A. G. Schuur, et al. (2002), Seasonal and latitudinal variability of troposphere $\Delta^{14}CO_2$: Post bomb contributions from fossil fuels, oceans, the stratosphere, and the terrestrial biosphere, *Global Biogeochem. Cycles*, *16*(4), art. no. 1112.

Randerson, J. T., M. V. Thompson, T. J. Conway, et al. (1997), The contribution of terrestrial sources and sinks to trends in the seasonal cycle of atmospheric carbon dioxide, *Global Biogeochem. Cycles*, *11*(4), 535-560.

Rasch, P. J., X. X. Tie, B. A. Boville, et al. (1994), A 3-dimensional transport model for the middle atmosphere, *J. Geophys. Res.*, *99*(D1), 999-1017.

Rathgeber, C., A. Nicault, J. Guiot, et al. (2000), Simulated responses of *Pinus halepensis* forest productivity to climatic change and CO_2 increase using a statistical model, *Global and Planetary Change*, *26*(4), 405-421.

Rayner, P. J., I. G. Enting, R. J. Francey, et al. (1999), Reconstructing the recent carbon cycle from atmospheric CO_2, $\delta^{13}C$ and O_2/N_2 observations, *Tellus*, *51*(B2), 213-232.

Robertson, A., J. Overpeck, D. Rind, et al. (2001), Hypothesized climate forcing time series for the last 500 years, *J. Geophys. Res.*, *106*(D14), 14783-14803.

Robock, A. (2000), Volcanic eruptions and climate, *Reviews of Geophysics*, *38*(2), 191-219.

Robock, A. and J. P. Mao (1995), The volcanic signal in surface temperature observations, *J. Climate*, *8*(5), 1086-1103.

Rödenbeck, C., S. Houweling, M. Gloor, et al. (2003), CO_2 flux history 1982-2001 inferred from atmospheric data using a global inversion of atmospheric transport, *Atmos. Chem. Phys.*, *3*, 1919-1964.

Roderick, M., G. Farquhar, S. Berry, et al. (2001), On the direct effect of clouds and atmospheric particles on the productivity and structure of vegetation, *Oecologia*, *129*(1), 21-30.

Roderick, M. L. and G. D. Farquhar (2002), The cause of decreased pan evaporation over the past 50 years, *Science*, *298*(5597), 1410-1411.

Rojstaczer, S., S. M. Sterling and N. J. Moore (2001), Human appropriation of photosynthesis products, *Science*, *294*(5551), 2549-2552.

Romanovsky, V. E. and T. E. Osterkamp (1997), Thawing of the active layer on the coastal plain of the Alaskan Arctic, *Permafrost Periglacial Process.*, *8*(1), 1-22.

Roy, T., P. Rayner, R. Matear, et al. (2003), Southern hemisphere ocean CO_2 uptake: reconciling atmospheric and oceanic estimates, *Tellus*, *55*(2), 701-710.

Rozanski, K., I. Levin, J. Stock, et al. (1995), Atmospheric $^{14}CO_2$ variations in the Equatorial region, *Radiocarbon*, *37*(2), 509-515.

Rubin, S. I. and R. M. Key (2002), Separating natural and bomb-produced radiocarbon in the ocean: The potential alkalinity method, *Global Biogeochem. Cycles*, *16*(4), 1105.

Sabine, C. L., R. A. Feely, N. Gruber, et al. (2004), The oceanic sink for anthropogenic CO_2, *Science*, *305*(5682), 367-371.

Sato, M., J. E. Hansen, M. P. McCormick, et al. (1993), Stratospheric aerosol optical depths, 1850-1990, *J. Geophys. Res.*, *98*(D12), 22987-22994.

Schlitzer, R. (2000), Applying the adjoint method for biogeochemical modeling: export of particulate organic matter in the world ocean, in *Inverse Methods in Global Biogeochemical Cycles*, edited by P. Kasibhatla, et al., pp. 107-124, American Geophysical Union, Washington.

Schweingruber, F. H. (1988), *Tree Rings: Basics and Applications of Dendrochronology*, 276 pp., D. Reidel Pub. Co., Dordrecht and Boston.

Schweingruber, F. H., K. R. Briffa and P. D. Jones (1991), Yearly maps of summer temperatures in western-Europe from AD 1750 to 1975 and western North-America from 1600 to 1982 - Results of a radiodensitometrical study on tree rings, *Vegetatio*, *92*(1), 5-71.

Scuderi, L. A. (1990), Tree-ring evidence for climatically effective volcanic eruptions, *Quaternary Research*, *34*(1), 67-85.

Sear, C. B., P. M. Kelly, P. D. Jones, et al. (1987), Global surface temperature responses to major volcanic eruptions, *Nature*, *330*(6146), 365-367.

Shabanov, N. V., L. M. Zhou, Y. Knyazikhin, et al. (2002), Analysis of interannual changes in northern vegetation activity observed in AVHRR data from 1981 to 1994, *IEEE Trans. Geosci. Remote Sensing*, *40*(1), 115-130.

Simkin, T. and L. Siebert (1994), *Volcanoes of the World: A Regional Directory, Gazetteer, and Chronology of Volcanism During the Last 10,000 Years*, 349 pp., Geoscience Press, Tucson.

Sinclair, T. R., T. Shiraiwa and G. L. Hammer (1992), Variation in crop radiation-use efficiency with increased diffuse radiation, *Crop Science*, *32*, 1281-1284.

Stammer, D., K. Ueyoshi, A. Köhl, et al. (2004), Estimating air-sea fluxes of heat, freshwater, and momentum through global ocean data assimilation, *J. Geophys. Res.*, *109*, C05023, doi:10.1029/2003JC002082.

Steiner, A. L. and W. L. Chameides (2005), Aerosol-induced thermal effects increase modelled terrestrial photosynthesis and transpiration, *Tellus*, *57*(5), 404-411.

Stephens, C., J. I. Antonov, M. E. Conkright, et al. (2002), *World Ocean Atlas 2001, Volume 1: Temperature*, 167 pp., US Government Printing Office, Washington.

Stothers, R. B. (2002), Cloudy and clear stratospheres before AD 1000 inferred from written sources, *J. Geophys. Res.*, *107*(D23), art. no. 4718.

Stuiver, M. and B. Becker (1993), High-precision decadal calibration of the radiocarbon time scale, AD 1950-6000 BC, *Radiocarbon*, *35*(1), 35-65.

Stuiver, M., P. M. Grootes and T. F. Braziunas (1995), The GISP2 delta[18]O climate record of the past 16,500 years and the role of the sun, ocean, and volcanoes, *Quaternary Research*, *44*(3), 341-354.

Stuiver, M. and H. G. Ostlund (1980), Geosecs Atlantic radiocarbon, *Radiocarbon*, *22*(1), 1-24.

Stuiver, M. and H. G. Ostlund (1983), Geosecs Indian-Ocean and Mediterranean radiocarbon, *Radiocarbon*, *25*(1), 1-29.

Stuiver, M. and H. A. Polach (1977), Reporting of C-14 data - Discussion, *Radiocarbon*, *19*(3), 355-363.

Stuiver, M. and P. D. Quay (1981), Atmospheric ^{14}C changes resulting from fossil fuel CO_2 release and cosmic ray flux variability, *Earth Planet. Sci. Lett.*, *53*(3), 349-362.

Suess, H. E. (1955), Radiocarbon Concentration in Modern Wood, *Science*, *122*(3166), 415-417.

Takahashi, T., S. C. Sutherland, C. Sweeney, et al. (2002), Global sea-air CO_2 flux based on climatological surface ocean pCO_2, and seasonal biological and temperature effects, *Deep-Sea Res.*, *49*(9-10), 1601-1622.

Tang, K. L., X. H. Feng and G. Funkhouser (1999), The delta ^{13}C of tree rings in full-bark and strip-bark bristlecone pine trees in the White Mountains of California, *Glob. Change Biol.*, *5*(1), 33-40.

Tans, P. P., J. A. Berry and R. F. Keeling (1993), Oceanic ^{13}C/^{12}C observations: a new window on ocean CO_2 uptake, *Global Biogeochem. Cycles*, *7*(2), 353-368.

Tans, P. P., A. F. M. Dejong and W. G. Mook (1979), Natural atmospheric C-14 variation and the Suess Effect, *Nature*, *280*(5725), 826-827.

Tans, P. P., I. Y. Fung and T. Takahashi (1990), Observational constraints on the global atmospheric CO_2 Budget, *Science*, *247*(4949), 1431-1438.

Thompson, M. V. and J. T. Randerson (1999), Impulse response functions of terrestrial carbon cycle models: method and application, *Glob. Change Biol.*, *5*(4), 371-394.

Toggweiler, J. R., K. Dixon and K. Bryan (1989), Simulations of radiocarbon in a coarse-resolution world ocean model .1. Steady state prebomb distributions, *J. Geophys. Res.*, *94*(C6), 8217-8242.

Trolier, M., J. W. C. White, P. P. Tans, et al. (1996), Monitoring the isotopic composition of atmospheric CO_2: Measurements from the NOAA Global Air Sampling Network, *J. Geophys. Res.*, *101*(D20), 25897-25916.

Turney, D. E., W. C. Smith and S. Banerjee (2005), A measure of near-surface fluid motions that predicts air-water gas transfer in a wide range of conditions, *Geophys. Res. Lett.*, *32*(4).

Van Huffel, S. and J. Vandewalle (1989), Analysis and properties of the generalized total least squares problem $Ax \approx B$ when some or all columns in A are subject to error, *SIAM J. Matrix Anal. Appl.*, *10*(3), 294-315.

Van Scoy, K. A., K. P. Morris, J. E. Robertson, et al. (1995), Thermal skin effect and the air-sea flux of carbon dioxide: A seasonal high-resolution estimate, *Global Biogeochem. Cycles*, *9*(2), 253-262.

Vitousek, P. M., P. R. Ehrlich, A. H. Ehrlich, et al. (1986), Human appropriation of the products of photosynthesis, *Bioscience*, *36*(6), 368-373.

Vogel, J. C. (1971), Pretoria radiocarbon dates I, *Radiocarbon*, *13*(2), 378-394.

Wahba, G., D. R. Johnson, F. Gao, et al. (1995), Adaptive tuning of numerical weather prediction models - Randomized GCV in 3-dimensional and 4-dimensional data assimilation, *Mon. Weather Rev.*, *123*(11), 3358-3369.

Walsh, J. (1978), A data set on northern hemisphere sea ice extent, 1953-1976, pp. 49-51, World Data Center for Glaciology (Snow and Ice), Report GD-2.

Wanninkhof, R. (1992), Relationship between wind-speed and gas-exchange over the ocean, *J. Geophys. Res.*, *97*(C5), 7373-7382.

Wanninkhof, R. and W. R. McGillis (1999), A cubic relationship between air-sea CO_2 exchange and wind speed, *Geophys. Res. Lett.*, *26*(13), 1889-1892.

Wanninkhof, R., K. F. Sullivan and Z. Top (2004), Air-sea gas transfer in the Southern Ocean, *J. Geophys. Res.*, *109*(C8).

Ward, B., R. Wanninkhof, W. R. McGillis, et al. (2004), Biases in the air-sea flux of CO_2 resulting from ocean surface temperature gradients, *J. Geophys. Res.*, *109*(C8).

Watson, A. J. (1997), Volcanic iron, CO_2, ocean productivity and climate, *Nature*, *385*(6617), 587-588.

Weiss, R. F. and B. A. Price (1980), Nitrous oxide solubility in water and seawater, *Mar. Chem.*, *8*(4), 347-359.

Woolf, D. K. (2005), Parametrization of gas transfer velocities and sea-state-dependent wave breaking, *Tellus*, *57*(2), 87-94.

Worbes, M. (1999), Annual growth rings, rainfall-dependent growth and long-term growth patterns of tropical trees from the Caparo Forest Reserve in Venezuela, *Journal of Ecology*, *87*(3), 391-403.

Wunsch, C. (1996), *The Ocean Circulation Inverse Problem*, 442 pp., Cambridge University Press, Cambridge; New York.

Yang, Z. H., G. C. Toon, J. S. Margolis, et al. (2002), Atmospheric CO_2 retrieved from ground-based near IR solar spectra, *Geophys. Res. Lett.*, *29*(9), 1339.

Zhang, J., P. D. Quay and D. O. Wilbur (1995), Carbon isotope fractionation during gas-water exchange and dissolution of CO_2, *Geochim. Cosmochim. Acta*, *59*(1), 107-114.

Zhao, D., Y. Toba, Y. Suzuki, et al. (2003), Effect of wind waves on air-sea gas exchange: proposal of an overall CO_2 transfer velocity formula as a function of breaking-wave parameter, *Tellus*, *55*(2), 478-487.

Zhou, L. M., C. J. Tucker, R. K. Kaufmann, et al. (2001), Variations in northern vegetation activity inferred from satellite data of vegetation index during 1981 to 1999, *J. Geophys. Res.*, *106*(D17), 20069-20083.

Zielinski, G. A. (1995), Stratospheric Loading and Optical Depth Estimates of Explosive Volcanism over the Last 2100 Years Derived from the Greenland- Ice-Sheet-Project-2 Ice Core, *J. Geophys. Res.*, *100*(D10), 20937-20955.

Zielinski, G. A. (2000), Use of paleo-records in determining variability within the volcanism-climate system, *Quaternary Science Reviews*, *19*(1-5), 417-438.

Zielinski, G. A., J. E. Dibb, Q. Z. Yang, et al. (1997), Assessment of the record of the 1982 El Chichon eruption as preserved in Greenland snow, *J. Geophys. Res.*, *102*(D25), 30031-30045.

Zwally, H. J., J. Comiso, C. Parkinson, et al. (1983), Antarctic Sea Ice, 1973-1976: Satellite Passive Microwave Observations, pp. 206, NASA.